Sintering and Joining of Low Temperature Co-Fired Tungsten and Aluminum Oxide

by

Yuttanant Boonyongmaneerat

Sc. B. Materials Science and Engineering
Brown University, 2002

SUBMITTED TO THE DEPARTMENT OF MATERIALS SCIENCE AND ENGINEERING
IN PARTIAL FULFILLMENT OF THE REQUIREMENTS FOR THE DEGREE OF

DOCTOR OF PHILOSOPHY IN MATERAIALS SCIENCE AND ENGINEERING
AT THE
MASSACHUSETTS INSTITUTE OF TECHNOLOGY

JUNE 2006

Signature of Author: _____
Department of Materials Science and Engineering
May 26, 2006

Certified by: _____
Christopher A. Schuh
Danae and Vasilios Salapatas Associate Professor of Metallurgy
Thesis Supervisor

Certified by: _____
Thomas W. Eagar
Professor of Materials Engineering
Thesis Co-Supervisor

Accepted by: _____
Samuel M. Allen
POSCO Professor of Physical Metallurgy
Chair, Departmental Committee for Graduate Students

Sintering and Joining of Low Temperature Co-Fired Tungsten and Aluminum Oxide

by

Yuttanant Boonyongmaneerat

Submitted to the Department of Materials Science and Engineering
on May 26, 2006 in Partial Fulfillment of the
Requirements for the Degree of Doctor of Philosophy in
Materials Science and Engineering

ABSTRACT

Conventional methods used to fabricate co-fired tungsten/alumina composites usually rely on high temperature processing (>1500°C). As it would be beneficial or even necessary for some applications to produce such composites at relatively low firing temperatures, low-temperature processing techniques and the attendant knowledge of processing-property relationships need to be developed. In this thesis, a set of experiments and simulations are performed to obtain a better understanding of sintering and joining of the tungsten/alumina system processed at temperatures near or below 1200°C.

The technique of activated sintering for tungsten is investigated, whereby a minimal content of additives enables low firing temperatures through a change in the sintering mechanism for tungsten. Tungsten compacts produced by this method are found to sinter only to the "initial stage" and are characterized by high residual porosity level. Hardness and fracture toughness of such partially-sintered materials are examined experimentally and analytically, and dependence of mechanical properties on the relative particle neck size is observed.

Various studies are carried out to examine both fundamental and practical aspects of joining co-fired tungsten/alumina. First, contributions to adhesion of co-sintered bilayers are studied where the properties of the tungsten layer are controlled using the process of activated sintering. Using a bending delamination test, improvements in sintered density of tungsten are found to increase the adhesive strength of the system only up to a point, beyond which shrinkage mismatch compromises the intrinsic toughness of the interface. A study of low-temperature co-fired tungsten/alumina is then focused on composite shells for an investment casting application. The influences of various processing parameters in a slurry-based route on the sintering and adhesion properties of tungsten/alumina are investigated. Binder content, stucco sand application, and powder characteristics are among the parameters found to critically control the quality of tungsten/alumina shells produced. Finally, the feasibility of several joining strategies, which involve the use of chemical additives, is examined on co-fired tungsten/alumina compacts processed at low temperatures. Some bonding techniques are verified to help improve the bonding of the co-sintered composites.

Thesis Supervisor: Christopher A. Schuh
Title: Danae and Vasilios Salapatas Associate Professor of Metallurgy

Thesis Co-Supervisor: Thomas W. Eagar
Title: Professor of Materials Engineering

Acknowledgements

The completion of this thesis would not be possible without the support of several persons throughout the course of my study. I would like to express my sincere gratitude to my advisors, Prof. Christopher Schuh and Prof. Thomas Eagar, for their guidance, support and research opportunity. They have been a constant source of inspiration and have shaped many aspects of my academic life. I am also deeply thankful to my thesis committee members, Prof. Bernhardt Wuensch and Prof. David Parks, for their invaluable advice and guidance. Additionally, I would like to express my sincere thank to Donald Galler, Harold Larson, Alan Lund, and Yinlin Xie for their help and technical support.

I am very grateful to Tom Allen, Dick Humphrey, and Rick Kenyon of Selmet Inc. for giving me an opportunity to embark on this research and show me the world of investment casting. I would like to extend special thanks to Andy Martinez for his friendship, support, and collaboration. Many thanks to Dan Blankenship for all his help and assistance. It has been a great experience working with them. I also would like to thank several other persons at Selmet for their supports: Tom Daly, Dustin Harrington, Robert Comer, Art Hill, Sandra Halsey, and the investing and casting crews. To me, Selmet is one big engineering school where I was privileged enough to have gained so much knowledge and experience.

I would like to acknowledge Raymundo Arroyave, Nuwong Chollacoop, Megan Frary, Jerilyn Hill, Neil Jenkins, Samerkhae Jongthammanurak, Jizhao Ma, Nonglak Meethong, Christopher Musso, Wanida Pongsaksawad, Ratchatee Techapiesancharoenkij, Panitarn Wanakamol, Jessada Wannasin and Joel Williams for their friendships and supports. I would also like to thank James LeBeau for his contribution on the slurry processing project; everyone in the Schuh and the Welding Research Groups: Ying Chen, Andrew Detor, Jeremy Mason, Corinne Packard, Shiyun Ruan, Jason Trelewicz, David Fischer, Brian Hohmann, as well as Bruce Wu, In-Suk Choi, and Simon Bellemare for great times in and out of the labs; Fu, Joy, Petch, P'Tik, Pu, Sup, Ton and Wang for friendship, support and all fun activities we did together in Boston. Lastly, I would like to express my wholehearted gratitude to my parents, family, and my girlfriend, Jib, for all their love and support.

Table of Contents

Part B: JOINING OF W AND Al_2O_3

List of Tables and Figures

Chapter I. Introduction

1.1 Motivation and Thesis Objectives

With its very high melting point of 3422°C, tungsten (W) has been a material of choice for a number of refractory uses including heating, electrical and welding applications. Among these, W is most well known for its use as a filament for incandescent light bulbs, as developed by Coolidge in 1910 [1, 2]. Because of its positive influence on mechanical properties, W is also employed as a component for making heavy metal alloys and superalloys used in turbine blades and wear-resistant parts. Additionally, W is often used in combination with a ceramic in co-fired composites. For example, to provide electrical contacts for electronic packages, a patterned, W-metallizing film is layered on a ceramic substrate, which is usually made from a material with good dielectric properties such as aluminum oxide (Al_2O_3) or aluminum nitride (AlN). For brazing applications, a thin W metallizing layer is applied on a ceramic article to help enhance the wetting properties of the material. In addition, a coating layer of W on an Al_2O_3 substrate (or vice versa) can also be utilized for reaction barriers, or for composite structures requiring the low thermal diffusivity of Al_2O_3 combined with the refractory properties of a W surface. For the W-Al_2O_3 system, in particular, bonding is usually conducted through a sintering process at a firing temperature above 1500°C with the use of a joining technique, such as the glass migration process, to improve bonding.

While joining techniques performed at high temperatures are common, low temperature joining processes for this system (below 1200°C), have not gained much attention. If the co-sintered W-Al_2O_3 system could be fabricated at low temperatures, several benefits, such as reduction in energy cost, increase in productivity, and reduced thermal softening of the components would result. Additionally, in some applications, it is required that W and Al_2O_3 contain some degree of porosity, and such a structure can be achieved by partial sintering of the materials at a low firing temperature.

Of particular interest to this thesis is a co-sintered W/Al_2O_3 composite used for investment casting applications. For metal alloys to be cast with the investment casting process, fired molds need to be fabricated with a cavity of the same form and geometric details as the finished cast components. This is achievable by applying powder slurries layer by layer, until a desirable thickness is obtained. Al_2O_3 is a refractory material commonly used for such

applications. However, in some cases, undesirable reaction between Al_2O_3 and the melt may occur during casting. This can be prevented by applying a layer of W adjacent to the Al_2O_3, which can function as a reaction barrier. Since the mold needs to contain some porosity, so that steams can be transferred through the mold during the autoclave operation and so that entrapped gas can migrate out of the mold during the metal casting step, relatively low firing temperatures are favorable for mold production.

To effectively produce co-sintered W/Al_2O_3 at low temperatures, mechanical strength of the individual layers as well as the adhesion properties between bonded layers needs to be carefully controlled, as these underpin the structural integrity of the bonding components. With a weak interface, residual stresses and the application of external pressure could lead to buckling and spallation of the joined layers. If the strength of the sintered W layer is too low, chipping and cracking of the layer could occur. Cracks originating from the surface may also extend to the interface, causing delamination. Since both sintering of W and joining of W and Al_2O_3 are usually performed at high temperatures, research on sintering and joining processes of these materials at relatively low firing temperatures is very limited.

In this thesis, a set of experiments and simulations are performed to obtain a better understanding of low-temperature sintering and joining in the W/Al_2O_3 system. In particular, the objectives of this thesis are (i) to gain a fundamental understanding of how various processing parameters may influence the sintering and adhesion properties of low-temperature co-sintered W/Al_2O_3 and (ii) to investigate and develop processing and joining techniques that can be practically useful for joining W and Al_2O_3 at low firing temperatures.

1.2 Thesis Organization

The material presented in this thesis progresses from discussion of a relatively simple system, where the sintering and properties of just one component, W, are examined, to more complex systems, where co-firing of W and Al_2O_3 and the incorporation of additional joining compounds are investigated. This thesis contains five main chapters, which are organized in two main parts:

Part A: SINTERING OF W

- Chapter II. Sintering of W
- Chapter III. Sintering of W at Low Temperatures

Part B: JOINING OF W AND Al_2O_3

- Chapter IV. Co-firing of W and Al_2O_3
- Chapter V. Joining of W and Al_2O_3 through a Slurry-Based Processing Route
- Chapter VI. Bonding Strategies of W and Al_2O_3 at Low Temperatures

The material presented in each chapter follows a logical progression, and the various chapters connect to one another and are fully cross-referenced. However, each chapter is also self-contained. Accordingly, there is some redundancy in e.g., introductory comments and procedure statements. This structure is presented intentionally to allow for individual chapters to be reviewed separately.

In Chapter II, a literature review on the standard high-temperature sintering process typically used for W is presented. With the use of the "activated sintering" technique, both sintering kinetics and corresponding properties of partially-sintered W processed at relatively low firing temperatures are discussed in Chapter III. In Part B (Ch. IV-VI), the Al_2O_3 layer is introduced, and both processing and mechanical property aspects of joining of W and Al_2O_3 are investigated. For these chapters, literature reviews relevant to each subject are incorporated within each chapter. Chapter IV presents a fundamental study of the contributions to adhesion of W and Al_2O_3 which are joined via a purely mechanical interlocking mechanism. In chapter V, joining of W and Al_2O_3 through a slurry-based processing route is examined. Particular attention is focused on composite shells for investment casting applications. Finally, Chapter VI concerns the investigation of several bonding strategies for W and Al_2O_3 which involve the use of chemical additives in the system.

Part A: SINTERING OF W

Chapter II. Sintering of Tungsten (W)

2.1 Introduction

The process of sintering allows near-net shape manufacturing of components at temperatures below their melting points, and consequently has been widely employed in numerous applications. Because of its very high melting point, casting molten W is not economically feasible, and instead, W is usually processed by sintering. For many applications, including W filaments, W is generally sintered to the "final stage" where porosity is minimal. In this section, a literature review on sintering techniques for W and the resulting sintered properties will be presented. As will be seen, while W is traditionally sintered at high temperatures, some research has been conducted towards the development and improved understanding of relatively low-temperature W sintering processes.

2.2 Literature Review on Sintering of W

2.2.1 Sintering

Sintering refers to the consolidation of powder materials upon the application of thermal energy. The sintering process, which is driven by the reduction of the solid/vapor interfacial area of powders, involves atomic diffusion of material, which leads to bonding and densification of the sintered particles. Depending on sintering protocols, namely temperature and firing duration, the powder materials may be sintered to the "initial", "intermediate", or "final" sintering stage [3]. In the initial stage, necks grow between sintered particles, and the degree of shrinkage and densification is relatively low. At higher sintered density, generally above 80 %TD (theoretical density), the formation of interconnected pores and pore isolation occur, marking the intermediate and final stages, respectively. As sintering proceeds, grain growth also occurs in the final sintering stage.

A general practice in sintering techniques involves the packing of green (unfired) powders, either metallic or ceramic, into a desired geometry, followed by firing the materials in a furnace. Consolidation of green materials can be achieved through various processes, such as drying pressing, slip casting, and injection molding. A detailed discussion of these processes is provided in Chapter V, Section 5.2.

2.2.2 Solid-State Sintering of W

Sintering is commonly performed on W through the final stage to achieve a nearly fully dense body. Two sintering techniques, namely 'direct' and 'indirect' techniques, are common. In so-called direct sintering, a W compact (which is usually previously pre-sintered at 1000-1150°C for 30 minutes), is resistively heated through Mo or W clips held at the ends of the compact. Coarse powders with particle size larger than 5 μm are usually required to build up the necessary electrical resistance. To obtain high theoretical densities in the range 88.5-96%, the sample is commonly sintered at a final temperature of 2700-3100°C for 30-60 min. In indirect sintering, heating is achieved by resistance or induction. A furnace is usually subjected to a vacuum of 10^{-5} torr then backfilled with a hydrogen-containing atmosphere. The typical sintering temperature ranges up to 3000°C for times between 15 and 30 minutes. In the early stages of sintering, a slow heating rate is necessary to deoxidize the material. Additionally, to prevent

temperature gradients, which can result in cracking of the sintered compact, a stepwise sintering schedule is generally applied [4].

2.2.3 Effects of Sintering Variables

a. Size Effects

Since the sintering process is driven by surface area reduction, and powders with small average particle size possess more surface area, the rate of bonding between small particles is high during the early stages of sintering. With fine particles, grain growth is also promoted in the subsequent stages after densification is nearly complete. As a result, a denser product with larger final grains is obtained when the starting powders are fine.

Figure 2.1 shows the effect of average particle size of W powders on sintered density. W powders with a size as small as 1.7 μm can be sintered to 94%TD at 1800°C within five hours [5]. On the other hand, larger W powders with a size of 4.4 μm can be sintered to merely ~80% with the same temperature and duration.

b. Temperature Effects

The sintering rate increases with temperature through the typical Arrhenius dependence of diffusion processes. For example, compacts of 4 μm W powders sintered at 1610°C and 1750°C for 20 hours have a density of 75% and 85% TD, respectively (Fig. 2.2) [5]. Hayden and Brophy [6] and Kothari [7] studied the densification of pure W over a lower range of sintering temperatures (1000-1500°C) and observed that full densification of W (1-3 μm) could not be obtained at low firing temperatures, although W powder compacts had been sintered for a considerable period of time (8 hours). The relative density of W (3 μm) compacts sintered at temperatures between 1100-1500°C, as reported by Kothari [7], is presented in Fig. 2.3.

c. Atmosphere Effects

Hydrogen-containing atmospheres are commonly used to sinter W powder compacts, to aid in oxide dissociation and removal. Moon et al. [8] studied the effects of different atmospheres on the sintering behavior of W compacts sintered at 1400°C for 4 hours, with an average starting particle size of 0.96 μm. They found that the specimens sintered in hydrogen

showed relatively high density, while those sintered in vacuum had only a modest increase in density, and densification was not observed at all in the specimens sintered in argon.

Haubner et al. suggested that in vacuum and argon environments, the volatile vapor phase oxide hydrate of the fine particles ($WO_2(OH)_2$) can form and deposit back on the surface of coarse W particles, leading to the low sinterability of powder compacts [9]. Moon and coworkers [8] however argued that the formation of gaseous tungsten oxide hydrate was unlikely in their systems where no continuous source of water vapor was present. Instead, they proposed that the W-particle coarsening, which occurred during the initial sintering stage in the sample sintered in non-reducing atmospheres, was due to the oxidation and reduction processes associated with oxide phases such as WO_2 and WO_3. For example, in a dry atmosphere, gaseous WO_3 can form more readily from relatively small W particles, and the oxide will be deposited on the surface of larger particles through the reduction of the oxide. Similar to Ostwald ripening, this transfer process is driven by the equilibrium pressure difference of particles with different sizes. As particle coarsening occurs more rapidly than neck growth accompanying a shrinkage, only slight densification is observed in the specimens sintered in argon and vacuum.

Although a hydrogen-containing atmosphere has been identified as superior for sintering of pure W, it can result in embrittlement of W alloys. For example, in the case of W-Cu-Ni heavy alloys, hydrogen atoms can segregate to the W-Cu-Ni matrix–W particle interface, causing embrittlement. To eliminate this problem, vacuum or argon annealing after sintering are recommended [10]. The production of W alloys is discussed in Section 2.2.5.

2.2.4. Activated Sintering

Because temperatures as high as 2700°C are required for W powder to achieve nearly-full sintered density in a reasonable amount of processing time, the possibility of adding small amounts of an element to the W powder to enhance its sintering kinetics and hence to reduce the sintering temperatures have been explored. A sintering additive which is insoluble in W can segregate to the contact zone between W particles, provide a high diffusivity transport path for W atoms, and consequently lower the activation energy for bulk transport of W (see Section 2.2.6).

Group VIII transition metals including Ni, Pd, Pt, Co, and Fe and some combinations of these materials are among the additives that can help activate the sintering of W [11-15].

Depending on the types of additives and sintering temperatures, the segregated phase along the grain boundaries can be either solid or liquid. For W+Ni and W+Fe binary systems with a few monolayers of Ni and Fe, the coexisting phases during sintering (above 1100°C) are W with a saturated solid solution of W in Ni, and W in equilibrium with intermetallic compounds, respectively [16]. The difference in phase equilibria as such leads to different degrees of sintering enhancement when distinct activators are employed.

Figures 2.4 and 2.5 illustrate the effects of transition element additions on the shrinkage and relative density of W at various sintering temperatures. In their study on enhanced low-temperature sintering of W in the temperature range 1100-1400°C, German and Munir [15] found that 4 monolayers of either Ni, Pd, or Pt resulted in relatively high shrinkage of W, while greater amounts of activator could hinder the densification process (Fig. 2.4). Pd, which was determined to be the best activator, could help W sinter to near-theoretical densities at temperatures as low as 1200°C. Similar sintering enhancements were observed for Fe and Co additions, but with a relatively small degree of shrinkage (Fig. 2.5). Addition of Cu, on the other hand, did not improve the sintering. It was speculated that this could be due to the low solubility of Cu in W. Additionally, the authors also observed pore rounding and grain growth, which deteriorate the shrinkage rates, as the total shrinkage of the Ni, Pd, and Fe-doped compacts exceeded ~10% (corresponding to the end of the initial sintering stage).

Solid-state sintering of W with binary additives has also been studied by Li and German [17]. Alloys containing Ni+Co in a 1:1 weight ratio and those with Ni+Fe in a 3:2 weight ratio (2 wt.% of additives; > 4 monolayers) show high sintered densities and superior mechanical properties, as these alloys avoid intermetallic phase formation during sintering. Additionally, it was reported that the addition of a small content of Ni+P alloy (0.27%) resulted in improved sinterability of W over that of W containing approximately the same amount of Ni additive (0.3%) [5].

Tungsten (W) and molybdenum (Mo) are materials with very similar characteristics, and form a solid solution at all compositions. While it is known that the addition of Mo to W can result in higher strength of the material due to solid solution strengthening, some studies have also shown that addition of Mo can improve the sinterability of W. For example, Skorokhod et al. examined the sintering behaviors of a mixture of W and Mo powders [14]. Their study shows that at the same sintering condition, Mo specimens exhibited higher density than W compacts.

By mixing W with Mo in a 1 to 1 ratio, compacts with higher density than pure W sintered under the same conditions were obtained. Similar results have been reported by Timofeeva and coworkers as they observed that the sintered density of W-Mo powder compacts sintered at 1200-2000°C for 5 hrs. increased up to about 10% when the Mo content was raised from 15 to 50 wt.% [18].

The sintering behaviors of W-Mo alloys with additives have also been investigated. Studies by Skorokhod et al. [14, 19] suggest that additions of Group VIII metals have a pronounced activating effect on the sinterability and alloy formation of W-Mo powder compacts. Bose and German [20] studied the effect of Mo content in W activated by binary additives of Ni and Fe. They proposed that addition of Mo results in reduction of W solubility which leads to a smaller grain size and solid solution strengthening. No sintering behaviors, however, were discussed in their work. Microstructure evolution of 80W-10Mo-7Ni-3Fe during the course of liquid-phase sintering has been discussed by H. D. Park and coworkers [21].

In addition to the transition metals in group VIIIB and Mo, W powders are sometimes doped with other materials, such as K, Si, Al and rare earth oxides. Rather than to enhance the sintering kinetics, these elements are introduced into W to improve the material's mechanical properties such as creep resistance [22, 23].

The effect of oxygen on sintering of a refractory metal has also been discussed in the case of Mo. Bin and Liyeh examined the effect of oxygen content in the range of 0.48-1.19 wt.% on the sintering of Mo [24] and found that oxygen could help improve the sintering and transverse rupture strength of Mo compacts. The authors noted that oxygen was largely removed in the sintering process, and the final oxygen content was independent of the initial one. The effect of oxygen on the sintering of W has not been reported.

2.2.5. Liquid-Phase Sintering

Liquid-phase sintering refers to a sintering process that involves the formation of liquid phase upon sintering. Because of the rapid diffusion of materials in the presence of a liquid phase, materials processed through liquid-phase sintering have relatively high densification rates as compared to those prepared by solid-state sintering [25]. High additive content is a general requirement for materials to be sintered with this process. The examples of W systems formed by liquid-phase sintering are W-Cu-Ni, W-Fe-Ni, W-Co-Ni, and W-Cr-Ni heavy alloys [26]. For

Cu-Ni or Fe-Ni additions, the content of W typically ranges from 80% to 96% by weight. Due to the ductile nature of the second phase that surrounds the comparably brittle W grains, W with improved ductility is usually produced by the liquid-phase sintering process. Among all systems, W heavy alloys containing an Fe-Ni binder have received the most attention due to their good mechanical properties and relatively low cost [27-29]. The temperatures used to sinter these alloys are in the range of 1460-1500°C (T_m of Ni = 1455°C; T_m of Fe = 1538°C).

2.2.6. Sintering Kinetics

It has been indicated that in the early period of initial solid-state sintering, a surface diffusion process, with a relatively low activation energy, controls the sintering kinetics of pure W powders [26]. This stage is marked by an increase of the average interparticle neck size ratio without shrinkage of the bonded particles. Several authors [6, 7, 26, 30] have suggested that grain boundary diffusion soon dominates the sintering kinetics in the initial stage. For this mechanism, an activation energy in the range of 380-460 kJ/mol has been reported [6, 7, 31]. It was suggested that impurities, such as C, P, N can have a large impact on the measured activation energy as they can segregate to W grain boundaries and decrease the atomic mobility of W [32]. For the intermediate and final stages, German suggests that grain boundary diffusion is also the dominant sintering mechanism [26].

When sintering activators, particularly group VIIIB transition elements, were added to W, it was observed that in general the transport rate of W was enhanced, as evidenced by a reduction of the activation energy for W atom diffusion [15, 33-36] Using a constant heating rate method to evaluate shrinkage, German and Munir [15] estimated the activation energy for sintering of W containing 4 monolayers of either Ni, Fe, or Co to be 280, 480, or 370 kJ/mol, respectively. Similar values of activation energy for W (200-285 KJ/mol) with comparable or higher monolayer coverage of Ni were reported by other authors [33, 35, 36].

2.2.7 Mechanical Properties of Sintered W

Several sintering variables presented earlier influence the microstructure and hence mechanical properties of sintered W products. At high sintered density, porosity, pore shape, pore size and pore uniformity all play vital roles in controlling the mechanical properties of sintered products [37]. Pores aligned on interparticle boundaries can result in stress

concentration and hence premature failure, while isolated pores within the grains can prevent sintering to full density. Pores can also, however, act as obstacles to the propagation of a brittle crack. In addition to porosity, grain size, grain shape and grain boundary cohesion also contribute to the strength of fully or nearly fully dense materials [38, 39].

As described in Section 2.2.4, sintering activators can be employed to enhance the sintering of W. Although considerable amounts of research exist showing how activators can improve the sinterability of W powders, work on the mechanical response of these materials is limited. The lack of mechanical property data in general and the lack of an optimization for sintered strength specifically are believed to be at least partly responsible for the limited industrial use of the activated sintering technique for W [17]. Two active research groups in this field are led by (i) S. Hofmann and H. Hofmann of the Max Planck Institut für Metallforschung, Germany, whose interest is the effects of impurities in W on its mechanical properties [39], and (ii) R. M. German of Pennsylvania State University, who studied mechanical behavior of activated W powder compacts [17].

Hofmann and Hofmann [39] investigated how additives segregated at the grain boundaries of W influenced the boundary cohesion and caused brittle fracture. In systems with 0.05%Ni and 0.17%Fe and with sintered density higher than 98.3% of the theoretical, the authors observed that the bend strength was in the range of 280-440 MPa, depending on the pre-annealing and cooling conditions. Although Ni and Fe could improve the sintering of tungsten, Ni, Fe as well as O were found detrimental to the cohesion of the material. Additionally, grain boundary strength was enhanced by C additives, while P decreased the cohesion substantially. The effects of P have also been noted by Ioshi and Stein [40]. They suggested that the fracture mode of W is essentially intergranular and segregation of phosphorus to the grain boundaries is responsible for embrittlement of W.

Li and German [17] investigated the mechanical response (Rockwell-A hardness and modulus of rupture) of W powder compacts with average particle size of 0.5 and 5.4 μm, doped with various concentrations of Pd, Ni, Co, Fe up to approximately 4 monolayers, and isothermally sintered at 1200, 1400, or 1600°C for 1 hour. Sintered density of the materials in the range of 59-98 %TD was obtained. Relatively high transverse rupture strength (450MPa) was observed in the sample of small-sized powder with 4 monolayers of Ni (0.29 wt.%), sintered at temperatures in the range of 1200-1400°C (Fig. 2.6). The strength of W compacts doped with

Ni and Pd decreased with increasing temperature due to grain growth at higher temperatures. On the other hand, W compacts doped with Co and Fe exhibited relatively low sintered density, and the strength of these compacts increased with temperature as the sintered density of the specimens was enhanced (Fig. 2.6). Brittle fractures were observed in all specimens.

Li and German also extended their work to consider binary additives [16]. They found that binary additives in general lead to better densification than single additives, and transverse rupture strength of these systems could be as high as 600 MPa. Figures 2.7a and 2.7b show the densification and hardness of ternary alloys of W with 2 wt.% (>4 monolayers) of either Ni, Fe, Co, or some binary combination of these additives, sintered at 1300°C and 1500°C. From the figures, it is observed that a W compact containing Ni, sintered at 1300°C, has relatively high densification and hardness. However, when the firing temperature is increased to 1500°C, the hardness of the material becomes relatively low, because hardness is controlled by grain size at high density. Additionally, Li and German observed that the mode of failure in some of the samples with Ni-Co and Ni-Fe (~7:3 ratio) was ductile, rather than the brittle fracture typically observed in untreated W and W containing a single additive.

Unlike W processed by activated solid-state sintering, since the development of W-Ni-Fe heavy alloys with 78-98 wt. % W and a Ni:Fe ratio of 7:3 in the 1940's, a great amount of attention has been given to the investigation of fracture behavior of W heavy alloys and of how various variables in the liquid-phase sintering process affect mechanical properties [27, 38, 41-44]. The mechanical properties of theses alloys depend on the strength and ductility of both the W and the binder phase, and on the cohesive strength of the W-W and W-binder interfaces. Some of the causes that degrade the alloys' properties are residual porosity, impurity segregation, hydrogen embrittlement, intermetallic phase formation, and W precipitation in the matrix.

2.3 Concluding Remarks

Various sintering techniques, including solid-state and liquid-phase, have been developed for consolidating W powder or W alloy powders, typically to nearly full density. For solid-state sintering, W can be sintered almost to full density either at very high temperatures (~2700°C) or at lower temperatures (~1500 °C) with the addition of sintering activators such as Ni and Fe. Some studies however indicate that activators may deteriorate the mechanical properties of W at high sintered density, and this may prevent a general usage of the technique. On the other hand, it is plausible that the activated sintering technique with relatively low contents of additives could be both useful and feasible for applications where relatively low firing temperatures (<1200 °C) and only partially-complete sintering of W are required.

In the next chapter, sintering kinetics, the influences of sintering variables, and corresponding mechanical properties of partially-sintered W in relation to minority contents of sintering activators, namely Ni and Fe (<3 monolayers), will be investigated. These experiments will help us gain a better understanding of these subjects and verify the feasibility of the activated sintering technique at low firing temperatures. In addition to a novel study of the influence of additives content (few monolayers and below) on sintering behavior of W fired at low temperatures, Ch. III presents the first experimental work to determine the relationships between sintering parameters, microstructure, and mechanical response (both hardness and fracture toughness) of partially-sintered materials.

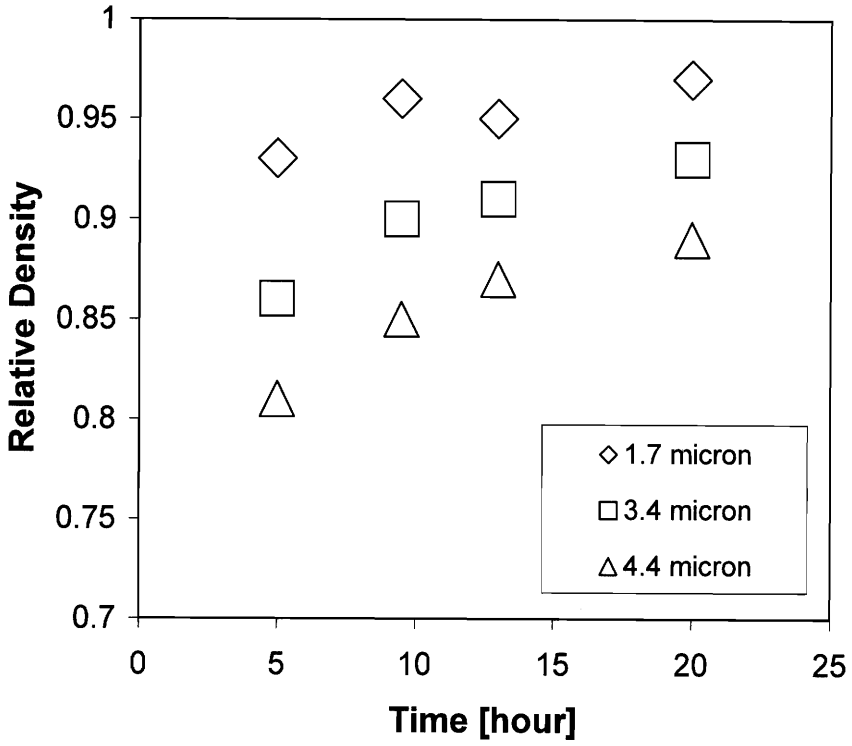

Fig. 2.1: Sintered density as a function of sintering period at 1800°C for W powders of different average particle size. The data is reported in Ref. [5].

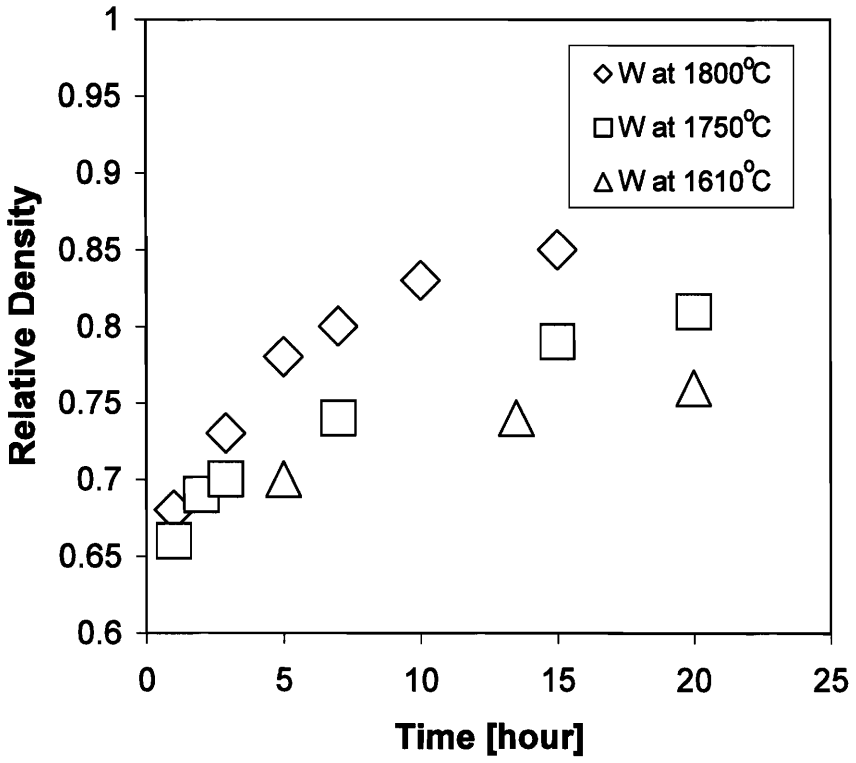

Fig. 2.2: Sintered density of W (4μm average particle size) as a function of sintering period at different temperatures. The data is reported in Ref. [5].

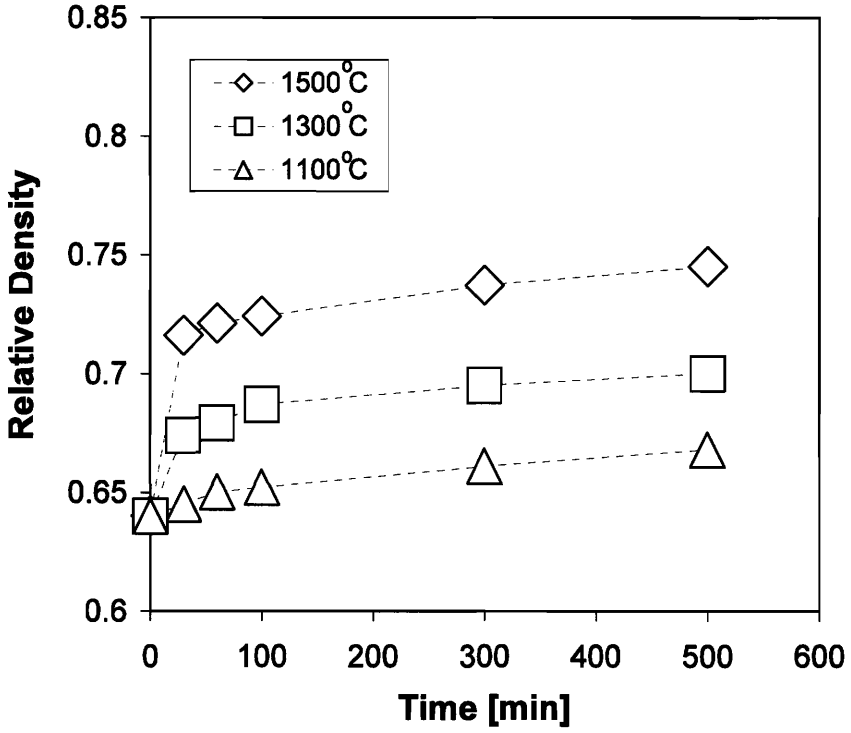

Fig. 2.3: Sintered density of W (3 μm average particle size) processed at low firing temperatures (1100-1500°C), as a function of sintering period. The data is reported in Ref. [7].

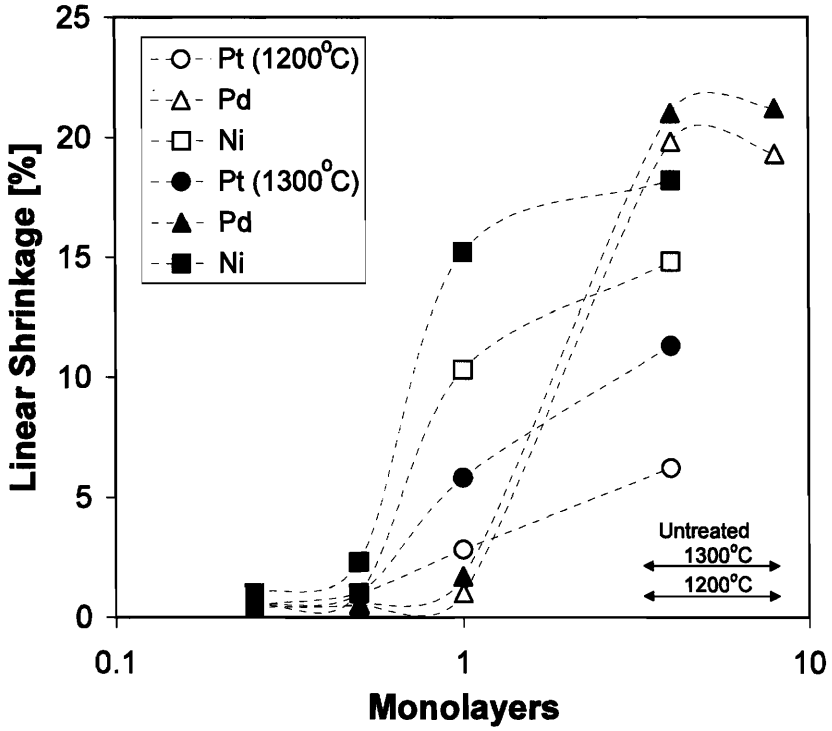

Fig. 2.4: Shrinkage data for a 0.5 μm W powder sintered for 1 hr. versus the content of activator for three transition metal additives. The data is reported in Ref. [15].

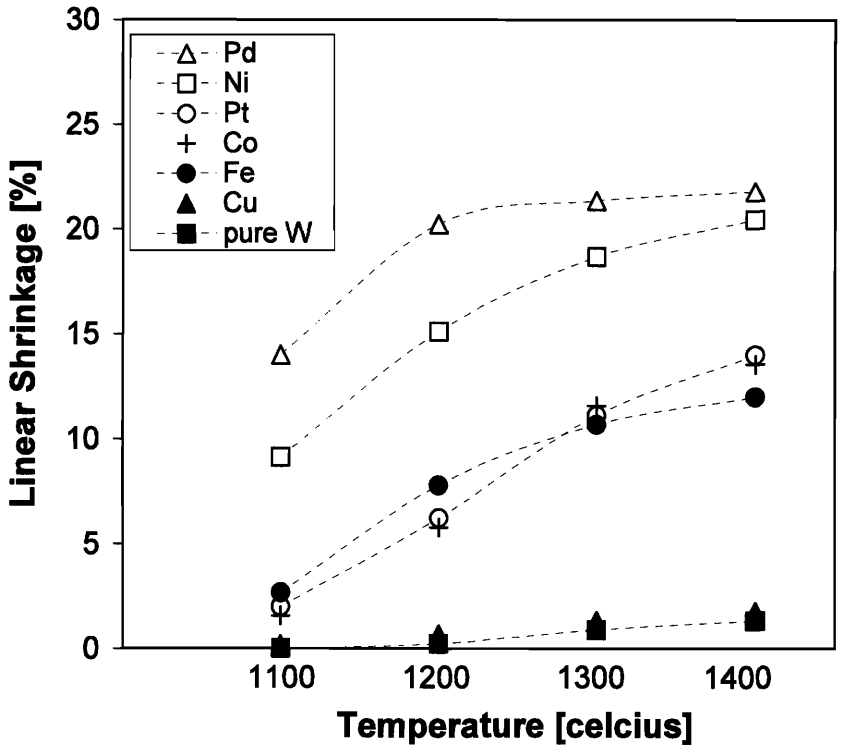

Fig. 2.5: Shrinkage and density data for a 0.5 μm W powder with four monolayers of additives sintered at various temperatures for 1 hr. The data is reported in Ref. [15].

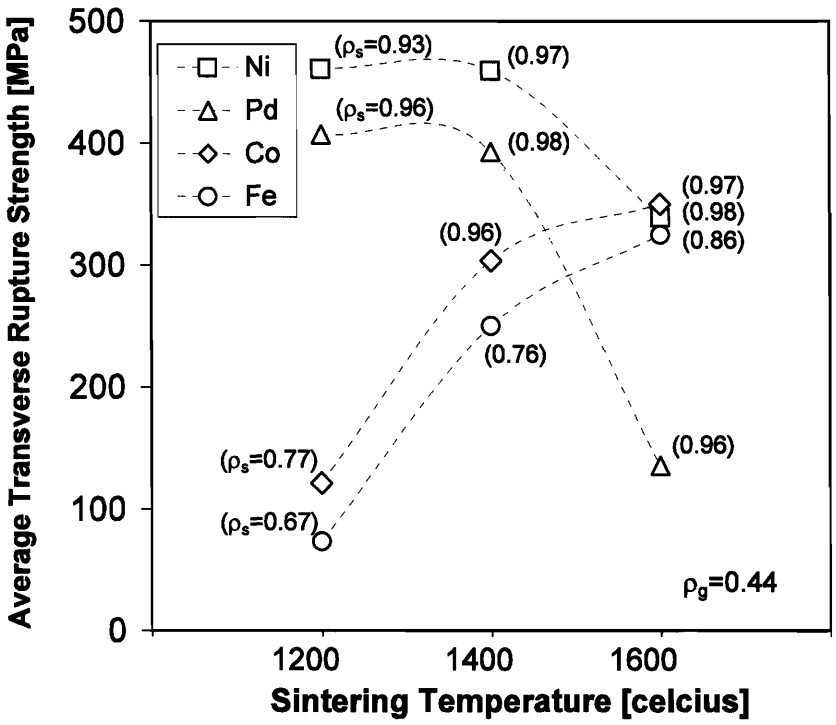

Fig. 2.6: Transverse rupture strength of W powder compacts (0.5 μm) activated by approximately 4 monolayers of Ni, Pd, Co or Fe, and processed at the various temperatures for 1 hour. The data is reported in Ref. [17].

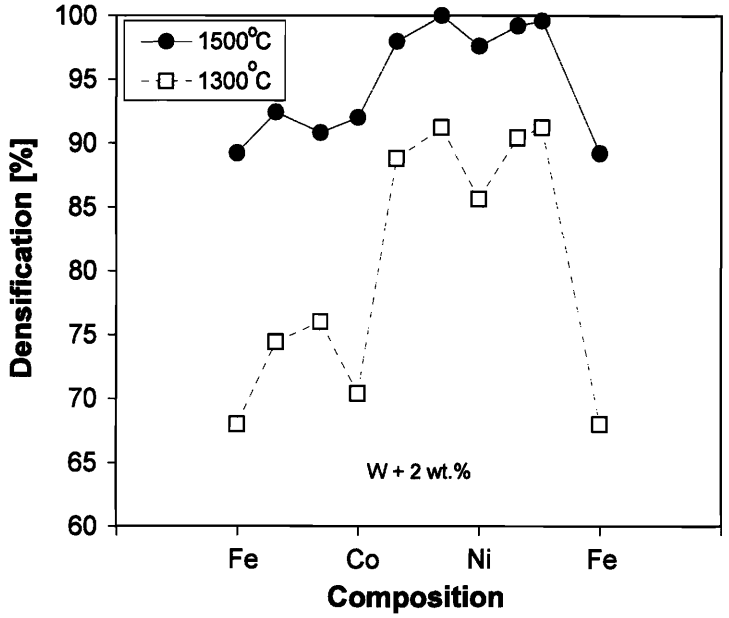

(a)

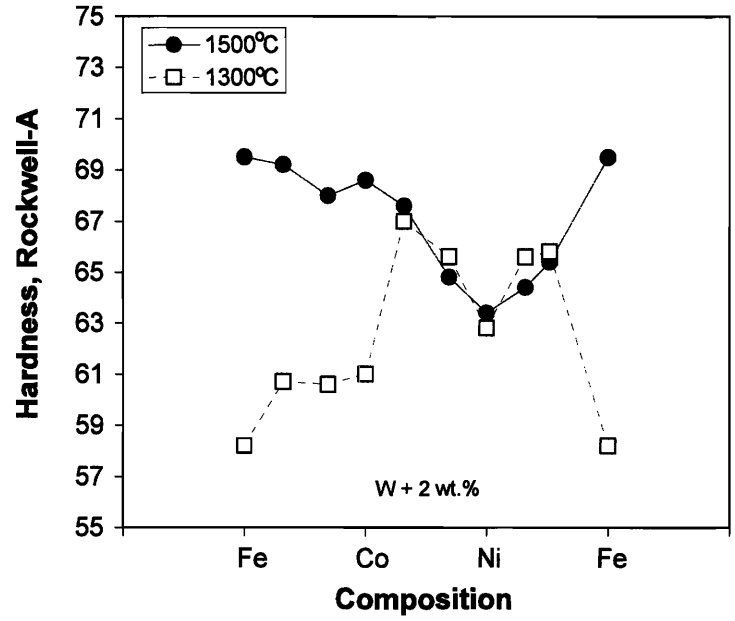

(b)

Figs. 2.7a-b: (a) Densification and (b) Rockwell-A hardness versus composition of W (0.44 μm) binary and ternary alloys sintered at 1300°C and 1500°C for 1 hr. The data is reported in Ref. [16].

Chapter III. Sintering of W at Low Temperatures

3.1 Introduction

The sintering process can be described by three sequential stages, namely the initial, intermediate and final stages of sintering. It is clear that in many applications it is desirable to sinter powder materials through all sintering stages to full density, such that optimum strength is achieved. In some applications, however, full sintering is not required or may even be undesirable from the point of view of property control or economics. For example, a sintered ceramic shell used in investment casting needs to contain some porosity, so that (i) steams can be transferred through the mold during the autoclave operation, and so that (ii) water vapor and entrapped gas can migrate out of the mold, and (iii) adequate thermal transfer can be maintained during metal casting process [45, 46]. Anode substrates for solid oxide fuel cells can be processed by tape casting and sintering, and require a high residual porosity level so that fuel can reach the electrolyte interface [47-49]. Finally, melt-infiltration processes for fabrication of metal matrix composites require a partially-sintered porous perform with fully open porosity [50].

The fabrication of partially-sintered W with a continuous network of pores could potentially be useful for a variety of applications including those mentioned above. A specific example will be discussed later in Chapter V, where the use of partially-sintered W in investment casting applications is discussed. To fabricate initial-stage sintered W, W powder can be consolidated at firing temperatures lower than typical processing temperatures. With the addition of minority content of sintering activators, the processing temperature could be as low as ~1200°C. By modifying the content of sintering activators, it is plausible that the microstructure of the sintered material and its corresponding mechanical properties could be manipulated.

The main objective of this chapter is to examine the processing-microstructure-property relationships of partially-sintered W processed at low temperatures. In the next section, the influences of sintering variables including sintering activator content, firing time and firing temperatures will be investigated in the context of sintering kinetics and mechanisms. Section 3.3 is concerned with the mechanical response of partially-sintered W, which is examined in

relation to processing variables and sintered microstructure. While this study is specifically applicable to W, the understanding developed here can also be applied to other partially-sintered material systems.

3.2 Activated Sintering and Sintering Kinetics of W

3.2.1 Introduction

As discussed in Chapter II, the activated sintering technique can be employed to enhance the sintering kinetics of a material, such that it can be sintered at relatively low firing temperatures. For W, the sintering activators include Ni, Fe, Co, and Pd. In this section, the incorporation of very small amounts of Ni and Fe (<3 monolayers) is examined in W compacts. The focus of the study is on the types and contents of sintering activators, and how these may influence the sintering behavior and kinetics of W processed at low firing temperatures.

3.2.2 Experimental Procedure

High purity W powder manufactured by GE Lighting Components (Cleveland, OH) is used in the study. To distinguish W powder of this set from others which will be used in later sections, the powder will be labeled 'series A'. The powder has a mean particle size of 1.2 μm, and its particle size distribution and some additional characteristics are presented in Fig. 3.1 and Table 3.1, respectively. Various contents of either Ni, Fe, or both Ni and Fe (1:3 and 3:2 weight ratios) additives, ranging approximately from 0.01% to 0.18% by weight, were incorporated into the base powder, resulting in 0.6, 1.3 or 2.6 average monolayer coverage of the sintering activators on the W surface of W powders. The average monolayer coverage parameter, $\bar{M}$, is calculated by integrating monolayer coverage over the particle size distribution, assuming spherical particles:

$$\bar{M} = \frac{\int P(r) \cdot \frac{r}{2a} [(1 + \frac{c}{1-c} \cdot \frac{\rho_w}{\rho_a})^{\frac{1}{3}} - 1] \, dr}{\int P(r) \, dr} \qquad (3.1)$$

where r is the particle radius of W, P(r) is the number population of W powders at any particle size, c and a are the concentration and atomic radius of sintering activators, respectively, and ρ_w

and ρ_a are theoretical densities of W and additives. Sintering activators generally can be added to W with an aqueous deposition method [12, 17] or a dry mixing method [51]. While the first can result in a more uniform coating, the latter is practically useful for an industrial setting and thus was chosen for this study. In particular, Ni (2.2-3 μm) and Fe (1-3 μm) powders were added to the W powder and the materials were mixed in a high energy powder mixer for approximately 30 minutes.

Following dry mixing, green compact specimens were prepared using a single-action cold press and a stainless-steel die of rectangular cross section. A compaction pressure of 21 MPa was employed, resulting in compact densities of about 50 % of theoretical density (TD). These green specimens were then sintered in a furnace programmed with a heating rate of approximately 5° C/min and an isothermal hold at 1177° C for either 0.5, 1 or 2 hours. Additionally, some sets of specimens were sintered isothermally at 1200° C and 1250° C for 0.5 hours. In all cases, slow furnace cooling was employed after firing. To prevent the oxidation of W, the processing was carried out in a dry 3% H_2-97% N_2 atmosphere. The geometry of the fired specimens was approximately 24 x 8 x 3 mm, as shown for some typical test specimens in Fig. 3.2. At least two specimens were prepared for each processing condition. After sintering, sintering properties including linear shrinkage ($\Delta L/L_o$) and sintered density (ρ_s) could be determined from the measured dimensions of the as-fired specimens.

3.2.3 Analysis of Sintering Kinetics

The activation energy for diffusion of W atoms can be estimated by examining their sintering kinetics. In the initial stage of sintering, linear shrinkage of a material may be assumed to follow [3]:

$$\frac{\Delta L}{L_0} = \left(\frac{Kt}{T}\right)^m \tag{3.2}$$

where

$$K = B\exp(\frac{-Q}{R_g T}), \tag{3.3}$$

B is a constant which relates to diffusivity, surface energy, atomic volume, and particle size, t is time, T is temperature, Q is activation energy for atomic diffusion, R_g is the gas constant (8.3 J/mol-K), and m is a sintering exponent whose value depends on the dominant diffusion mechanism. For grain boundary diffusion, volume diffusion and viscous flow, the values of m are 1/3, 1/2, and 1 respectively [3]. According to Eqn. (3.2), 'm' can be evaluated from the slope of a log-log plot of shrinkage versus time at a constant temperature. Using a fixed value of linear shrinkage and corresponding sintering time presented in isothermal log-log shrinkage-time plots, the value of K can also be determined. Finally, from Eqn. (3.3), the value of 'Q/R_g' can be obtained from the slope of a ln(K) - 1/T plot [52, 53].

3.2.4 Results and Discussion

Fig. 3.3 shows the linear shrinkage of W specimens prepared at 1177° C for 1 hour as a function of the types and contents of additives. For all specimens containing additives, sinterability was enhanced over that of the pure W specimen, whose linear shrinkage and sintered density were respectively 0.5% and 51.4%TD. The data also show that Ni is a very effective sintering activator as compared to Fe, and that the sintering of W is enhanced with increasing amount of Ni added. On the other hand, sintering improved with an increase of Fe content until it reached 2.6 monolayers, after which a drop in linear shrinkage and density was detected. The observation that Ni helps activate the sintering of W much better than Fe agrees well with prior studies [15, 16]. With the use of 2.6 monolayers of Ni, which is the maximum impurity content employed in this study, maximum shrinkage and sintered density of 7.8% and 65.4%TD, respectively, were obtained.

Activated sintering process was enabled when both Ni and Fe were used together, (Fig. 3.3). With the same monolayer coverage, W specimens containing both Ni and Fe additives with the weight ratio of 3:2 appeared to sinter better than those with 1Ni:3Fe. This may be due to the higher content of Ni, the superior activator, present in the first case. Alternatively, this may be explained by considering the co-existing phases of the materials upon sintering, using a W-Ni-Fe pseudo-binary phase diagram [54, 55]. Unlike W with 1Ni:3Fe additive, that with 3Ni:2Fe additive avoids the formation of intermetallic phases, which can inhibit W transport during sintering. Consequently, it may be expected that the activation energy for diffusion of W atoms is relatively low for W with 3Ni:2Fe additive. From the experiment, it was also observed that

the degree of sintering of W was generally higher in the case of specimens containing only Ni additives, as compared to those with both Ni and Fe of the same total monolayer coverage. It should be noted that with the use of different additive incorporation procedures and additive particle sizes, the degree of mixing of Ni and Fe and how they distribute on W particles may vary, and consequently differences in the relative degree of sintering enhancement may be observed when different processing procedures are employed [51].

Fig. 3.4 shows a log-log shrinkage vs. time plot of W specimens that contained 0, 0.6, and 1.3 monolayer of Ni additive and were sintered at 1177° C for 0.5, 1, and 2 hours. In Fig. 3.5, shrinkage of the specimens prepared at 1177, 1200, and 1250° C for 0.5 hour is presented as a function of processing temperature. These two figures indicate that sintering of W was improved with an increase of sintering time or temperature, as expected. The data shown in Fig. 3.4 and Fig. 3.5 can be presented in the same plot for each set of specimens, as exemplified in Fig. 3.6 for the case of W containing 1.3 monolayer Ni. Assuming that the controlling diffusion mechanism is the same in this low range of sintering temperatures (1177-1250° C), trendlines parallel to the one for 1177° C may be drawn on the plot (Fig. 3.6). The value of 'K' at different processing temperature was determined by using Eq. (3.2) and the data presented in Fig. 3.6. (i.e., sintering exponent, temperatures, a fixed value of shrinkage, and corresponding sintering times). The resulting K for all different specimen sets were plotted as a function of 1/T in Fig. 3.7, and the slopes of those curves yielded Q, the activation energy. The results of Q and m of each specimen sets are tabulated in Table 3.2.

For the case of W without additives, the slope of the plot, which corresponds to the sintering exponent 'm', was determined to be 0.40. This is comparable to the expected value of sintering exponent for grain boundary diffusion mechanism (0.33), and therefore it is suggestive that, for the case of pure W, the dominant diffusion mechanism involves the transportation of W atoms from grain boundaries (i.e., interparticle boundaries) to interparticle neck regions. The activation energy for this process was determined to be 404 KJ/mol, in agreement with prior studies which reported the activation energy for sintering of pure W between 380-460 KJ/mol [6, 7, 31].

As a minority content of Ni (0.6 monolayers) was introduced, the shrinkage exponent was found to increase from that observed in the pure W case to 0.64. This value is close to the shrinkage exponent proposed for the volume diffusion mechanism (0.50). The deviation of the

experimental shrinkage exponent from the predicted value may possibly be attributed to competitive diffusion mechanisms that occurred simultaneously. The apparent activation energy in this case was found to be 406 KJ/mol, which is comparable to that observed in the case of pure W. The results, therefore, suggest that when a minimal content of Ni was introduced to W, the dominant diffusion mechanism starts to shift from grain boundary diffusion to volume diffusion which involves the migration of diffusing species from grain boundary to neck surface through the particle interior. In this case, the particle "interior" is probably the activator-rich surface region. With this very small content of Ni, the increase in diffusion rate arises from the change of dominant transport mechanism without an observable change in activation energy.

When the content of Ni additive was increased to 1.3 monolayers, the shrinkage exponent was determined to be 0.66, which was similar to the case with lower Ni content. This suggests a similar material transport mechanism. The activation energy for diffusion, however, was found to decrease significantly to 315 KJ/mol. With this reduction in energy barrier for diffusion, the sintering kinetics of W containing 1.3 monolayers of Ni was therefore much faster than that with 0.6 monolayers. Comparing the results obtained here with the activation energy for sintering of W with 4 monolayers of Ni, 280 KJ/mol as reported by German and Munir [15], it can be seen that activation energy is reduced with an increasing activator content.

3.2.5 Summary

The study performed in this section illustrates that sintering of W can be improved with the addition of very small contents, particularly less than 3 monolayers, of either Ni or Fe, or a combination of both Ni and Fe. Using a dry-mixing technique, it was observed that Ni was superior to other activators in enhancing the sintering kinetics of W compacts. The shrinkage exponent, which relates to the diffusion mechanism, increased at once with the addition of Ni even when the content was below 1 monolayer coverage. With increasing content of Ni, a reduction of the activation energy and hence an increase of the diffusion coefficient were observed. Despite the improved degree of sintering, the W specimens processed at our chosen additive contents and at low firing temperatures were only in the initial stage of sintering, as indicated by their low sintered density. The microstructural features and corresponding properties of these partially-sintered materials will be discussed subsequently.

3.3 Mechanical Properties of Partially-Sintered W

3.3.1 Introduction

As discussed in the previous section, the use of minimal sintering activator content and low processing temperatures for W compacts results in materials which are sintered only partially, and contain a continuous network of pores. It can be expected that the mechanical properties of such materials rely on the transmission of stress across interparticle necks of the partially-sintered powder particles. While a large number of publications have concentrated on the mechanical response of highly-densified sintered materials [20, 27, 56-61], fundamental studies on the mechanical properties of those with low sintered density (i.e., sintered only in the initial stage) are much more limited [62-65]. It is the purpose of this section to examine the mechanical properties of partially sintered W, particularly hardness and fracture toughness, and to clarify the relationships between material properties, sintering parameters, and microstructure.

3.3.2 Analytical

Arato et al. were one of the first groups to consider the mechanical properties of partially-sintered materials in relation to their microstructure [62]. They derived an analytical scaling relationship for elastic modulus through the determination of forces acting across particle contacts and on a reference plane through the structure, using a Voigt average for the elastic properties of a polycrystalline body. The resulting expression for Young's modulus is nominally valid for the initial stage of sintering [66]:

$$E = E_0 \frac{z}{4} \rho_s \left(\frac{r}{R} \right)^2 \tag{3.4}$$

Here E and E_o are the Young's moduli of partially-sintered and fully-dense material, respectively, z is the average coordination number of the sintering particles of mean radius R, ρ_s is the fractional sintered density (relative density), and r is the interparticle neck radius. The dimensionless ratio r/R will be termed the "relative neck radius". Arato et al. further suggested that the hardness of a partially-sintered compact, H, would scale similarly:

$$H = \frac{E}{E_o} H_o \tag{3.5}$$

where H_o is hardness of the fully-dense material. The general scaling of Eq. (3.5) has been experimentally validated by Luo and Stevens [64], who measured the bulk modulus and hardness

of stabilized zirconia sintered to densities $\rho_s = 0.6 - 1.0$. Combining Eqs. (3.4) and (3.5), the hardness of partially-sintered material may also be written as:

$$H = \left(\frac{z}{4} \cdot \rho_s \cdot \left(\frac{r}{R} \right)^2 \right) H_o \tag{3.6}$$

Eqs. (3.4) and (3.6) give simple scaling relationships for modulus and hardness with respect to the density of a partially-sintered compact. However, the microstructural state variables z and r/R also evolve with sintered density, and must be modeled to reduce the above expressions to simple functions of ρ_s. For example, Arato et al. used Fischmeister and Arzt's model [67, 68] for the densification of an irregular packing of spherical particles to capture the evolution of *z* and r/R as a function of the sintering profile (density), and compared the resulting model with hardness measurements performed on Si_3N_4-based sintered compacts having sintered density in the range $\rho_s = 0.6 - 0.9$. The results from the experiments were found to be in good agreement with the predictions of Eqs. (3.4) and (3.6).

In addition to their discussion of hardness, Arato et al. also modeled the fracture toughness, K_{IC}, of partially-sintered brittle materials using Griffith's fracture theory:

$$K_{IC} = \sigma_o R^{1/2} \frac{E}{E_o} = \sigma_o R^{1/2} \left(\frac{z}{4} \cdot \rho_s \cdot \left(\frac{r}{R} \right)^2 \right) \tag{3.7}$$

In Eq. (3.7), σ_o is the theoretical tensile strength of flaw-free fully-dense material. Fracture toughness was also considered later by Green and Hardy [63], who derived a different theoretical model for partially-sintered brittle materials by modifying existing models for fracture toughness of cellular ceramics [69]. With the assumption that partially-sintered particles fail by a crack passing through sintered interparticle contacts (i.e., necks) and that one contact is broken at a time, the authors argued that tensile stress, σ, acting on an unbroken neck ahead of a crack is responsible for fracture of the material, and is given by:

$$\sigma = \left(\frac{2}{\pi} \right)^{1/2} \left(\frac{K_I}{\pi r^2} \right) (2R)^{3/2} \tag{3.8}$$

where K_I is the stress intensity factor in mode I loading. As σ is increased and reaches the intrinsic strength of the neck, σ_o, fracture occurs, and the critical stress intensity is written as:

$$K_{IC} = C_o \sigma_o R^{1/2} \left(\frac{r}{R} \right)^2 \tag{3.9}$$

where $C_o \approx 1.4$ is a numerical constant. Unlike Arato et al.'s model (Eq. (3.7)), Green and Hardy's solution in Eq. (3.9) does not contain an explicit sintered density dependency, and, as before, a microstructual model is required to link R and r/R to ρ_s. However, neither of these two models has been rigorously tested against experimental data. Green and Hardy did examine the fracture toughness of sintered alumina over a relatively narrow range 58-64 %TD, and found reasonable agreement with the form of Eq. (3.9). However, in the narrow range of sintered densities they investigated, their model (Eq. 3.9) and Arato et al.'s (Eq. 3.7) give very similar predictions.

Despite the differences among the various analytical models described above, it can be observed that they all contain an explicit dependence on the relative neck radius. This highlights the importance of neck formation on the evolution of strength in the initial stage of sintering. Several expressions for the relationship between the relative neck radius, r/R, and sintered density, ρ_s, have been proposed, some of which are shown in Table 3.3 and plotted as a function of sintered density, for the case of sintered materials with green density $\rho_g = 0.5$ and 0.64, in Fig. 3.8 [67, 68, 70, 71]. As shown in the figure, all four models suggest a monotonic increase of relative neck radius with sintered density. In the initial stage of sintering of concern to this work ($0.5 < \rho_s < 0.75$), the predicted r/R is significantly different from one model to another. In the later stages of sintering, these differences become even more pronounced; compared to the expected limit r/R → 1 as ρ_s → 1, the relationships of Fischmeister and Arzt [67, 68] and Helle et al. [71] underestimate the relative interparticle neck radius, while Skorokhod's initial stage model [70] overestimates it.

Most of the relationships presented in Table 3.3 can be explicitly expressed in terms of *densification*, $\tilde{\rho}$, – a sintering parameter that is defined as the relative change of density with respect to the green density, ρ_g (i.e., compact density), according to:

$$\tilde{\rho} = \frac{(\rho_s - \rho_g)}{(1 - \rho_g)} \tag{3.10}$$

For example, Skorokhod's model may be written as:

$$\left(\frac{r}{R}\right)^2 = 1 - \left(\frac{1-\rho_g}{1-\rho_s}\right)^{4/3} = 1 - (1-\tilde{\rho})^{4/3} \tag{3.11}$$

This signifies that densification, $\widetilde{\rho}$, may be regarded as a sintering parameter that describes the relative interparticle neck radius of sintered materials. Two sets of sintered materials can be sintered to very different levels of sintered density, but to the same *densification* (and hence the same degree of relative neck radius), provided they have different green densities.

Another variable that enters into Eqs. (3.4), (3.6) and (3.7), is the average coordination number of sintered particles, z, which increases as the structure forms new contacts upon sintering. Several models have been proposed for z as a function of sintered density; they are presented in Table 3.4 and Fig. 3.9 [25, 67, 68, 72]. Due to geometric constraints, the minimum and maximum coordination number that mono-sized spherical particles can exhibit is 6 and 14, respectively. Unlike r/R, the values of z as predicted by different models do not differ from one another significantly in the lower range of sintered density relevant to initial stage sintering ($0.5 < \rho_s < 0.75$).

To briefly summarize, various models have been proposed to describe the relationship between sintering behavior and mechanical properties of partially-sintered materials. However, some such models exhibit fundamentally distinct scaling from one another, even for the same predicted property. Furthermore, experimental works performed to justify these models are very limited and not conclusive. In this section, the experimental study aimed at a quantitative evaluation of both the hardness model proposed by Arato et al. and the fracture toughness models proposed by Arato et al. and Green and Hardy is presented. The investigation is performed on partially-sintered W containing minority additions of sintering activators, and with a broad range of sintered density as well as densification. Similar to the situation for other sintered material systems, studies of the mechanical properties of partially-sintered W are very limited [17]. The first study on Vickers hardness and fracture toughness of W produced by activated sintering will be presented in this section.

3.3.3 Experimental Procedure

To examine the contribution of powder characteristics to sintering behavior and mechanical properties, two series of W powders were used in this section of the study. The first one is series A powder, which was employed in the earlier sections of this chapter. The second powder will be labeled 'series B'. This powder was manufactured by Alldyne Powder Technologies (Huntsville, AL) and had mean particle size of 1.7 μm, somewhat larger than that

of series A powder (1.2 μm). The particle size distribution and some characteristics of the two series of W powders are presented in Figs. 3.1a-b and Table 3.1, respectively. Due to the different particle size distributions of the two powders, the tap densities of powders A and B were very distinct (see Table 3.1).

In order to manipulate the sintering properties of these powders, various minority additions of sintering activators were added to the W powder by dry mixing. Note that the same set of activated series-A W specimens prepared in the last section is used here in this section for investigation of mechanical response. As for series-B powder, Ni powder (2.2-3 μm) was added to the base powder to achieve 0.3, 0.6, 1 and 2 monolayer coverage. It should be noted that a small initial content of sintering activators (Ni and Fe) was also present as impurities in powder B (Table 3.1). The same compaction and firing procedures used to prepare series-A W compacts in the previous section were employed for the fabrication of series-B compacts. With a compaction pressure of 21 MPa, approximate compact densities of 50 and 64 %TD in series-A and series-B specimens were obtained, respectively.

Sintering properties including linear shrinkage ($\Delta L/L_o$), sintered density (ρ_s) and densification ($\tilde{\rho}$) were determined from the measured dimensions of the as-fired specimens. As will be discussed in more detail later, the two chosen series of W powders with processing parameters as described resulted in specimens with a broad range of sintered density and densification in the initial stage, ranging over ρ_s = 0.51-0.75, and $\tilde{\rho}$ = 0.03-0.31, respectively. Hardness measurements were performed using a Vickers micro-indenter with a load of 100 g. To measure fracture toughness, the single-edge notched three point bending test [73, 74] was conducted on test specimens containing a notch cut by a diamond knife with an approximate depth of 1 mm. For every mechanical property reported, at least two identical specimens were prepared and tested. In the case of hardness, the reported values are the averages of at least four measurements.

3.3.4 Results

The linear shrinkage of series-A and -B specimens after sintering is shown in Fig. 3.10. In both series, the maximum shrinkage is observed for the highest content of Ni additive (0.18 wt.% (2.6 monolayer) and 0.10 wt.% (2 monolayer) for series A and B, respectively). In the range of low density of concern here, sintering shrinkage relates linearly to sintered density. Due

to their relatively higher green density, series-B specimens exhibited higher sintered densities even while they experienced a very small degree of shrinkage. The results in Fig. 3.10 also suggest that the correlation of shrinkage and sintered density is independent of the particular activators added, as the various points collected there correspond to specimens with Ni, Fe and Ni+Fe additions.

Figures 3.11a-d present the microstructure of fired specimens prepared with powders A and B which experienced the smallest (a, c) and largest (b, d) sintering shrinkage. The micrographs clearly show that with increasing content of sintering activators, the bonding between W particles is promoted. At the maximum content of sintering activators employed, irregular pore shapes can still be observed in both series of specimens, indicating that sintering remains in the initial stage.

The hardness and fracture toughness of the specimens as a function of the sintering activator concentration are respectively shown in Figs. 3.12a and 3.12b, using for the latter quantity the monolayer coverage of activators, $\overline{M}$, on the surface of W powders. With a slight increase of the sintering activator concentration (amounting to only a few monolayers), the hardness and fracture toughness of the specimens in both series increased considerably (Figs. 3.12a and 3.12b), and roughly in proportion to the sintered density (Figs. 3.13a and 3.13b). The exception to this observation is the specimens in series A that contained Fe, whose toughness slightly declined at relatively high content of Fe. As shown in Figs. 3.13a and 3.13b the hardness and fracture toughness of the specimens was essentially zero at the green density, and increased monotonically with sintered density, even though different combinations of sintering activators were used. The results therefore suggest that hardness and fracture toughness are dominated by the evolution of the partially-sintered microstructures of the specimens, which is in turn influenced by the sintering activators, Ni and Fe; the direct effect of a small concentration of the additives on hardness is not obviously significant.

The fracture surfaces of the specimens employed in the fracture test were analyzed in a scanning electron microscope, and it was observed that the specimens cracked in brittle mode. Particularly, the surfaces of particles across the fracture surface were smooth and no ductile dimples were apparent on the surfaces. The fracture appears to occur along sintered contacts in brittle fashion, in agreement with the high ductile-to-brittle temperature of W [75].

3.3.5 Discussion

It can be deduced from Figs. 3.13a and 3.13b that sintered density is a poor microstructural state variable with which to predict mechanical properties of partially-sintered W, because this parameter alone does not account for the microstructural evolution that occurs upon sintering from different green densities. Consequently, different parameters are required to predict the properties of the material. In this section, the applicability of scaling factors for hardness and toughness, proposed in the various models as described earlier in Section 3.3.2 will be examined.

To compare Arato et al.'s and Green and Hardy's models to our experimental data, some knowledge of z and r/R is essential. Since the values of the average coordination number, z, proposed in different models do not differ significantly from one another, as shown in Fig. 3.9, it is assumed here that z follows Fischmeister and Arzt's model. The models for r/R, on the other hand, are somewhat different from one another (Fig. 3.8). To justify a choice of model to be used here, the relative neck radius from two sets of specimens, one from each powder series, was measured. This was accomplished by measuring particle size and interparticle neck size of over 100 sintered particles of each set from scanning electron micrographs. The average and standard deviation of the measurements are shown in Fig. 3.8. The relative neck radius of specimens from both experimental sets matches fairly well with that given in Skorokhod's "all-stage" model. Furthermore, Skorokhod's all-stage model is the only one which appropriately extrapolates to r/R = 1 at full density. For these reasons, Skorokhod's model was chosen for the comparisons that follow.

a. Hardness

A first attempt to normalize hardness for the effect of green density is shown in Fig. 3.14, where the hardness of the specimens in series A and B is plotted as a function of densification. However, just as was observed in Fig. 3.13a, two distinct curves can be discerned for series A and B, although they appropriately converge to a hardness of zero as densification decreases. Densification alone therefore does not explicitly predict the hardness of the material, and we therefore turn to a more complex normalization based on Arato et al.'s model (Eq. (3.6)).

Introducing Skorokhod's model for relative neck radius (Eq. (3.11)) into Arato et al.'s hardness model (Eq. (3.6)), we see that hardness is proportional to $z\rho_s(1-(1-\tilde{\rho})^{4/3})$. Our

experimental data is plotted as a function of this scaling factor in Fig. 3.15. From the figure, it is found that the two separable trends observed earlier for powders A and B in Figs. 3.13a and 3.14 collapse into a single, monotonic trend in Fig. 3.15. This result signifies that hardness of partially-sintered W cannot be predicted knowing either sintered density or densification alone, but is related to both sintering parameters; Arato et al.'s model reasonably captures the hardness evolution of our partially sintered materials.

b. Fracture Toughness

We first compare our data to Arato et al.'s model for fracture toughness. Examining Eqs. (3.6) and (3.7), we observe that the scaling factor for fracture toughness proposed by Arato et al. has a similar form as that of hardness, with $K_{IC} \propto R^{1/2} z \rho_s (1-(1-\tilde{\rho})^{4/3})$. The fracture toughness of W normalized by $R^{1/2}$ is plotted as a function of this factor in Fig. 3.16. Unfortunately, Arato et al.'s model neither convincingly linearizes our data nor collapses the two data series into a single trend. While the two trendlines start from the origin, they deviate from one another as the value on the x-axis increases.

To examine the applicability of Green and Hardy's fracture toughness model, which suggests a more explicit dependence of fracture toughness on interparticle neck size (Eq. (3.9)), we plot $K_{IC}/R^{1/2}$ as a function of $(1-(1-\tilde{\rho})^{4/3})$, which is equivalent to $(r/R)^2$ according to Eq. (3.11). The result presented in Fig. 3.17 exhibits data that are reasonably aligned in a single monotonic trend. The toughness extends to zero as interparticle neck size decreases to zero, as expected, and increases linearly with the increase of neck size, in agreement with Green and Hardy's model. This trend underscores the importance of interparticle neck size on fracture toughness and that fracture toughness is related to a scaling factor of $(r/R)^2$. It can also be shown that the factor $(1-(1-\tilde{\rho})^{4/3})$ is approximately equivalent to $1.3\tilde{\rho}$, and hence fracture toughness of partially-sintered W may in many cases be adequately described using only the densification parameter and the mean particle size R.

3.3.6 Summary

The addition of sintering activators, namely Ni and Fe, resulted in improved sintering of W. In the regime of low sintering activator content and low processing temperatures chosen for this study, activated W compacts were partially-sintered and remained in the initial stage of sintering. The mechanical properties of W were improved with sintering enhancement, and the relationship between mechanical response and sintered density was found to be not obviously dependent on the type or content of sintering additives used. The mechanical properties of the partially-sintered W compacts were critically controlled by interparticle neck size – a sintering property whose value can be estimated from the densification parameter. Specifically, hardness of partially-sintered materials is explicitly related to both sintered density and densification, in accordance with Arato et al.'s hardness model. On the other hand, fracture toughness scales with densification but apparently not with sintered density, an affect captured by Green and Hardy's fracture toughness model for partially-sintered materials.

3.4 Concluding Remarks

In this chapter, the production of partially-sintered W at low firing temperatures has been found feasible using the activated sintering technique. With minority contents of sintering activators, namely Ni and Fe, sintering kinetics, sintering properties and corresponding mechanical properties of W could be improved at the low temperature (~1177°C) of interest to this work. These properties could be controlled with the types and contents of additives used. The knowledge gained here will aid in designing and fabricating low-temperature co-fired W/Al_2O_3 composites with a W layer of sufficient strength to resist spallation of W particles *from the W layer*, which may occur due to poor sintering. In the following chapter, which is concerned with joining of co-fired W and Al_2O_3, it will be shown that sintering activators not only affect the mechanical properties of the W sintered layer, but also influence the adhesion of bonded materials in various ways. The effects of sintering additives for Al_2O_3 on joining properties will be examined in chapter V.

Table 3.1: The characteristics of W powders in series A and B.

Property	A	B
Mean Size [μm]	1.2	1.7
Tap Density [%TD]	42	60
Compact Density [%TD]	50	64
Ni Impurity [wt.%]	< 0.0005	0.006
Fe Impurity [wt.%]	< 0.001	0.018

Table 3.2: The sintering exponent (m) and apparent activation energy for sintering (Q) of various sets of W specimens prepared with series A powder.

Material	m	Q [kJ/mol]
Pure W	0.4	404
W+0.6 monolayer Ni	0.65	406
W+1.3 monolayer Ni	0.66	315

Table 3.3: Proposed relationships between the relative interparticle neck radius and densities.

Fischmeister and Arzt [67, 68]	**Skorokhod** (initial stage) [70]	**Skorokhod** (all stages) [70]	**Helle et al.** [71]
$\left(\frac{r}{R}\right)^2 = 1.75(\rho_s - \rho_g)\cdot(1-(\rho_s - \rho_g))$	$\left(\frac{r}{R}\right)^2 = \frac{4}{3}\ln\left(\frac{1-\rho_g}{1-\rho_s}\right)$	$\left(\frac{r}{R}\right)^2 = 1-\left(\frac{1-\rho_s}{1-\rho_g}\right)^{4/3}$	$\left(\frac{r}{R}\right)^2 = \frac{1}{3}\left(1-\left(\frac{1-\rho_s}{1-\rho_g}\right)\right)$

Table 3.4: Proposed relationships between coordination number of sintered particles and relative density.

Fischmeister and Arzt [67, 68]	**German**[25]	**German** [72]
$z = 7.3 + 8.07(\rho_s - 0.64)$	$z = 7 + 17.5(\rho_s - 0.64)$	$z = 14 - 10.3(1-\rho_s)^{0.38}$

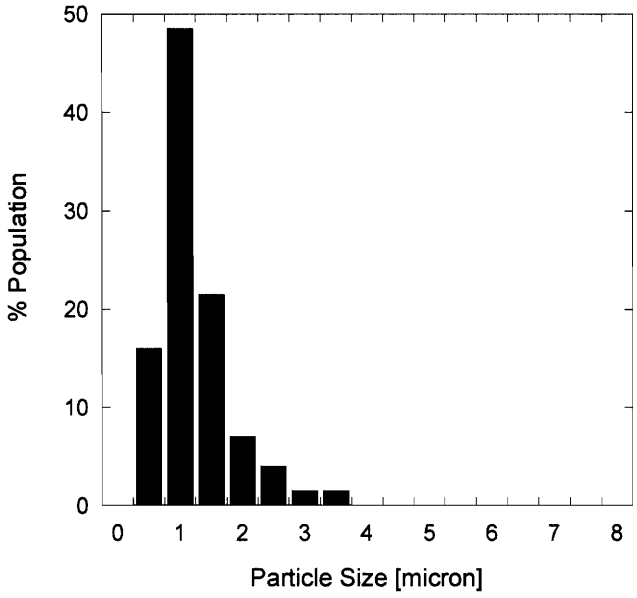

(a)

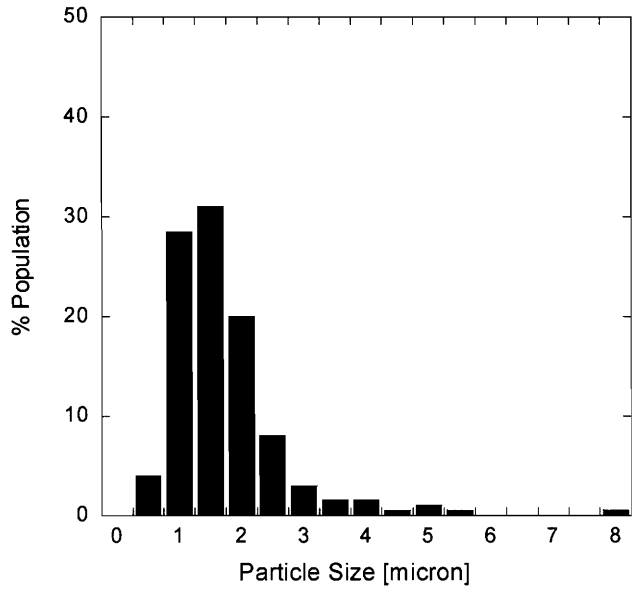

(b)

Fig. 3.1a-b: Particle size distribution of (a) 'series A' and (b) 'series B' tungsten powders.

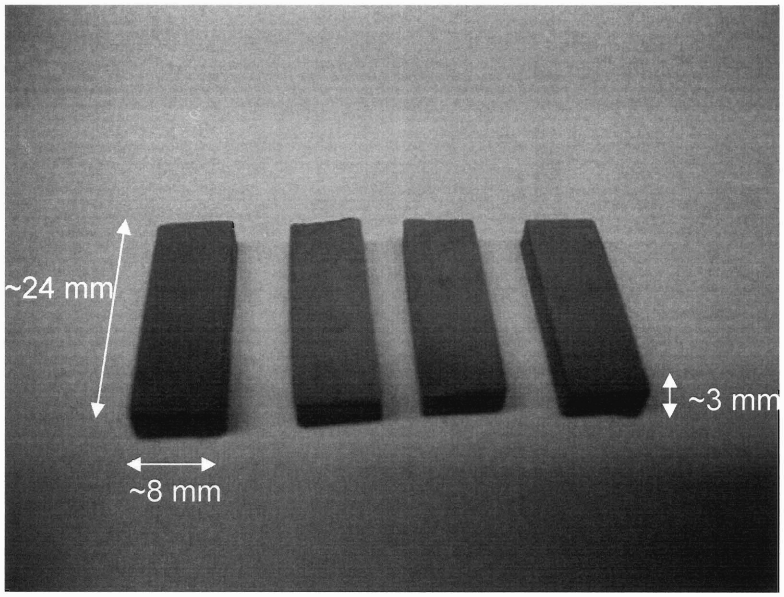

Fig. 3.2: Typical W compact specimens containing different amounts of sintering activators. The specimens shown in this figure were all prepared from series A tungsten powder. The leftmost specimen contained no additive, while others contained Ni and/or Fe.

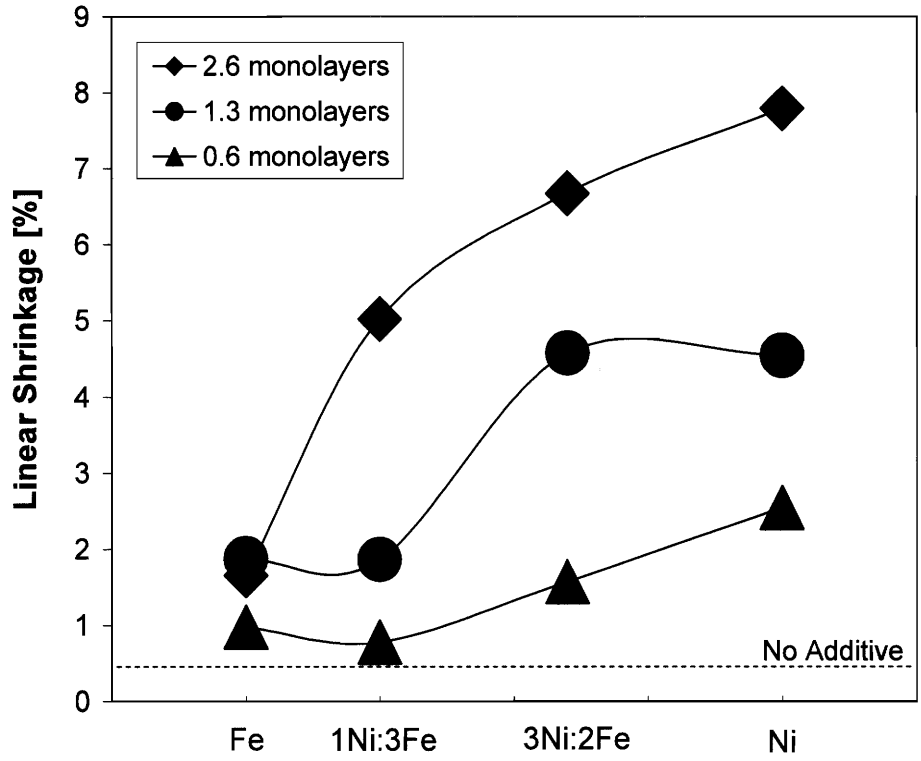

Fig. 3.3: Linear shrinkage of the W compact specimens activated by Ni and Fe at various concentrations. The specimens were sintered at 1177° C for 1 hour.

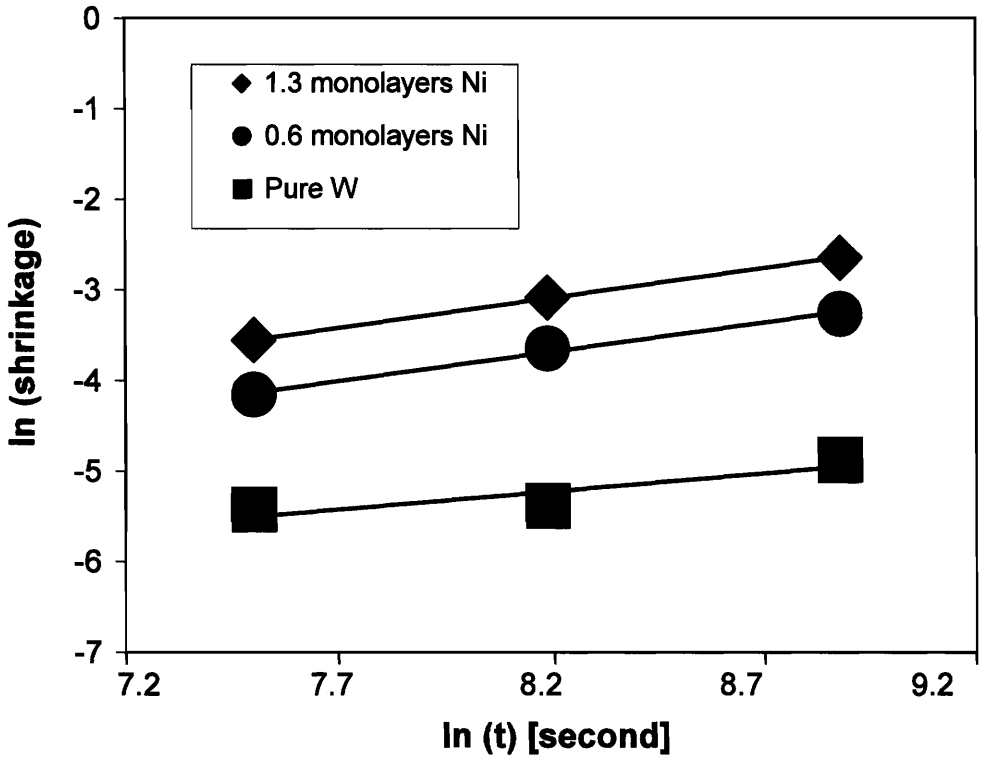

Fig. 3.4: Linear shrinkage of Ni-activated W compact specimens sintered at 1177° C for 0.5, 1, and 2 hours.

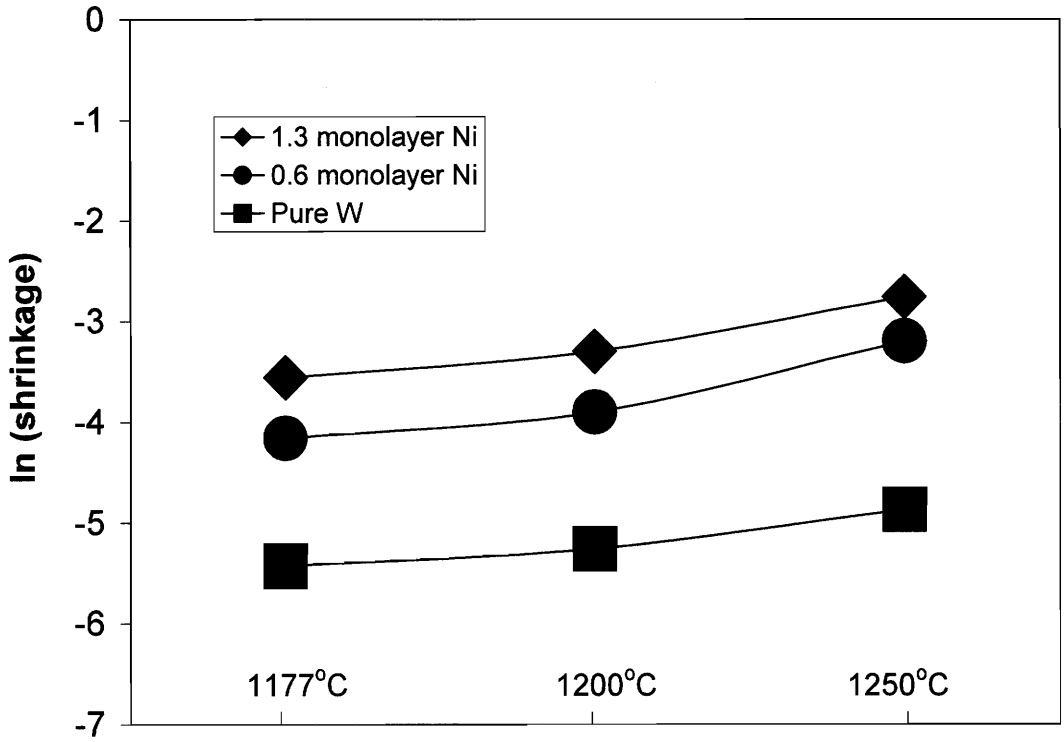

Fig. 3.5: Linear shrinkage of Ni-activated W compact specimens isothermally sintered at various temperatures for 0.5 hours.

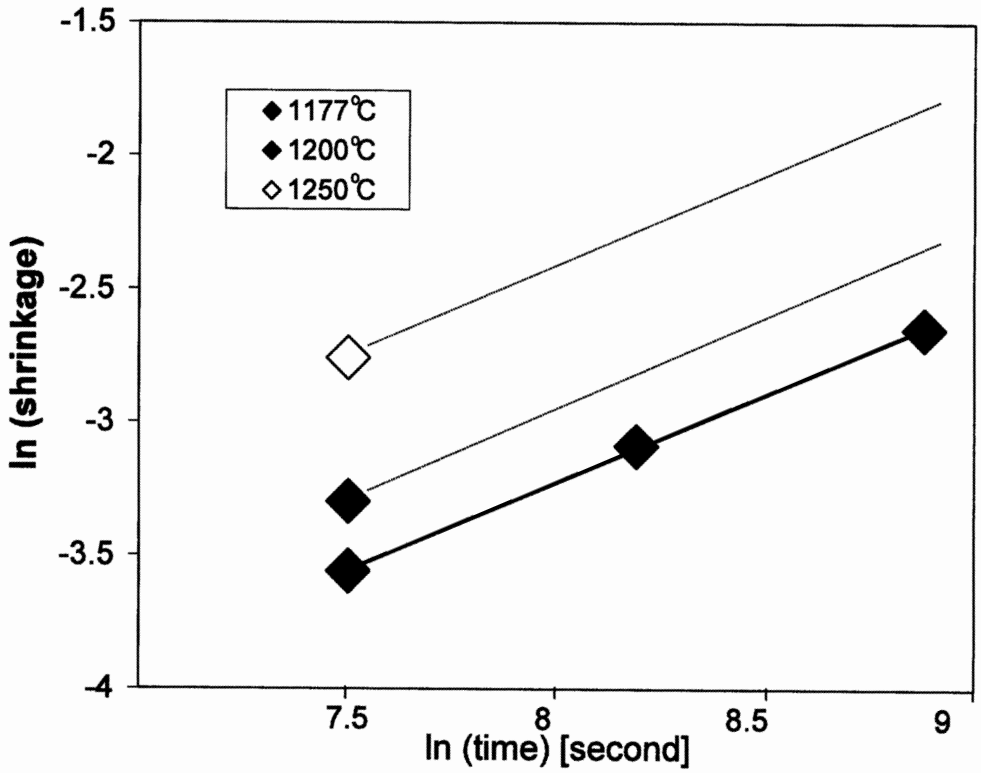

Fig. 3.6: Linear shrinkage of W specimens which contained 1.3 monolayer Ni and were isothermally sintered at various times and temperatures.

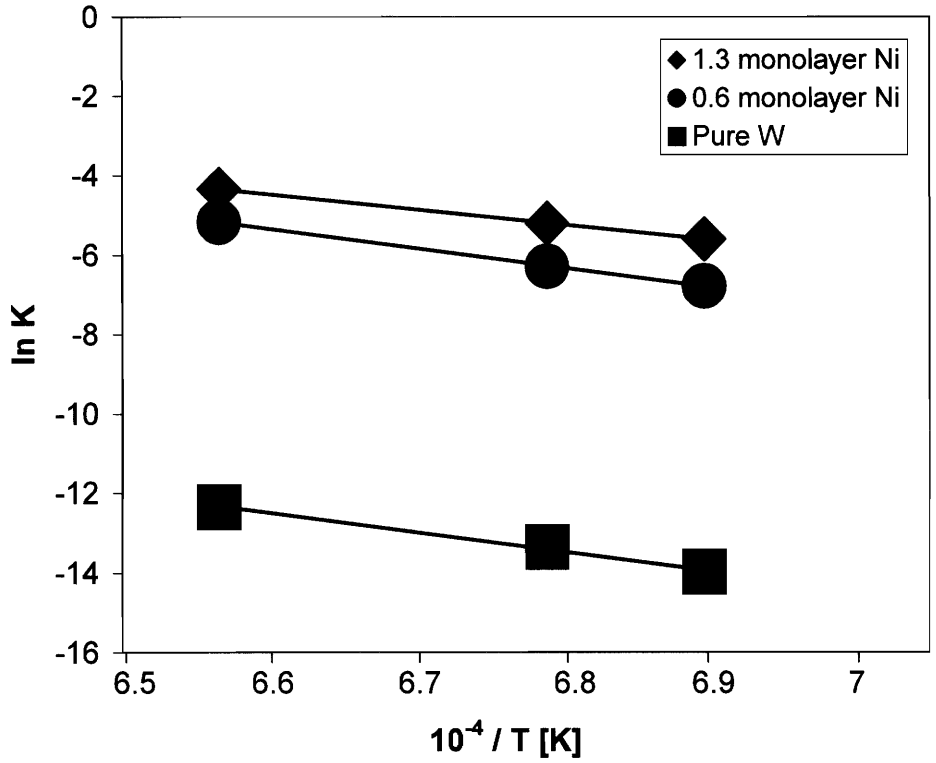

Fig. 3.7: Plot of ln K vs. 1/T for various sets of W specimens prepared from series A powder.

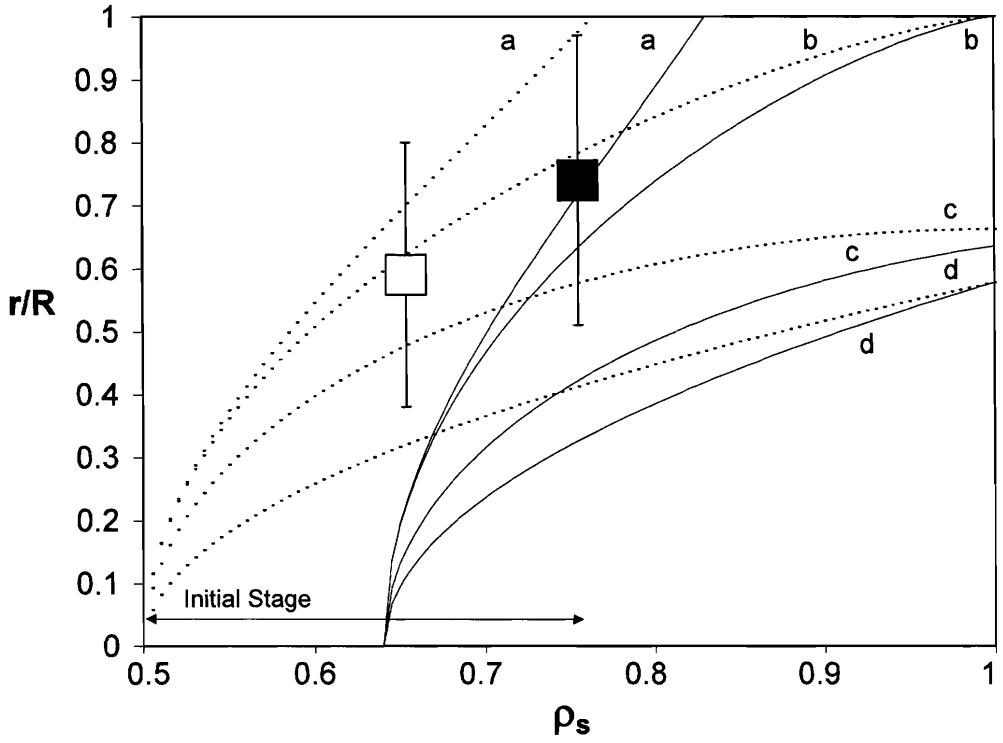

Fig. 3.8: The relative neck radius of powders with green density, ρ_g of 0.5 (·····) and 0.64 (——) as a function of sintered density, ρ_s, according to the models of (a) Skorokhod (initial stage) [70], (b) Skorokhod (all stages) [70], (c) Fischmeister and Arzt [67, 68], and Helle et al. [71] (See Table 3.3). Also shown on the plot are the average values of relative neck radius of (i) series A sintered powders with $\rho_g = 0.5$ and $\rho_s = 0.65$ (□), and (ii) series B sintered powders with $\rho_g = 0.64$ and $\rho_s = 0.76$ (■).

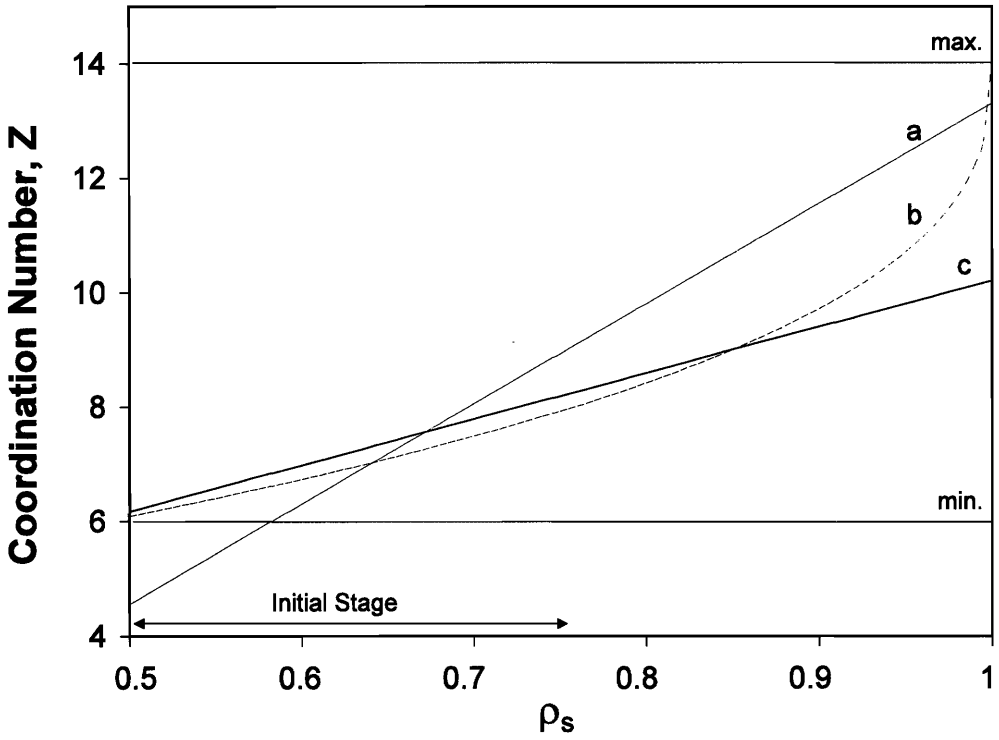

Fig. 3.9: The coordination number of powders as a function of sintered density, ρ_s, according to two models of German, (a) [25] and (b) [72], and (c) Fischmeister and Arzt's [67, 68] model (See Table 3.4). The highest and lowest values of the coordination number possible are 6 and 14, respectively, as shown on the plot.

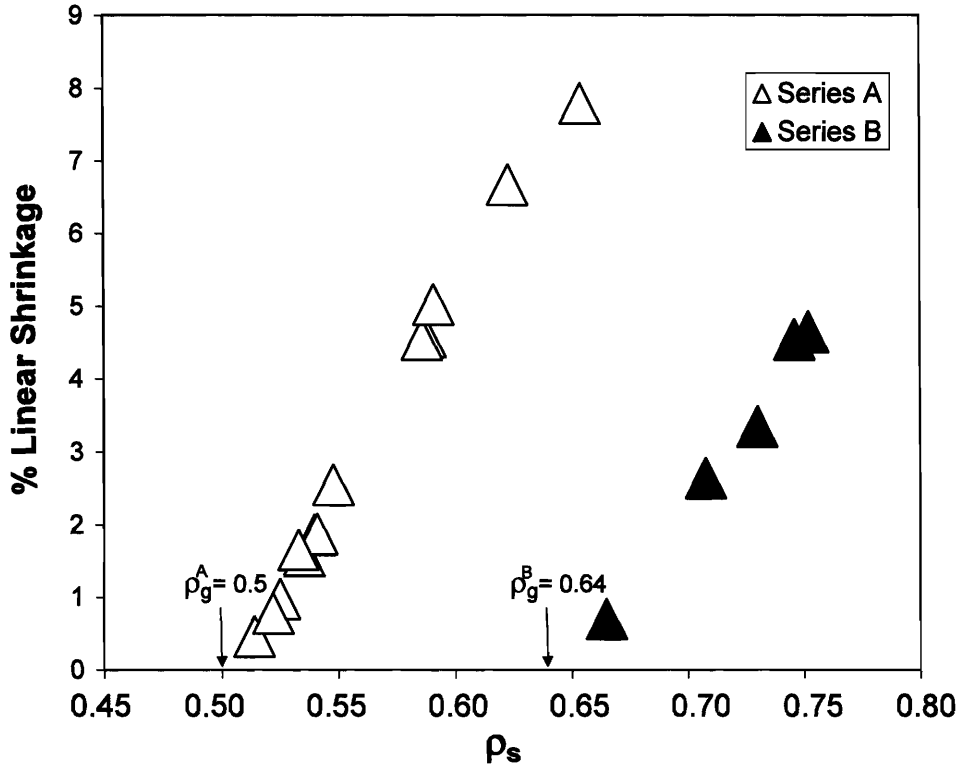

Fig. 3.10: The percent linear shrinkage of W compacts prepared with series A and series B powders containing various contents of sintering additives. The shrinkage is presented as a function of sintered density.

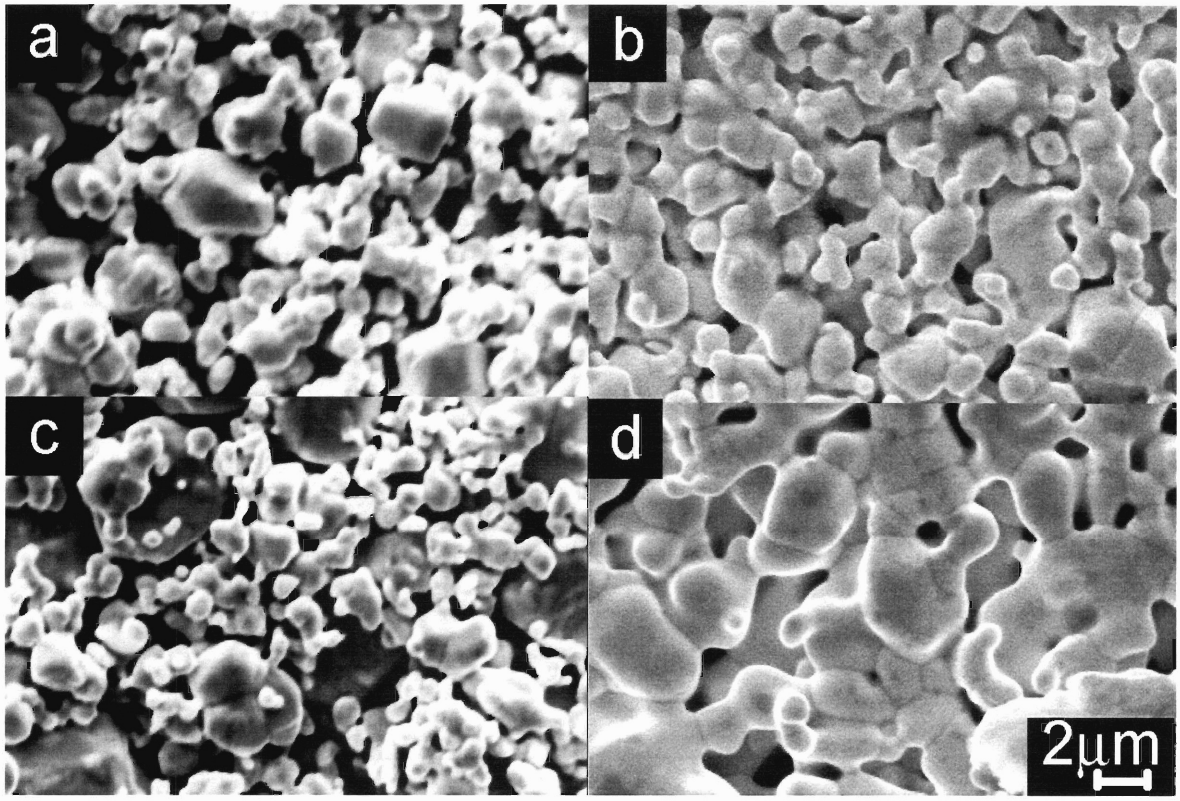

Figs 3.11a-d: SEM micrographs of W compacts prepared with (a) series A powder (ρ_s=0.51), (b) series A powder containing 0.18wt.% Ni (ρ_s=0.65), (c) series B powder (ρ_s=0.67) , and (d) series B powder containing 0.10wt.%Ni and 0.02wt.%Fe (ρ_s=0.75). The specimens shown in (b) and (d) contained the highest amounts of additives used to prepare series A and series B specimens, respectively.

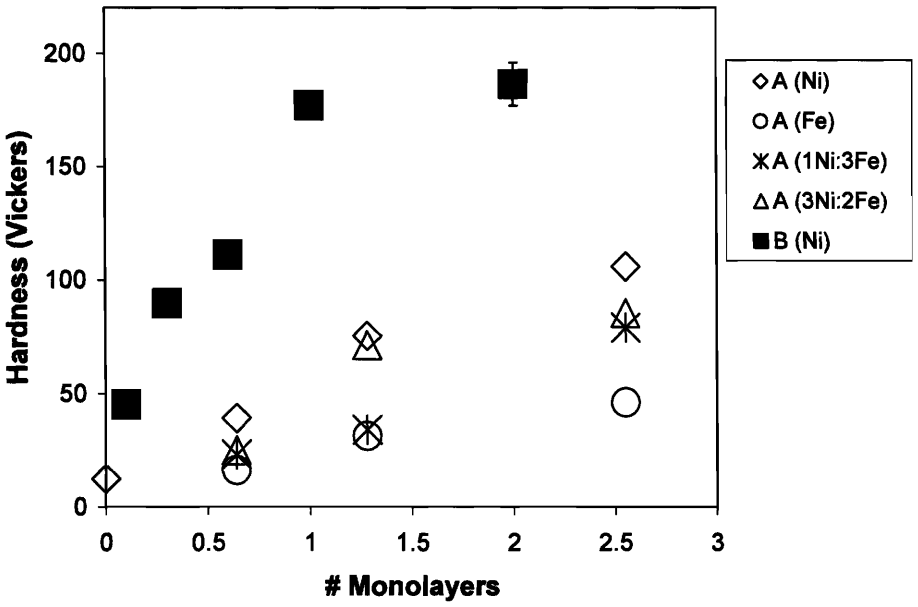

(a)

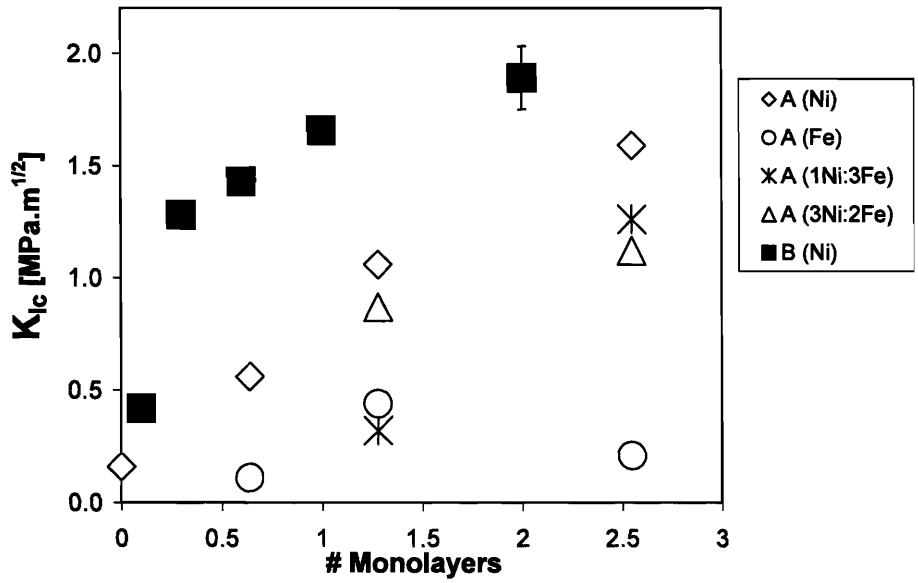

(b)

Figs. 3.12a-b: The average (a) Vickers hardness and (b) fracture toughness of W compacts prepared with series A and B powders that contained various types and contents of sintering additives. The content of sintering activators is presented in terms of monolayer coverage of activators on the surface of W particles. A representative error bar is presented for one of the data sets on each curve to show the degree of deviation in the data obtained.

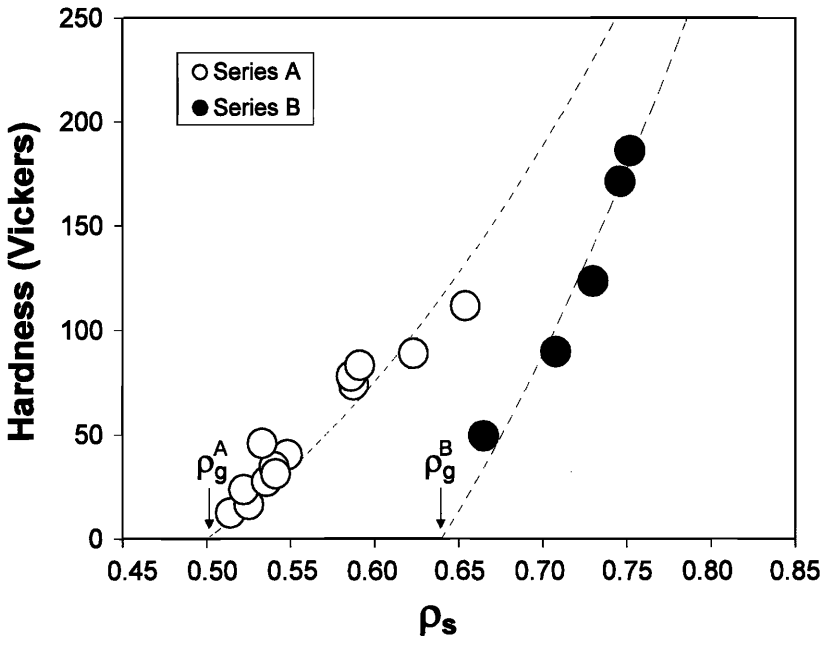

(a)

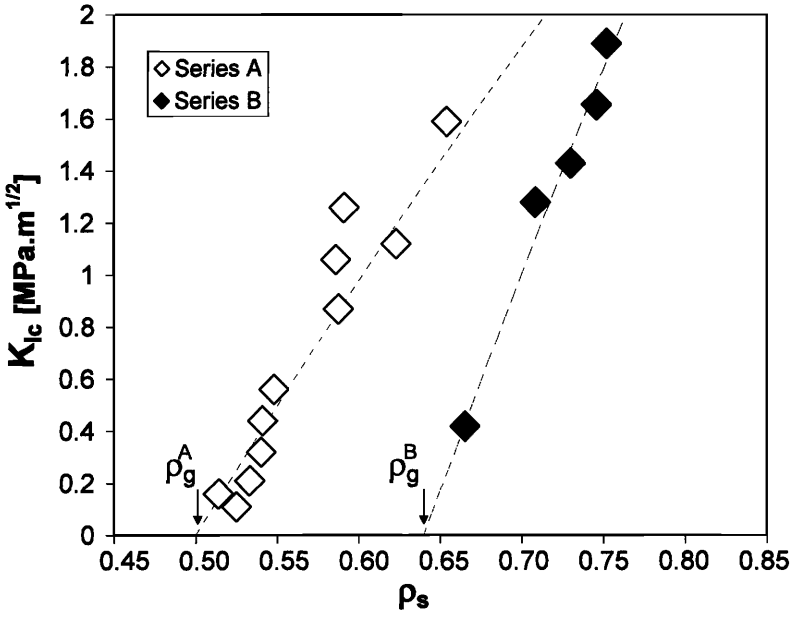

(b)

Figs. 3.13a-b: The average (a) Vickers hardness and (b) fracture toughness of W compacts prepared with series A and B powders, as a function of sintered density. Trendlines are shown for visualization purposes only.

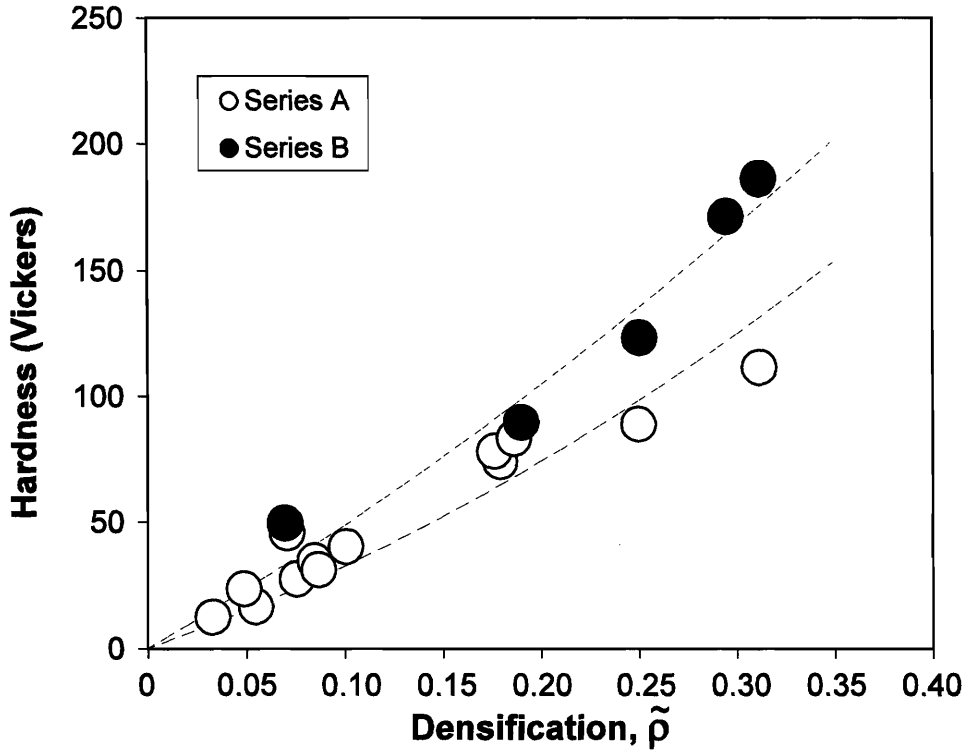

Fig. 3.14: Vickers hardness of W compacts in series A and B as a function of densification. Trendlines are prescribed for visualization purposes.

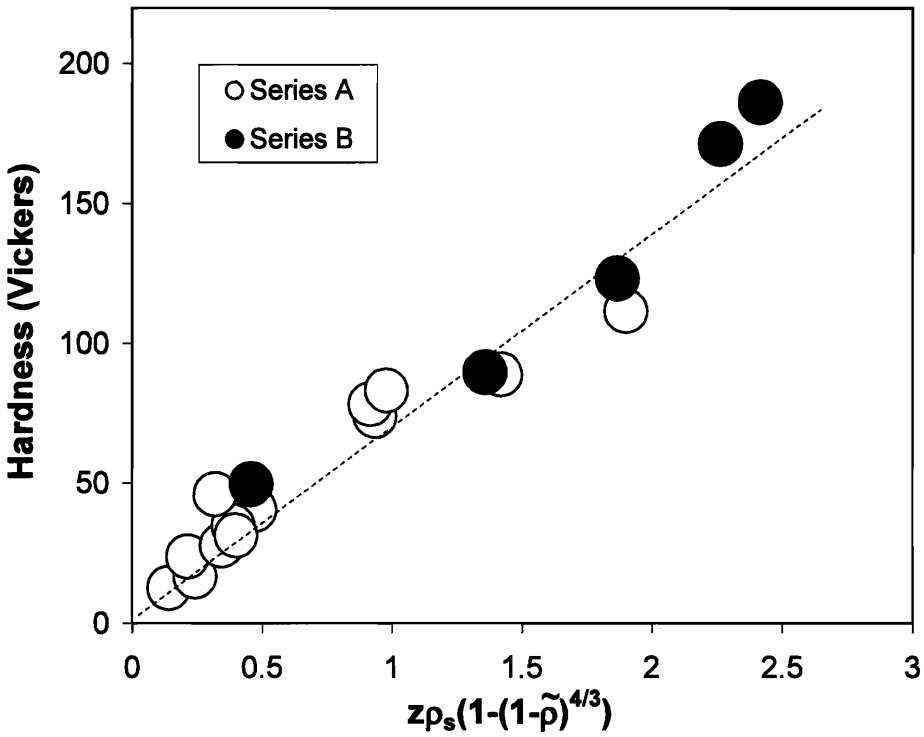

Fig. 3.15: Vickers hardness of W compacts in series A and B as a function of a factor which contains the coordination number (z), the sintered density (ρ_s), and densification ($\tilde{\rho}$). A trendline is prescribed for visualization purposes.

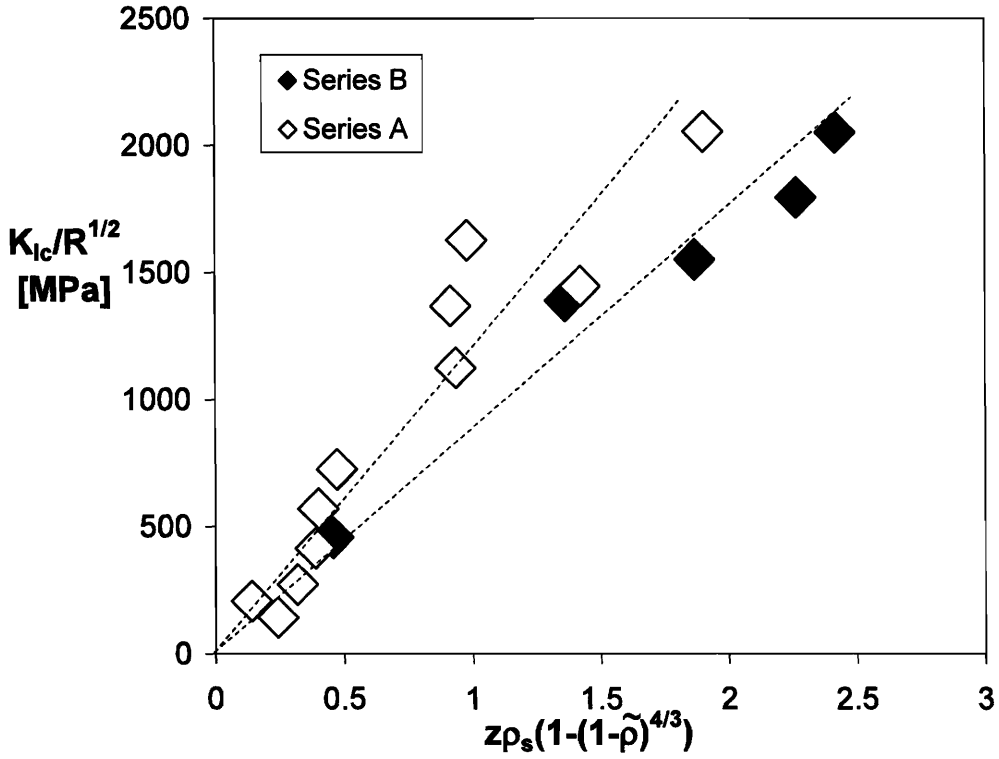

Fig. 3.16: Normalized fracture toughness of W compacts in series A and B as a function of a factor which contains the coordination number (z), the sintered density (ρ_s), and densification ($\tilde{\rho}$). Trendlines are prescribed for visualization purposes.

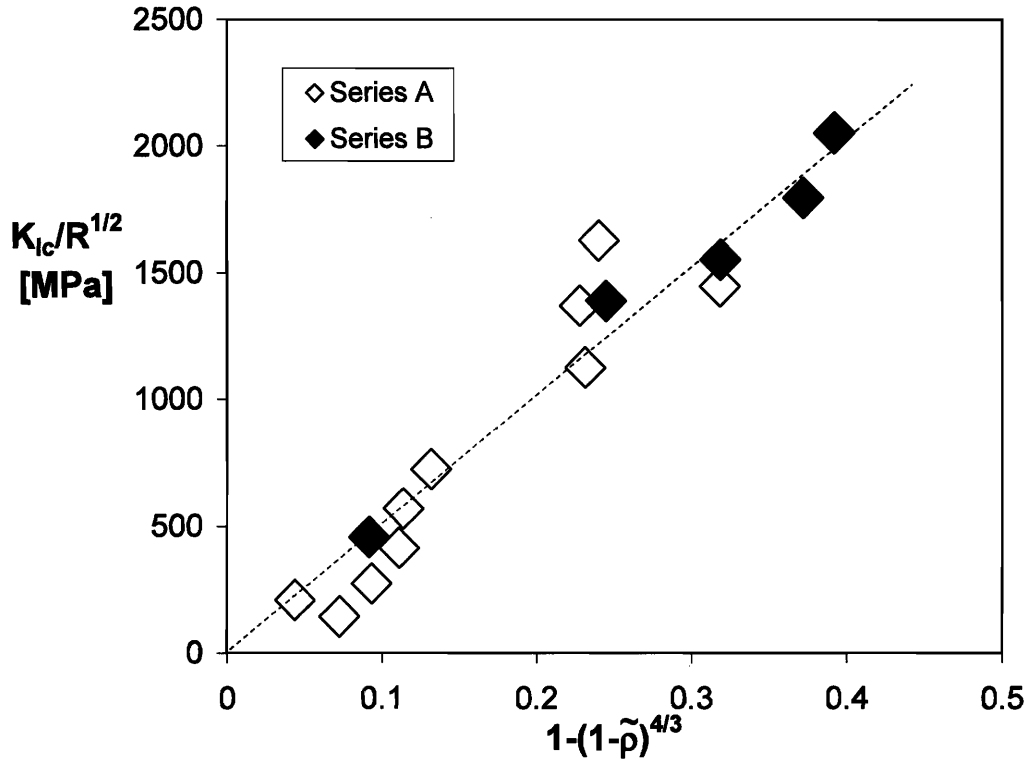

Fig. 3.17: Normalized fracture toughness of W compacts in series A and B as a function of a factor which solely depends on densification ($\tilde{\rho}$). A trendline is prescribed for visualization purposes.

Part B: JOINING OF W AND Al_2O_3

Chapter IV. Co-firing of W and Al_2O_3

4.1 Introduction

Because of differences in the characteristics of ceramics and metals, joining of these two classes of materials is beneficial and essential in many applications. Depending on the specific metal and ceramic to be joined, techniques such as glazing, diffusion bonding, hot-press bonding, and brazing by way of metallization are all plausible [76]. Joining of W and Al_2O_3, in particular, has been a subject of interest since the 1930s. Due to their unique and distinct properties, W and Al_2O_3 have been employed in the form of co-fired composites in a number of applications, including electronic packaging, vacuum devices, and reaction barriers. Electronic packages, for example, require circuits with good electrical conductivity, and substrates with superior mechanical and dielectric properties – these characteristics can be found in W and Al_2O_3, respectively.

Growing numbers of research papers in the field of W-Al_2O_3 joining over the past few decades are associated with joining techniques employed at high processing temperatures (above 1500°C) in which a thin layer of W and an Al_2O_3 substrate are bonded together by interaction with a glass phase [77-80]. This type of joining involves the use of chemical additives that induce glass migration in the system and is employed primarily in two applications – metallization for brazing and metallization in electronic packaging (These subjects will be discussed in more detail in Ch. VI). For certain applications, however, it may be more desirable to fabricate W/Al_2O_3 co-sintered components at relatively low temperatures (<1200°C). Among the potential benefits of low temperature processing include reduction in energy cost, increase in productivity, and that a partially-sintered structure can be obtained. Compared to high temperature joining, the study of joining of W and Al_2O_3 at low firing temperatures (<1200°C) is very limited.

In this chapter, our main focus is the factors that affect adhesion of low-temperature co-sintered W/Al_2O_3 compacts, which contain no chemical additives that would induce glass migration along the joined interface. While the current study will focus on layered composites

formed through a dry powder route, the result obtained in this chapter serves as a baseline for W/Al_2O_3 layered composites processed by different strategies which will be examined later. Additionally, the understanding developed here will also elucidate principles relevant to other joining processes where mechanical interlocking takes place at the metal/ceramic interface. Background on the joining of pure W and pure Al_2O_3 is provided in the subsequent section. Several joining strategies which involve the use of chemical additives and migrating phases will be investigated in Ch. VI.

4.2 Joining of W and Al_2O_3 without third-phase migration

W and Al_2O_3 can be joined by a co-sintering process, whereby the two materials in the form of powder are layered on one another and sintered. Chemical additives such as Mn or combinations of SiO_2, CaO, etc. may be incorporated into a W/Al_2O_3 joining system to induce the formation and migration of liquid phase along the joining interface. It should be mentioned, however, that for certain applications, W and Al_2O_3 without chemical additives are more favorable. For example, the presence of diffusion layers caused by Mn is undesirable in electron tubes for UHF applications [81]. When additives are not used, thermal conductivity, dimensionality and microstructure of W/Al_2O_3 multichip modules can be better controlled [82]. Additionally, uncontrollable leaching of oxidizable metal additives or glassy phases from one layer to another may also affect the performance of a component.

Without the presence of chemical additives and hence a third phase along the joining interface, it has been found that adhesion of co-sintered materials is relatively weak. This point is well-illustrated by Cole and Sommer's [83] comparison study on the influence of joining process details on adhesion of Al_2O_3 and Mo, a material whose characteristics are similar to W. Their results, summarized in Table 4.1, show that tensile strength of the joint prepared without additives at 1500 °C was on the order of 1 MPa. While it was observed that adhesion increased with firing temperatures, it was still well below that of specimens containing additives.

The mechanism that controls adhesion of the bonded materials could be a chemical interaction (primary and/or secondary), a mechanical interaction, or a combination of both. For W and Al_2O_3, it has been found that no primary chemical interaction nor inter-diffusion of the two species occur when they are in contact and processed through solid-phase sintering [81, 84-86]. Consequently, it has been suggested that the bonding of co-sintered W and Al_2O_3 is primarily controlled by mechanical interlocking of sintered particles along the joined interface.

In 1970, Chance [84] published his frequently cited work on co-sintering of pure W and pure Al_2O_3. Chance examined the processing conditions by which thin Al_2O_3 substrates and metallizing layers of W could be produced via mechanical interaction of sintered particles, with minimal shape distortion of the component. To produce test specimens, pastes of W were screened onto layers of green ceramics and the materials were co-sintered for 3 hrs. at 1570°C +/- 20°C in a wet H_2 atmosphere (22°C dew point). With excessive use of small-sized W particles, the author found that a high degree of densification, grain growth and reorientation of

W particles occurred, and might lead to the weakening of particle interlocking at the interface. By controlling the particle size distribution of W powders and the use of terepthalic acid to help in shrinkage matching, delamination-free W/Al_2O_3 composites with minimal shape distortion could be produced without the use of chemical additives that induce the formation of a third phase. A more recent study on joining of W and Al_2O_3 without glass migration was reported by Foster et al. [82]. In their investigation, the authors applied thin films of W on 99.6% Al_2O_3 substrate by a photolithography method. Al_2O_3 and TiO_2 had been added to W for thermal expansion matching with the Al_2O_3 body. Similar to Chance's results, successful bonding of the materials was obtained when the specimens were fired at temperatures near 1500°C.

While there is no work reported in this area for low-temperature processing (<1200 °C), these past studies indicate that, through appropriate control of processing parameters, bonding of W and Al_2O_3 without a migrating phase is feasible when the materials are processed at high temperatures close to 1500°C. It can be expected that to achieve strong adhesion of co-sintered bilayers of this type, several factors need to be controlled – these may include the degree of mechanical interlocking, residual stress evolution during processing, and the sintered properties of individual layers. In the next section, the manner in which these different factors may contribute to adhesion of co-sintered bilayers will be examined. The investigation will be performed on W/Al_2O_3 compacts processed at low firing temperatures. The process of activated sintering, with minimal additive content (as proven applicable to low-temperature sintering of W in the previous chapter), will be used to control the W layer properties. The influence of sintering activators on adhesion and the characteristics of the bonding of low-temperature co-fired W/Al_2O_3 will be discussed.

4.3 Contributions to Interfacial Adhesion in Co-Sintered Bilayers

4.3.1 Introduction

W/Al_2O_3 bi-layered composites represent a material system that is produced through co-sintering, which involves simultaneous joining and consolidation of powders. Other examples of material systems produced by co-sintering are solid oxide fuel cells which are composed of electrolytes and anode substrates [47, 49], multi layer capacitor produced by co-firing of $MgTiO_3$ and Cu electrodes [87], and zirconium silicate-aluminium silicate ceramic molds used in investment casting [45, 46]. The advantages of co-sintering include potential net-shape processing of complex geometries, the incorporation of refractory materials at relatively low processing temperatures, and its amenability to slurry-based processing routes (see Ch. V). While the performance-critical physical properties of co-sintered systems vary from one application to another, the adhesion between bonded layers is important for most layered composite systems, as it underpins the structural integrity of components.

The main factors controlling adhesion of co-sintered materials include (i) the nature of bonding along the joined interfaces, (ii) residual stresses arising in the firing cycle and (iii) the degree of sintering and associated density-related mechanical properties of the individual layers of the composite. For co-sintering of non-reactive species, such as W and Al_2O_3, mechanical interlocking of sintered particles is often the key mechanism controlling point (i), while shrinkage mismatch (during sintering) and thermal expansion mismatch (during cooling) influence point (ii). It is also clear that there may be significant interrelations between these issues and point (iii); whereas longer sintering times may lead to stronger layers and stronger mechanical interlocking at the interface, it may also influence the development of shrinkage mismatch of the components, which can result in the formation of interfacial micro-cracks that compromise the strength of the joint [88]. Despite this synergy, points (i), (ii), and (iii) are usually treated separately in the literature. References [77, 82, 84, 89, 90], for example, are studies related to joining techniques for co-fired W/Al_2O_3, focusing on the nature of bonding without significant attention to residual stresses. References [91-95], on the other hand, involve studies of shrinkage and thermal mismatch induced in co-sintered materials, but do not concern themselves with the density-related property changes of the individual sintered layers.

It is the purpose of this work to explicitly study the effects of the above points simultaneously, and to gain some understanding of their interaction as it impacts the toughness

of joints between co-sintered layers. In particular, the influences of the sintering variables and residual stresses on interfacial interlocking and the adhesion of co-sintered bilayer materials are investigated experimentally in the W/Al_2O_3 system, which is processed at low firing temperature via activated sintering. Finite element simulations are employed to numerically study the interfacial fracture mechanics of the system.

4.3.2 Experimental Procedure

A. Material System

The material system chosen for the present work was W/Al_2O_3 with a minority content of sintering activators, namely Ni and Fe, in W, which were used to control the sintered strength and stiffness as well as the shrinkage mismatch of co-sintered W/Al_2O_3. As discussed earlier, no liquid phase will be induced in this type of system, and mechanical interlocking of sintered particles is the main mechanism that controls adhesion.

A single lot of Al_2O_3 powder from Remet Corp. (Utica, NY) with a mean particle size of 4 μm (equivalent diameter) was used to prepare all specimens in this work. The W powders, on the other hand, were received from various suppliers and will be labeled with the letters C through E. Fig. 4.1 presents the particle size distributions of the W powders, which were measured on a population basis using a scanning electron microscope (SEM) to examine at least 300 randomly-selected individual particles. The mean particle size and the content of Ni and Fe of each powder are collected in Table 4.2, and are different due to the origin of the powders as well as the procedures we have employed:

- Powder "C" was supplied by Alfa Aesar (Wardhill, MA), and had a relatively low impurity content. In order to manipulate the sintered density of this powder, various minority additions of Ni powder (2.2-3 μm) were added to the W powder by dry mixing as discussed in Ch. III; these powders will be labeled with an additional number (e.g. C-1, C-2), which differentiates between different Ni additions (see Table 4.2).
- Powder "D" was supplied by Alldyne Powder Technologies (Huntsville, Alabama). This powder differed from powder "C" primarily in its relatively high initial content of sintering activators (Ni and Fe) present as impurities. The mean particle sizes of powder C and D were comparable (Table 4.2), although the two powders had distinct

particle size distributions (Figs. 4.1a and 4.1b) with powder D having a more significant population of particles with size between 1-2 μm. Similar to the procedure used with powder C, powder D was mixed with various additions of Ni, and the resulting mixtures will be labeled D-2 to D-4 (Table 4.2).

- Powders E-1, E-2, and E-3 were also supplied by Alldyne Powder Technologies (Huntsville, Alabama), and were chosen to more closely represent the kind of variability in powder character that might arise in an industrial setting. For example, impurities of both Ni and Fe were present as tramp elements in theses powders, and were somewhat different in samples E-1, 2, and 3. No additional Ni was mixed into the powders of this series, and the mean particle sizes and particle size distributions of the powders were all reasonably comparable to one another (Figs. 4.1c, d, e).

The concentration of sintering activators will be reported in terms of the average monolayer coverage of the additives, relative to the amount of W surface area in the system (M). The calculation procedure has been discussed in Ch. III.

B. Processing

A two-layer compact joining specimen was the test geometry chosen for this work, for reasons that will become clear in the next section. To prepare such specimens, Al_2O_3 and W powder were sequentially loaded into a die of rectangular cross-section and cold pressed without binders using a single-action press at 80 MPa. These green specimens were then co-fired in a furnace programmed with a heating rate of 5° C/min and an isothermal hold at 1177° C for one hour, followed by slow furnace cooling. This cycle allows only modest sintering for both W and Al_2O_3, so the specimens tested in this work experienced only "initial stage" sintering and had relative densities below about 0.75 after processing. To prevent the oxidation of W, the processing was carried out in a dry 3% H_2-97% N_2 atmosphere. The geometry of each fired specimen was approximately 8.3 x 24.7 x 5.1 mm, with individual layer thicknesses for W and Al_2O_3 being 4.4 mm and 0.7 mm, respectively. These specimens differed from one another only in the character of the W powders according to Table 4.2.

Some typical test specimens are shown in Fig. 4.2a. In Fig. 4.2b, a magnified view of the interfacial region between W and Al_2O_3 is shown in a SEM micrograph. The interfacial character is similar to that seen in prior work on co-sintered W/Al_2O_3 [84], and contains no

obvious excess porosity as compared with that in the individual layers themselves. As expected, there is no sign of chemical reaction between the layers.

C. Mechanical Testing

To establish a baseline for understanding the properties of W/Al_2O_3 bilayers, mechanical tests were first performed on some free-standing W or Al_2O_3 specimens, produced using the same general procedures described above. Flexural elastic modulus of W and Al_2O_3 was assessed using standard three-point bending tests according to ASTM D790-03.

The adhesion of W/Al_2O_3 co-sintered specimens was evaluated using a four-point bending delamination test [96] with the geometry shown in the inset to Fig. 4.3. This test has been used in a number of investigations to determine the bonding properties of interfaces [97-100] and was selected here because it allowed us to evaluate the interfacial fracture energy [101]. The tests were performed using a universal testing machine with a crosshead speed of 50 μm/min. Prior to the test, each specimen was pre-notched in the middle of the sample (on the plane of symmetry) in the porous Al_2O_3 layer, using a razor blade.

4.3.3 Experimental Results and Discussion

Table 4.3 presents the measured linear sintering shrinkage and Young's modulus of free-standing Al_2O_3 and W specimens made with series E powders. The results clearly show that the degree of sintering, quantified here by the sintering shrinkage, improved with the increase of sintering activator concentration in the W powders. Elastic modulus is well-known to increase with sintered density, and modulus differences for the different W powders in Table 4.3 may be attributed to the enhancement in sintering. The Al_2O_3 compact, on the other hand, sintered only weakly and had a very low degree of shrinkage (~0.1%) at our chosen sintering condition. The large average particle size (4 μm), low firing temperature, and high purity (i.e., lack of sintering additives like SiO_2) all contributed to the low degree of sintering of Al_2O_3. As a consequence, the fired Al_2O_3 body was sound and could be handled without fragmenting, but the measured Young's modulus was extremely low.

For the co-sintered W/Al_2O_3 bilayer specimens, after the sintering cycle, most specimens were intact and no macroscopic interfacial cracks were present. The only exceptions to this observation were specimens from groups C-1 and C-5, which spontaneously delaminated during

the firing cycle. For some groups of specimens, the W layer exhibited a relatively high degree of shrinkage as compared to the Al_2O_3 layer, leading to the development of slight curvature in the specimens, as depicted in Fig. 4.2a.

Fig. 4.3 illustrates some representative force-displacement curves obtained from the four-point bending delamination tests performed on the co-sintered W/Al_2O_3 specimens. Three typical stages can be identified over the duration of the test – initial elastic deflection, interfacial crack initiation and propagation, followed by elastic loading and through-crack failure of the W layer – as depicted by the symbols in the figure. The crack propagation stage was manifested in these tests with both a load drop and a displacement excursion, owing to the use of displacement control. Figures 4.4a and 4.4b respectively show representative specimens before and after mechanical testing. A separation of the joined materials by an interfacial crack could be observed. From one test to another, either symmetrical or asymmetrical interfacial cracking could be observed; in the latter case, the average of the crack propagation forces for the left and right cracks is reported. In every case, the excursion in the load-displacement curve was correlated with direct observation of an interfacial crack. It is also important to note that the W layer in every case failed without sustaining any plastic deformation. This is consistent with the relatively high ductile-to-brittle transition temperature of W [75] and the relatively low density of the partially sintered layer.

The test data in Fig. 4.3 yields two critical loads of interest: the load at interfacial crack initiation (•), and that at through-crack failure of the W layer (♦). The first of these critical loads will be termed the *adhesive load*, P_a, and will be only briefly presented and discussed in this section. The raw values of P_a are useful because they allow direct comparison of the apparent interfacial strength amongst the various specimens, whose geometry was identical. Later in this chapter, the values of P_a will be used in a more quantitative analysis to determine the critical energy release rate for interfacial fracture.

The second critical load, that corresponding to through-crack failure, is denoted P_f, and can be used to determine the *fracture strength* of the W layer. This is because, after the arrest of interfacial cracks in the W/Al_2O_3 specimens, the W layer experiences a uniform bending moment between the two inner pins, with a maximum tensile stress, σ_f, across the top surface [102]. The tensile stress in this region is responsible for final rupture in the W layer, and because there was no significant plastic deformation before rupture, the fracture strength can be determined from:

$$\sigma_f = \frac{6P_f L}{bh_w^2} \qquad (4.1)$$

where L (3.8 mm) is the horizontal distance between the inner and outer loading pins; b (8.3 mm) is the width of the specimen; and h_w (4.4 mm) is the thickness of the W layer.

The measured values of fracture strength and adhesive load for the various bilayer materials are plotted as a function of the monolayer coverage of sintering activators in Figs. 4.5 and 4.6; each data point represents an average of three tests. Looking first at Fig. 4.5, we see that the fracture strength of the W layer increased considerably with the concentration of sintering activators present in the system. This strengthening is a direct result of the enhancement of sintering and thus densification of W, as observed earlier in the work discussed in Ch. III. In contrast to the monotonic strength trend in Fig. 4.5, the adhesion of the specimens, on the other hand, showed a more complex trend with activator concentration (Fig. 4.6), first increasing, then peaking and continuously decreasing. Note that in this plot, an adhesive load of zero indicates spontaneous delamination upon cooling after the firing cycle. Fig. 4.6 also shows that the different series of specimens (i.e., series C vs. D or E) exhibited generally different degrees of adhesion. The different absolute adhesive loads measured between series C, D, and E could be due to many different factors, and we will return briefly to this issue at the end of this chapter. The important point for the moment is that the same concave-downward trend with sintering activator concentration is observed in every case, and that improved sintering does not necessarily lead to improved adhesion if the activator content is too high (i.e., beyond the peak in Fig. 4.6). It is the purpose in what follows to understand the form of the trends in Fig. 4.6, in terms of the various contributions to adhesion.

4.3.4 Numerical Analysis

The adhesive loads measured in Fig. 4.6 can be influenced by several factors, which include:

- Interfacial toughness between W and Al_2O_3
- Elastic properties and the mismatch of these properties between the W and Al_2O_3 layer
- Specimen geometry

Each of these factors can be influenced by the degree of sintering in the W layer, and therefore by the sintering activator concentration used. It is unclear from the experimental results alone

which of the factors above controlled the observed trends in adhesive load. In order to decouple these effects, numerical modeling will be used in this section to extract the intrinsic interfacial toughness (i.e., the critical strain energy release rate for interfacial fracture) of bilayer W/Al_2O_3 specimens. Three groups of specimens, namely E-1, E-2, and E-3, were chosen for the numerical study, as these specimens showed the sharpest characteristic trend in Fig. 4.6.

The numerical analysis was performed on the commercial finite element package ABAQUS, assuming isotropic linear elasticity and plane strain conditions. The specimen geometry was assessed by careful dimensional measurements of the experimental specimens following the firing, to account for sintering-mismatch-related shape distortions. This geometry was then explicitly meshed as shown in Figs. 4.7(a)-4.7(c) for all three groups of specimens E-1, E-2, and E-3 used in the analysis; due to symmetry, only half of each specimen was modeled. It should be noted that while these models assume simple continua with a planar interface, the experimental materials actually contained some porosity in the joined bodies and across the joined interface. Therefore, the interfacial toughness values assessed in this study should be regarded as "apparent" toughness values, whose value is certainly lower than the interfacial toughness of identical materials without porosity.

The finite element model employed plane-strain eight-noded reduced integration isoparametric elements (CPE8R). A symmetry plane and a roller support were prescribed as boundary conditions as shown in Figs. 4.7(a)-4.7(c). The interfacial cracks were assigned a length of 0.5 mm; a representative crack tip region of the models is shown in Fig. 4.7(d). Several inputs were used in the analysis including Young's modulus, E, Poisson's ratio, ν, and the coefficients of thermal expansion (CTE) of the individual layers, as assembled in Table 4.4. The proper modulus values were obtained from the direct experimental measurements on monolithic W or Al_2O_3 materials (Table 4.3), while the Poisson's ratio and CTE of W and Al_2O_3 were assumed to be the same as those of fully dense materials [103-106]; unlike modulus, these two properties are not significantly affected by porosity [107, 108]. It should also be noted that the coefficient of thermal expansion of W is unaffected by minor Ni additions up to 0.4 wt. % [103].

Two kinds of loads were prescribed in these models, namely thermal load and applied bending load. To simulate thermal stresses evolved during the cooling step following firing, a thermal excursion from 1177°C to room temperature was applied to the simulated structures. The bending load was applied based upon the experimental four-point bending delamination

measurements by taking the load measured at crack propagation (P_p) for samples of series E, as given in Table 4.4. For this purpose the load was measured just after the crack initiation point in Fig. 4.3, at a point when the interfacial crack was about 0.5 mm in length; this corresponds to the geometry of the finite element model in Fig. 4.7.

For all of the numerical analyses, the thermal and bending loads were both applied in sequence, to best simulate the true conditions of the experiments. To study the effect of geometric sintering distortion on the driving force for crack propagation, specimen E-3 was also analyzed with constant input parameters, but with two different geometries: the highly distorted one shown in Fig. 4.7(c), and a perfectly orthogonal specimen without distortion.

For all of the simulations described above, the critical strain energy release rate, G_c, and phase angle, ψ, for interfacial cracking were determined. These are universal parameters that characterize interfacial toughness, and were determined using a standard crack surface displacement method [109, 110]. Specifically, the relative plane-strain displacements of two points on the top and bottom crack surfaces (Δu_x and Δu_y in the x- and y-directions, respectively) were determined, and subsequently used to derive the strain energy release rate and phase angle according to Eqs. 4.2 and 4.3 below:

$$G_c = \frac{\pi(1+4\varepsilon^2)\cdot(\Delta u_x^2 + \Delta u_y^2)}{8\lambda\cdot\left[\frac{(1-\upsilon_1)}{\mu_1}+\frac{(1-\upsilon_2)}{\mu_2}\right]} \tag{4.2}$$

$$\psi = \tan^{-1}\left(\frac{\Delta u_x}{\Delta u_y}\right) - \varepsilon\ln\left(\frac{\lambda}{h}\right) + \tan^{-1}(2\varepsilon) \tag{4.3}$$

In these equations, λ is the distance from the crack tip, and h is the total thickness of the specimen. The parameter ε is known as the bimaterial constant, and is given by:

$$\varepsilon = \frac{1}{2\pi}\ln\left[\left[\frac{(3-4\upsilon_1)}{\mu_1}+\frac{1}{\mu_2}\right]\cdot\left[\frac{(3-4\upsilon_2)}{\mu_2}+\frac{1}{\mu_1}\right]^{-1}\right], \tag{4.4}$$

and μ is the shear modulus:

$$\mu_i = \frac{E_i}{2(1+\upsilon_i)} \tag{4.5}$$

In the above equations, the subscripts (i=1 or 2) distinguish between Al_2O_3 (1) and W (2). The mechanics of interfacial fracture is discussed in more detail in Appendix A.

It should be noted that there is a closed-form analytical solution for the strain energy release rate of a bilayer composite tested in the four-point bending configuration, as derived by Charalambides et al. [96]. That solution has been widely employed to characterize interfacial toughness in various material systems [97-99], and extended to cover additional mechanical loads from thermal expansion stress [111]. However, the analytical solution is generally valid only when the interfacial crack size is relatively large ($a > 4h_{min}$, where h_{min} is the thinner of the two layer thicknesses) and a steady-state energy release rate condition is established. With a shorter interfacial crack, such as we consider here ($a \sim h_{min}$), calculations based on the analytical solution could be in error by as much as 20% as compared with a complete numerical solution [112], so the latter, more rigorous approach was employed here.

4.3.5 Simulation Results and Discussion

Table 4.4 shows the critical strain energy release rate and phase angle calculated from the finite-element analysis of bi-layer composites E-1, E-2, and E-3 with the geometries in Fig. 4.7. The phase angle in each case was $\psi = 75 \pm 2°$. The apparent interfacial toughness values for specimens E-1 and E-2 were comparable, 0.94 and 0.95 J/m^2 respectively, while that of specimen E-3 was somewhat lower at 0.86 J/m^2. The differences here do not seem to be associated with the different geometries induced by shrinkage mismatch; the values of G_c for specimen E-3 with and without the consideration of geometry distortion were determined to be 0.86 and 0.85 J/m^2, respectively. The different mechanical responses of specimens from groups E-1 and E-2 vs. E-3 must therefore lie in either the intrinsic interfacial toughness or in the elastic properties of the sintered phases.

We can begin the discussion of the results presented in Table 4.4 by first looking at specimens from groups E-1 and E-2. Referring to Fig. 4.6, we see that specimens from group E-2 exhibited a much higher adhesive load than did those from group E-1, and from the outputs presented in Table 4.4 it is clear that this occurred without a change in interfacial toughness. This suggests that the increased content of sintering activators and the attendant changes in sintering shrinkage did not appreciably affect the degree of mechanical interlocking at the interface in these materials. Instead, the increase of the adhesive load in specimen E-2 may be attributed to the increased stiffness of the W layer due to its higher content of sintering activators (specimen E-2 is more than twice as stiff as E-1 according to Table 4.3). In other words, higher

load was required to delaminate specimen E-2 because of the improved densification and higher elastic modulus of its W layer, even though the degree of mechanical interlocking in specimens from groups E-1 and E-2 was comparable.

Turning our attention now to a comparison of specimens from groups E-2 and E-3, we see a different trend. Although the adhesive load in Fig. 4.6 is significantly lower for specimens from group E-3 than for those from group E-2, the Young's modulus in Table 4.3 is very similar for the two groups of specimens. In this case the weakening of specimens from group E-3 may be due to a partial loss of mechanical interlocking via a change in morphology and distribution of pores along the interface, as reflected in the reduced apparent interfacial toughness value given in Table 4.4. This reduction in G_c is likely a result of shrinkage mismatch of W and Al_2O_3, which is exacerbated at relatively high contents of Ni and Fe activators. Even though the magnitude of residual stresses that arise from shrinkage mismatch is generally much smaller than that of thermal stresses and they may be relaxed completely during the isothermal firing period, increased shrinkage mismatch is known to lead to the formation of interfacial defects [88, 95], and breakage of some mechanical interlocks at the interface may therefore be expected.

Combining the above modeling results, the origin of the concave-downward trend seen in all of the data sets in Fig. 4.6 can now be reviewed. The initial increase in adhesive load with sintering activators stems primarily from densification of the individual layers, and the improved stiffness that derives therefrom. The weakening of the system that follows at higher levels of activation results from a degradation in the interface quality, apparently due to shrinkage mismatch that compromises the adhesion between layers. The extreme example of this case is specimen C-5 in Fig. 4.6, which could not be prepared as a monolithic specimen, but instead delaminated during firing, presumably due to mismatch stresses evolved on cooling.

These results may have some relevance for practical situations involving co-sintered systems, where the stress/load required to cause interfacial failure is of more importance than the interfacial fracture toughness: the sintering schedule, the concentration of sintering additives, and particle size must all be carefully controlled to optimize both densification of the layers (which stiffens the system and increases P_a) and the shrinkage mismatch between layers (which degrades the interfacial toughness and lowers P_a). For example, for the W/Al_2O_3 bilayer system under investigation, relatively high values of P_a were obtained when the concentration of sintering activators in W fell somewhere between 1 to 2 monolayers. Recalling that powders E-1, 2 and 3

are representative of normal powder character variability that can be expected in an industrial setting, it is clear that control of impurities and conscious incorporation of sintering activators are required to optimize the mechanical strength of co-sintered systems. Finally, we note that although each of the three curves in Fig. 4.6 has a similar shape, the positions of these curves are significantly different. This result is a consequence of other contributors of the system strength: particle size and particle size distribution can also have a significant influence on P_a because these parameters affect densification and potentially the mechanical interlocking along the joining interface when powders of different sizes are used.

4.3.6 Summary

Four-point bending delamination experiments were used to evaluate the strength and adhesion of co-sintered W/A_2O_3 bilayer composites processed at low firing temperatures. By varying the concentration of sintering activators in the W layer, the shrinkage mismatch and sintered properties of the composite were manipulated in order to evaluate their individual contributions to the adhesion of co-sintered materials. It was observed that the adhesion of the bilayer (as measured by the load applied at delamination) exhibited an unusual trend with increasing content of sintering additives, first increasing and then subsequently decreasing. Numerical finite element analyses suggest that the initial increase in adhesive strength can be attributed to the enhancement in sintering and hence improved stiffness of the W layer, while the decrease of adhesive load at relatively high additive contents is a result of interface weakening. The expected breakage of some mechanical interlocks at the interface due to a higher degree of shrinkage mismatch is consistent with this result. Consequently, in order to maximize the adhesive strength of a co-sintered bilayer, both the densification-related properties of the individual layers as well as the sintering mismatch should be carefully controlled through the use of sintering additives and control of other sintering protocols.

4.4 Concluding Remarks

The study performed in this chapter illustrates that bonded W and Al_2O_3 can be produced at low firing temperature (<1200°C). Depending on the degree of sintering of the individual components and particle characteristics, the interfacial adhesion may vary. As shown in Ch. III, Ni and Fe are sintering activators that improve the sintering of W, and here we observe that these additives also affect the interfacial adhesion of W/Al_2O_3 by modifying the mechanical properties of W and by generating shrinkage mismatch between the joined materials. The studies performed in Ch. III and Ch. IV therefore suggest that the knowledge of the extent of shrinkage and densification of each sintered layers are very important for the production of co-fired W/Al_2O_3. Calculations of these sintering parameters for activated W powders with any given particle size distribution are outlined in Appendix B.

The study conducted in Ch. IV also illustrates that interfacial adhesion of bonded materials can be considered from two different perspectives – "fundamental adhesion" and "practical adhesion" [113]. While the first term is associated with interfacial toughness, which is in turn controlled by chemical or mechanical interactions along the interface, the second term refers to force or work required to separate the two materials, which is a function of fundamental adhesion and various experimental factors such as loading configuration, specimen geometry, and material properties of the individual layer. While fundamental adhesion measurements yield an intrinsic property of the interface, the practical adhesion measurement includes other contributions, and thus it has a direct engineering value in assessing the performance of a joined component used in particular applications. The critical strain energy release rate and the adhesive load evaluated here in this chapter may be regard respectively as fundamental and practical adhesion, while adhesion assessed by the tensile pull test (to be discussed in Ch. V) may be regard as practical adhesion.

In the next chapter, the influences of various processing parameters associated with slurry-based processing will be investigated with specific reference to the interfacial adhesion and sintering properties of W and Al_2O_3. Similar to the material system considered in this chapter, that studied in Ch. V does not contain chemical additives that induce a migration of liquid phase, so W and Al_2O_3 are again joined primarily through mechanical interlocking of co-sintered particles. In addition to Ni additives in the W layer, the influence of SiO_2 additions in the Al_2O_3 layer and the application of stucco sand along the joined interface will be examined.

Table 4.1: Adhesion of Mo and Al_2O_3 joined by various bonding strategies and processed at different temperatures [83].

Joining Process	Tensile Strength of Mo/Al_2O_3 Seals [MPa]	
	1700°C	1500°C
Mo-Mn	20	21.4
Glass Migration	66.2	73.1
Mo-Mn and Glass Migration	64.8	55.2
Interlocking of Particles	11.7	1.52

Table 4.2: The particle size and sintering activator contents of the various W powders used in this study.

Powder	Mean Size	Ni Content		Fe Content	
	[μm]	[wt. %]	[# monolayers]	[wt. %]	[# monolayers]
C-1	2.2	0.005	0.13	0	0
C-2	2.2	0.02	0.5	0	0
C-3	2.2	0.06	1.5	0	0
C-4	2.2	0.09	2.5	0	0
C-5	2.2	0.19	5.0	0	0
D-1	2.1	0.014	0.32	0.038	0.91
D-2	2.1	0.04	0.9	0.038	0.91
D-3	2.1	0.07	1.6	0.038	0.91
D-4	2.1	0.10	2.3	0.038	0.91
E-1	1.7	0.006	0.11	0.018	0.37
E-2	1.5	0.015	0.28	0.039	0.79
E-3	1.4	0.025	0.44	0.092	1.75

Table 4.3: Flexural modulus and linear shrinkage of free-standing, single-layer specimens of W (from powders of series E) and Al_2O_3.

Materials	Young's Modulus [GPa]	Linear Shrinkage [%]
W (E-1)	23.2	0.8
W (E-2)	52.4	2.73
W (E-3)	54.5	2.85
Al_2O_3	0.2	0.1

Table 4.4: Inputs and outputs used and obtained in the finite element analyses; Poisson's ratio (ν), and CTE are from Refs. [103-106], while bending load at crack propagation (P_p) was measured experimentally using the four-point bending delamination test in Fig. 4.3. The outputs from the analyses include the critical strain energy release rate (G_c) and the phase angle of the delamination failure (ψ).

Specimen	Input				Output	
	ν	CTE [ppm/K]	P_p [N]	P_a [N]	G_c [J/m^2]	ψ [degree]
W (E-1)	0.28	6.0				
W (E-2)	0.28	6.0				
W (E-3)	0.28	6.0				
Al_2O_3	0.22	8.3				
W/Al_2O_3 (E-1)			140	151	0.94	73.8
W/Al_2O_3 (E-2)			310	340	0.95	75.7
W/Al_2O_3 (E-3)			200	222	0.86	76.6

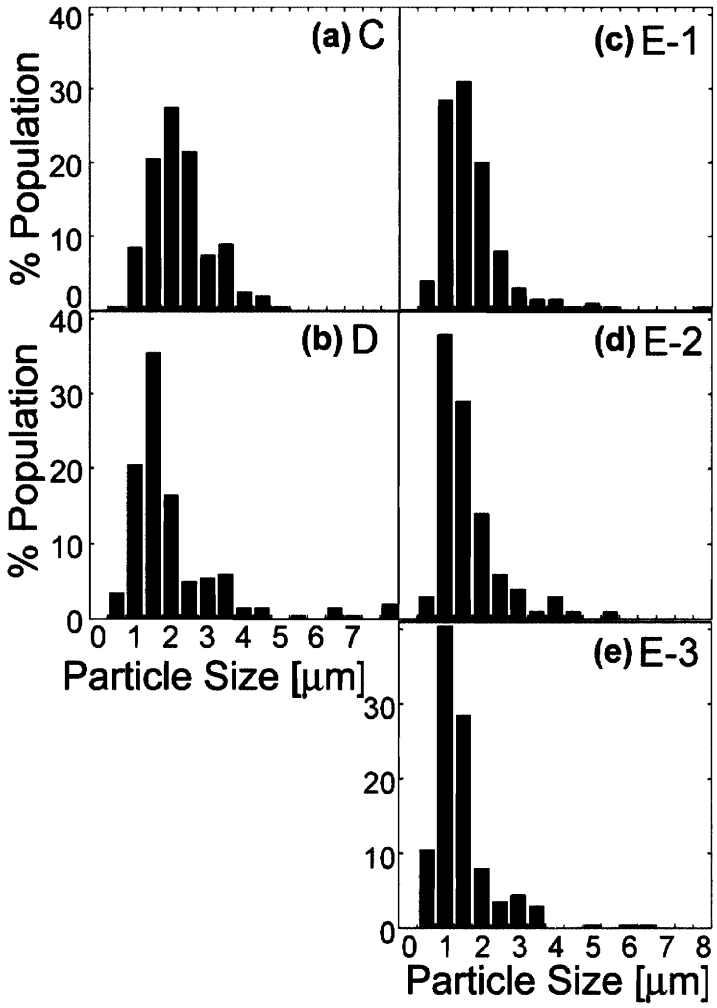

Fig. 4.1: Particle size distribution of the various W powders used in the study. Series C and D powders were all drawn from the same lot with the distributions shown in (a) and (b), while the series E powders were each from separate lots and had slight variations from one another, as shown for E-1 (c), E-2 (d), and E-3 (e).

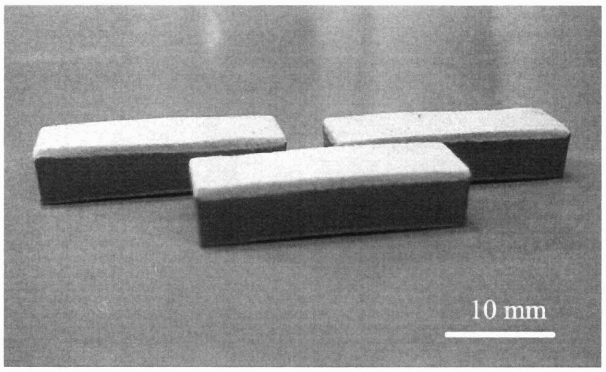

(a)

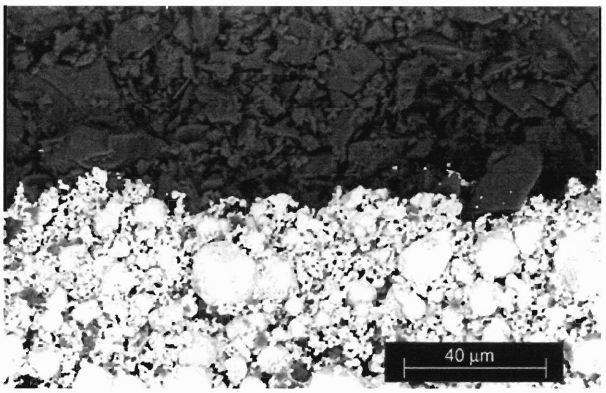

(b)

Fig. 4.2a-b: Samples of bi-layer specimens, prepared by cold pressing and firing at 1177° C for 1 hr. in a 3%H_2-97%N_2 atmosphere in (a) a macroscopic view and (b) a magnified view of the interfacial region, observed in a scanning electron microscope. In both views the layer on the bottom is composed of E-2 W powders and the layer on the top is Al_2O_3. The contrast in the images is opposite due to the two different modes of imaging.

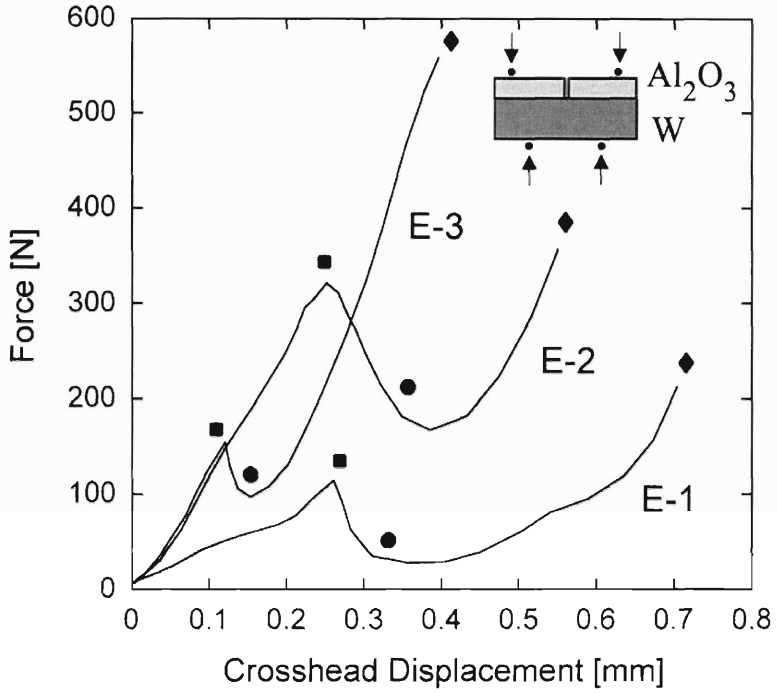

Fig. 4.3: Typical force-displacement curves obtained from the four-point bending delamination test. Representative test results for specimens from groups E-1, E-2, and E-3 are presented and the points at which interfacial crack initiation (■), crack propagation (●) and through-crack failure (♦) occurred are denoted. A schematic configuration of the delamination test is also shown in the inset.

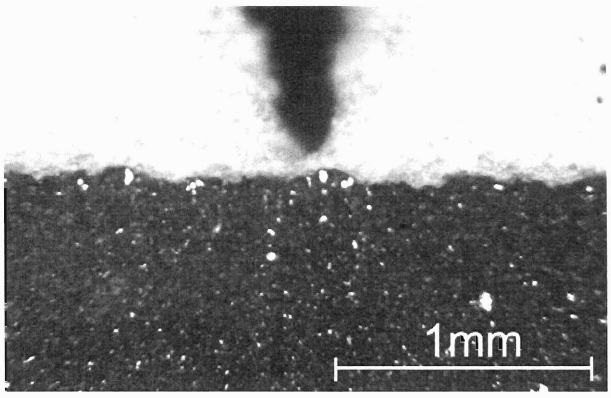

Fig. 4.4a: A co-sintered W (bottom) /Al_2O_3 (top) specimen containing a pre-notch within the Al_2O_3 layer.

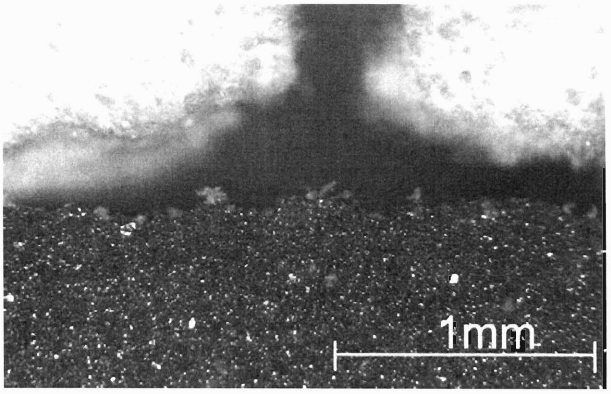

Fig. 4.4b: Interfacial delamination of a co-sintered W (bottom)/Al_2O_3 (top) specimen induced by the bending load.

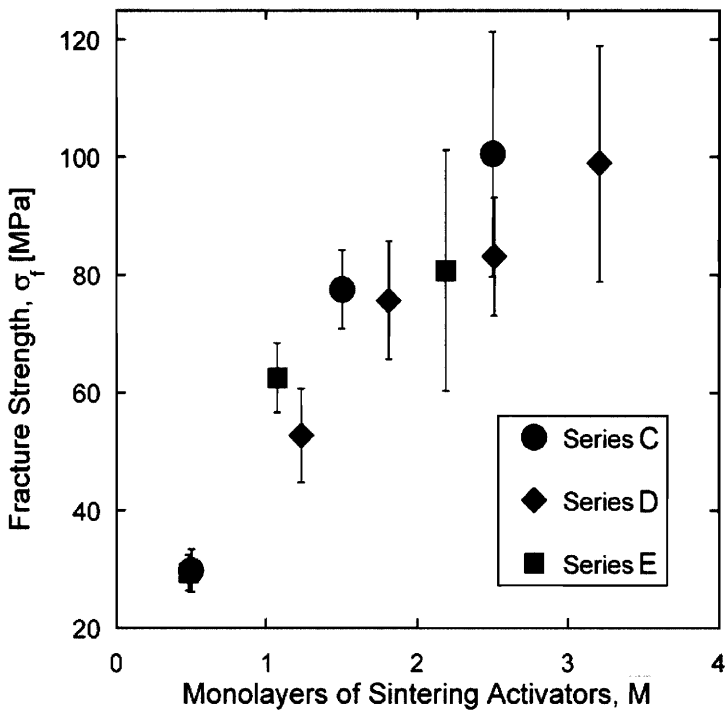

Fig. 4.5: Fracture strength, σ_f, of the W layer for various specimens, as a function of the monolayer coverage of sintering activators. The plotted values are averages of three specimens, and the error bars denote the range of the three measurements.

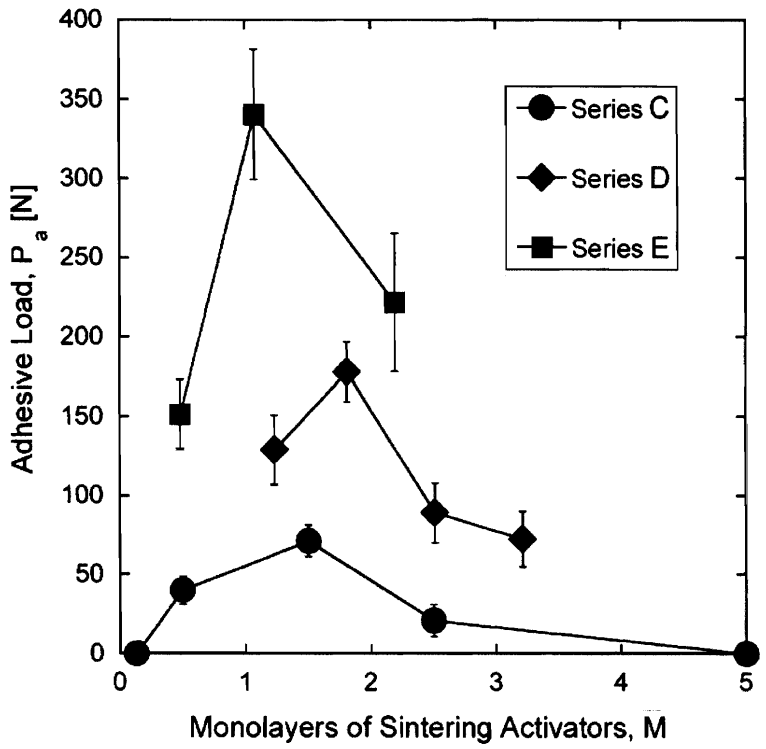

Fig. 4.6: Adhesive load, P_a, of the W/Al_2O_3 co-sintered compacts as a function of the monolayer coverage of sintering activators. As in Fig. 4.4, the points represent an average of three tests and the error bars denote the range of measured values.

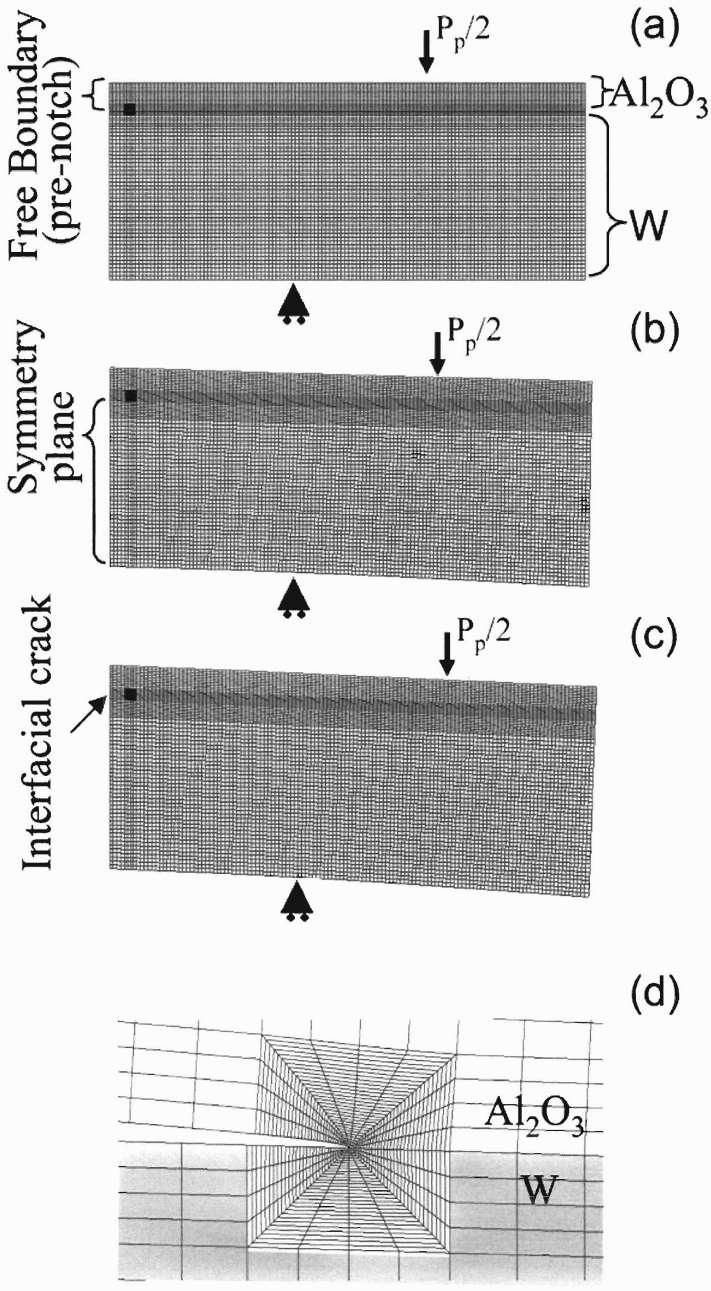

Fig. 4.7: The finite element models of specimens (a) E-1, (b) E-2, and (c) E-3, and (d) a zoomed view of a representative crack tip region. Note the different degrees of shape distortion in the three specimens.

Chapter V.

Joining of W and Al_2O_3 through a Slurry-Based Processing Route

5.1 Introduction

Powder materials can be consolidated into desirable shapes through various forming methods including dry pressing, plastic deformation forming, and slurry-based processing. The specific method to be used depends on the geometry of the green body as well as the manufacturing cost. Because of its amenability to the production of a component with complex geometry and its superior performance for coating applications, slurry-based processing has been widely employed in industry. For the W/Al_2O_3 system, in particular, a slurry-based tape casting is commonly used to produce W/Al_2O_3 electronic packages [114-116].

In this chapter, specific attention is given to W/Al_2O_3 composites used for investment casting applications. To produce such composites, a slurry-based processing route is employed. Unlike a relatively simple dry pressing method, which was employed in the earlier sections, the slurry-based processing involves a variety of materials (i.e., powders, solvent, binder, etc.) and several steps of processing (i.e., coating, drying, dewaxing, etc.). All of these add to the complexity of production. Clearly, for one to control the quality of co-sintered W/Al_2O_3, an understanding of how processing parameters associated with each processing step may influence properties of the materials is crucial.

The main objective of this chapter is to investigate how various processing parameters involved in the process of slurry-based investment production affect the adhesion and sintering properties of co-sintered W/Al_2O_3. In the following two sections, background on (i) powder consolidation methods with an emphasis on slurry-based processing and (ii) investment casting are provided. A study of the influences of processing parameters on properties of W/Al_2O_3 composites is presented in Section 5.4.

5.2 Powder Consolidation Methods

Forming methods for powder materials can be classified into three main groups:

- Dry Pressing
- Plastic Deformation Forming
- Slurry-Based Processing

a. Dry Pressing:

Pressing refers to a process whereby powder materials can be formed into a desirable shape through the application of compaction pressure in a rigid die or a flexible mold. Often, the stock material consists of agglomerated granules of particles which may contain binders and plasticizers, and spray drying or spray granulation can be used to prepare such powder feed. The two main types of pressing operation are uniaxial pressing and isostatic pressing. In the former case, the pressure is applied either by a single punch from one end of the die, or by two punches from both ends. On the other hand, in the case of isostatic pressing, with the use of a flexible mold (such as a rubber bag) inside a liquid pressure chamber, pressure is exerted equally on all sides of the mold. This operation can help eliminate the problem of density gradients that may exist in uniaxial pressing. Among the advantages of pressing are that the process is relatively simple and can be quickly executed. Because no liquid solvent is used, a pressed product can be made with close tolerances without drying shrinkage. The process however has a limitation in shape complexity, especially when internal geometries are important.

b. Plastic Deformation Forming:

The plastic deformation forming process relies on the use of a material mixture consisting of powders and binders which can flow plastically upon the application of pressure. The forming techniques of this type include extrusion and injection molding. Traditionally, injection molding is a method used for forming thermoplastic polymers. To apply injection molding to powder materials, the powder needs to be mixed with polymeric organic binders, such as paraffin wax or polypropylene, with a content as high as 35-50% by volume. Other additives may include plasticizers and lubricants. The mixture is then heated above the softening point of the polymeric vehicle and is forced into the cavity of a cool mold, where the polymer solidifies to give a rigid green body. Prior to firing, the binder needs to be removed from the inorganic

material network. As the consolidated viscous material can easily flow and conform to the mold's geometry, injection molding is potentially a high volume production process which allows the fabrication of parts with extremely intricate shapes. The high equipment and tooling costs, and the generation of flaws that usually occur during mold cooling and long binder removal stages however limit injection molding from being the major forming process for powder materials. Instead, it is mainly employed to fabricate small components for special applications where a key requirement is net shape forming of complex shapes.

c. Slurry-Based Processing:

Slurry-based processing involves the use of liquid slurries as vehicles for powder materials in the consolidation process. With the good flow properties of slurries, various types of components can be effectively made with the slurry-based processing method, ranging from those with large cross sections, to thin-walled products, to parts of very intricate geometry. Slurries usually consist of powder materials, solvent, and additives that are used to adjust slurry properties. The additives may include binders, plasticizers, dispersants, and wetting agents. The descriptions of these materials are presented below:

- *Solvent*: Solvent is a main component of slurries that provides flowability to solid powders. Traditionally, organic solvents, such as alcohols, ketones, and hydrocarbons, are used as they provide relatively fast drying and usually exhibit good compatibility with other materials in the system [117, 118]. However, since organic solvents usually pose environmental problems due to their toxicity and volatile nature, industry is gearing towards the use of a more environmentally-friendly solvent, namely water, and efforts are being directed towards a better understanding of water-based systems [117-121].

- *Binder*: Binder is used in a slurry mainly to provide green strength before a component is sintered. Various types of binders exist including clay, molecular, vinyl, and cellulose binders. Some of these are in colloidal form while others consist of networks of polymer chains. The use of colloidal silica binder and latex-based binder in W/Al_2O_3 system are discussed in Section 5.4.

- *Plasticizer*: Plasticizer, which is usually a low molecular weight organic substance, can be added to a slurry to modify the viscoelastic properties of the binders. In slurry-based tape casting, plasticizer is one of the main ingredients in the slurry as it helps increase the flexibility of the films, so that they can be handled and processed effectively into desired products.

- *Dispersant*: Dispersant is mixed into a slurry to help stabilize the suspension against flocculation. With good suspension, a slurry is allowed to have high solid loading while remaining at relatively low viscosity. A well-suspended slurry can also be used throughout a forming process without the need for remixing.

- *Wetting Agent*: Wetting agents, such as sodium alkyl aryl sulfonates and sodium alkyl sulfates, are sometime added to a slurry to help promote the wetting characteristics of a slurry on a substrate.

Examples of slurry-based processing techniques are slip casting, tape casting, three dimensional printing, and dip casting. Details of these different techniques are discussed below:

- *Slip Casting*: In the process of slip casting, a slurry containing fine clay, which is called a slip, is poured into a porous gypsum mold. At the inner surface of the mold, capillary suction of the solvent component of the slurry occurs, resulting in the formation of a layer of green body. The thickness of the green layer grows as capillary action continues, and when the desired thickness is obtained, excess slurry can be drained out of the mold. Finally, after removing the cast from the mold, further drying and firing can be pursued. Slip casting is generally used to produce dinnerware and thin-walled products. If the dispersion and viscosity of the slip is well-controlled, the production of a complex shaped component is feasible. While slip casting requires relatively low capital cost, the process has a lower production rate and usually yields a product with lower dimensional precision.

- *Tape Casting*: Tape casting is used to form a thin layer of powder materials. With the use of a device called a doctor blade, a slurry can be applied on a moving carrier substrate, and the thickness of the resulting film can be well-controlled, ranging from few microns to approximately 1 mm [122]. To effectively consolidate powder with this technique, high tape strength and flexibility are required. Tape casting has been employed for numerous electronic ceramic applications such as electronic packages, multi-layered capacitors, fuel cells and photovoltaic cells.

- *Three Dimensional Printing (3DP)*: Three dimensional printing is a solid free-form processing technique that allows the fabrication of very complex three dimensional components. In the process, a jet of stabilized slurry containing no binder is deposited onto a substrate. Following the drying stage, where solvent and dispersing medium are removed, a binder is printed onto the resulting green layer at specific locations according to a 2D image of the component cross-section extracted from a 3D CAD (computer aided design) file. The slurry deposition and binder printing steps are repeated layer by layer until the entire part is built. Prior to firing, the loose powder in the regions without binders present is removed. The 3DP process has been employed to fabricate metal, ceramic, and polymer components with a variety of binder systems [123, 124].

- *Dip Casting*: Dip casting is primarily employed for the fabrication of shells used in investment casting applications. The process involves the application of slurries on patterned wax layer by layer, until a desired thickness is obtained. A detailed discussion of the dip casting process is presented in the next section.

5.3 Investment Casting

Investment casting (also known as lost-wax casting) is a traditional casting process which has been commonly employed to manufacture near net-shape metal and metal alloy components. The main advantage of this casting method lies in its ability to produce a high volume of precision components of complex shapes, in a relatively short time. While archaeological evidence suggests that the first use of the investment process occurred in Thailand as early as in 4500 BC [125], it is from 1940 on, with the drive from the Second World War, that a modern investment casting process has been developed and employed in a wide variety of engineering applications. At the beginning stage of its development, investment casting was extensively used to produce aircraft turbo-supercharger parts and heat resisting alloy components in turbines [126]. Later, the use of investment casting expanded from aircraft and military applications to general commercial applications such as golf clubs, jewelry, and medical implants [127].

Figure 5.1 outlines the processing steps of investment casting, which can be divided into two key steps – shell production and casting of metals. First, shells whose cavity has the same form and geometric details as the finished cast products need to be made through a slurry-based processing route, and the entire process of shell manufacturing may be termed *dip casting* or *investing process*. The shell production step starts with the wax patterning process, which involves formation of wax into a desired shape using the precision die injection process. Small wax patterns can be assembled into a tree, and the parts are connected to one another through gating wax networks. The wax tree is then dipped (i.e., invested) in a slurry containing refractory powder materials, binders, etc. Excess slurry will be drained off, and the wet assembly will be immediately stuccoed with coarse ceramic particles. After drying in an area with controlled temperature and humidity, another layer of slurry dipcoat will be applied on the assembly. Dipping, stuccoing, and drying processes will be repeated until a desired shell thickness is achieved. The type and characteristic of powder materials used may be different from layer to layer depending on the property and economic requirements. Typically, fine powder is used for a primary dipcoat as it can replicate the details of wax patterns well. Coarser powder may be used for later dipcoats to speed the thickness build-up.

After the dipping stage is complete, wax can be removed from the assembly through interaction with hot steam inside an autoclave. The wax-free mold will be baked to remove

moisture, solvents and slurry additives, and then fired at higher temperature to sinter the powder materials. To produce shells with porous structure, such that the removal of entrapped gas and moisture can be facilitated during the metal casting step, the shells are partially-sintered at an approximate temperature of ~1000^{o} C (depending on materials). The cooling of sintered shells marks the final step of dip casting process for shell production. Casting then occurs by pouring molten metals into the shell. Following the solidification of the cast metal, the shell can be knocked out from the castings, and final finishing, machining and inspection can be performed.

5.4 The Influences of Processing Parameters on Adhesion of W and Al_2O_3

5.4.1 Introduction

Since pattern waxes can be assembled into a tree and several shells can be produced simultaneously, castings can be manufactured in high volume using the investment casting process. However, dip casting for shell production involves many processing steps, as discussed earlier. A long processing sequence makes the shells somewhat susceptible to flaw generation that may compromise shells' integrity. If processing parameters associated with each processing step in dip casting are not well controlled, the formation of defects, such as inclusions and scabs that are detached from casting shells and localize at the surface of cast metals, could result [128].

With its refractory nature and good thermal stability, Al_2O_3 is often used as a material for shell production. Al_2O_3 however may chemically interact with some cast metals and this makes the material unsuitable for certain applications. To overcome this drawback, W may be used as a primary dipcoat, which functions as a reaction barrier between the melt and Al_2O_3. The performance of such W/Al_2O_3 composites clearly relies on the adhesion and sintering properties of the materials, which in turn can be influenced by various processing parameters associated with each processing step of dip casting.

While joining of W and Al_2O_3 for electronic packaging application has been studied considerably [77, 80-82, 114], public domain literature on the processing of co-sintered W/Al_2O_3 for investment casting applications does not exist. Although a slurry-based processing route is employed in both cases, the unique processing method for casting applications, which involves dipping, dewaxing, and low-temperature co-firing, is quite distinct from that used for electronic packaging applications. It should also be noted that, commonly, organic solvents, such as alcohol, toluene, ethoxyethanol, and terpineol are employed as solvents for slurries used in tape casting of W/Al_2O_3 electronic packages as well as for slurries used in dip casting of Al_2O_3 shells [77, 129-131]. Compatible aqueous slurries for the fabrication of co-sintered W/Al_2O_3 are yet to be developed.

It is the purpose of this work to experimentally investigate how various processing parameters involved in the production of W/Al_2O_3 shells from aqueous slurries can influence adhesion and sintering properties of the composites. The processing parameters of interest include drying conditions, binder content, application of stucco sand, and powder characteristics. A study was performed using aqueous slurries for W and Al_2O_3, which had been characterized

and developed in a separate study that is not of direct relevance to this thesis; a detailed discussion of that investigation is provided in Appendix C. In the next section, background of the processing parameters will be discussed.

5.4.2 Processing Parameters

a. Drying Conditions:

Drying refers to removal of liquid from a porous body. For dip casting, each dip may either be partially or completely dried before the application of the next dip, and drying is usually conducted by hanging a wet assembly in an area with controlled temperature, humidity, and air flow [132]. In the early stage of drying, a meniscus of liquid solvent is formed at the surface of a drying layer and evaporation of the solvent is controlled by the capillary force, according to [133]:

$$P = -2\gamma_{LV} / r_m \qquad (5.1)$$

where P is the capillary pressure, γ_{LV} is the liquid/vapor interfacial energy, and r_m is the radius of the meniscus, which decreases upon drying. In this first drying period, shrinkage of the drying layer occurs, mostly in the thickness direction, and the drying rate is relatively fast and independent of time. Soon, as r_m approaches the size of pores, the meniscus recedes into the pores, marking a falling rate period where drying slowly progresses and is limited by diffusion of vapor phase from the interior of the drying layer.

With its low strength in the green stage, the drying body is prone to the generation of defects. It has been suggested that biaxial tensile stress, which may be responsible for drying cracks, can develop in a drying film in two ways [134]. First, a moisture gradient may be established across the thickness of the drying layer, either due to a rapid drying rate or differential liquid content when the part is initially formed. This moisture gradient is responsible for differential shrinkage which generates stress in the drying body. Alternatively, biaxial tensile stress can arise in the drying layer due to dimensional constraint of the substrate which prevents shrinkage, induced by the capillary pressure, to occur in the planar directions. In either case, if drying cracks should form, W/Al_2O_3 shells with good adhesion between the materials will not result. In this work, one particular focus is a study of how drying rate can affect the generation of cracks in Al_2O_3 layers containing colloidal silica binder. The influences of other processing

parameters, including binder content and sand size, on drying crack formation will also be examined.

b. Colloidal Silica Content

Colloidal silica (SiO_2) is one of the most common types of binders, which are primarily employed to help improve green strength of dip casting shells [131, 132]. It can be used with aqueous or non-aqueous solvents and consists of spherical, nano-sized, amorphous silica particles (i.e., silica sols). With the presence of alkaline ions, such as sodium or ammonia, the particles are dispersed and stabilized in a solvent. Upon drying, reduction of pH, or the addition of ionic salts that can neutralize the surface charges of silica particles, the particles become destabilized, interact more frequently, and adhere to one another to form strands of a three-dimensional solid network that provides green strength to a component. This process is known as polymerization or gellation.

In addition to green strength, SiO_2 also helps improve the sintering of Al_2O_3. A separate investigation was performed to examine the sinterability of Al_2O_3 at various concentrations of SiO_2, ranging from 0 to ~9 wt. % (See Appendix D). It was found that with an increase of SiO_2 content, sintering shrinkage of Al_2O_3 increases gradually, while the rupture strength of the material increases significantly. This may suggest that surface diffusion of Al_2O_3 is primarily enhanced when SiO_2 is added. A discussion of this study is presented in Appendix D.

Similar to Al_2O_3, SiO_2 can react with melts of some metal alloys during investment casting production. This may occur, for example in the case of W/Al_2O_3 shells, if slurries which contain colloidal silica binder leach from the Al_2O_3 layer to casting surfaces. To minimize the potential problem, using a small content of SiO_2 would be beneficial in this respect. The optimum content of SiO_2 is assessed in this study through the investigation of how SiO_2 content affects green strength and adhesion of W/Al_2O_3 composites.

c. Application of Stucco Sands

Stucco sands are generally applied between each dipcoat of dip casting shells to prevent further runoff of slurries, and to facilitate a subsequent dipcoat to spread and wet the shells better [135]. With their relatively large particle size, stucco sands also increase thickness buildup of the shells. In addition to these contributions during the dipping stage, it can be expected that the

presence of sand between W and Al_2O_3 layers will also affect adhesion of the joined materials. In this study, the influences of the application of zirconia (ZrO_2) sand and sand size on adhesion properties of W and Al_2O_3 will be examined.

d. Characteristics of W Powder

Several important observations were made in the studies presented in Chapters III and IV, which were performed on dry powder systems: we found that W powders with different particle size distributions can exhibit very distinct green densities (e.g. compact densities; tap densities) as well as different sintering behaviors and, correspondingly, mechanical properties. Secondly, the sintering of W, which is poor at low firing temperatures, can be improved with a small content of sintering additive, and the content of additive in the W layer can affect the adhesion of co-sintered W/Al_2O_3. When powders are used in the form of slurries, additional contributions of powder characteristics on slurries' properties, such as rheological behavior and dispersion, can be expected. These properties need to be well controlled, as they determine the performance of a slurry-based production line. Here, effects of the characteristics of W powders on processing and mechanical properties of co-sintered W/Al_2O_3 for investment casting applications, and the feasibility of the Ni addition technique (activated sintering) for a slurry-based route will be investigated.

5.4.3 Experimental Procedure

Two main types of test specimens were prepared to examine how various processing parameters influence the properties of dip casting W/Al_2O_3 composites, specifically the formation of drying cracks, green strength, sintered strength, and adhesion. The detailed specimen preparation procedure is given below.

a. Two-layer specimens:

Specimens of this set, which consisted of one layer of W and one layer of Al_2O_3, were used exclusively to assess how processing parameters affect drying crack generation. To prepare the specimens, wax pieces cut to the size of 5 x 2.5x 0.8 cm were hand-dipped into aqueous W slurry. The W slurry was prepared with 'series F' W powder (mean particle size of 1.3 μm), Latrix 6300 (a latex binder produced by Nalco Company (Naperville, IL)), and de-ionized water

in 94:3:3 weight ratio (See Appendix C for detailed descriptions of this W slurry). This resulted in a slurry with W solid loading content of 45 vol. %. To improve the wetting properties of the slurry on a wax surface, a very small amount (0.02 wt. %) of wetting agent (nonionic complex phosphate ester surfactant) was added. All ingredients were mixed by hand-stirring for approximately 30-60 mins. Figure 5.2 and Table 5.1 present the particle size distribution and powder characteristics of series F powder.

Stucco sands were applied immediately after W dips, while some specimens remained sand-free. For those with stucco sands, either large ZrO_2 (300 μm), or small ZrO_2 sand (100 μm) was used. These sands, which were manufactured by Remet Corp. (Utica, NY), were partially stabilized with CaO. SEM micrographs of these sands are presented in Figs. 5.3(a) and 5.3(b). The specimens with W dip were dried in a laboratory environment with temperature and relative humidity of $23 \pm 1^{\circ}C$ and $35 \pm 2\%$, respectively. Figure 5.4 shows some sanded and un-sanded samples.

Al_2O_3 dipcoat was applied onto the specimens in the next step. Three different compositions of Al_2O_3 slurry, containing 8, 18, and 28 wt. % aqueous colloidal silica binder were employed. Al_2O_3 powder (Remet Corp., Utica, NY) with an approximate mean particle size of 4 μm was used in all cases. The powder and binders were mixed with the same general procedure as used for W, except that a binder-to-powder weight ratio of 0.35 was employed, (the Al_2O_3 solid loading content was ~55 vol.%). This constituted an Al_2O_3:SiO_2 weight ratio of 97.3 : 2.7, 94.1 : 5.9, and 91.1 : 8.9 in the three Al_2O_3 slurries.

Following the application of the Al_2O_3 dip, specimens were dried in a partially-closed chamber within which the humidity level was controlled with a humidifier. Specimens in all sets were dried for 1 day in relatively wet drying conditions, ($21 \pm 1^{\circ}C$, $65 \pm 2\%$ relative humidity (RH)), while specimens in some chosen sets were also dried in relatively dry conditions ($23 \pm 1^{\circ}C$, $35 \pm 2\%$ RH). After drying, for all two-layer specimens, the formation of drying cracks was assessed visually and no dewaxing operation was subsequently performed.

We will call these specimens 'Axxyy-zzz', where 'A' refers to the two-layer specimen, 'xx' will designate the percent colloidal silica in the binders (8, 18, or 18), 'yy' will be denoted NS (no sand), SS (small sand), or LS (large sand), and finally 'zzz' will describe the drying condition (wet or dry), (e.g., A28LS-dry).

b. Three-layer specimens:

The specimens of this set contained one layer of W and two layers of Al_2O_3. These specimens were used to examine green strength, sintered strength, adhesion, as well as microstructural evolution of W/Al_2O_3 composites. To prepare the specimens, slurry materials and dipping procedures as employed for the two-layer specimens were used, except that after application of the 2nd dip layer (Al_2O_3), Al_2O_3 sand (500 μm) and another Al_2O_3 dipcoat were respectively applied to enhance the strength of the structure. The Al_2O_3 layers of all specimens were dried under wet drying conditions (21 ± 1^oC, $65 \pm 2\%$ RH) and dipping was performed after each dipped layer had been dried for one day. The dried specimens were dewaxed in a lab-scale autoclave with a 10 minute ramp and 5 minute soak at approximately 106^o C and 40 psi. Subsequently, the specimens were baked in air at 232^o C for 12 hours to remove excess moisture and solvents, and then fired at 1177^o C for 1 hour in a 3% H_2-97% N_2 atmosphere.

In addition to 'series F' W powder, 'series A' W powder which was employed earlier in Chapter III, was also used to prepare two additional sets of specimens – one without Ni addition, and the other containing 0.05 wt% of Ni powder (0.7 monolayer equivalent). In the latter case, dry W and Ni powders were pre-mixed in a high energy powder mixer before blending with the binder. Compared to series F powder, series A powder had relatively low tap density and contained very low impurity levels (See Figs 5.2a-b and Table 5.1).

We will call three-layer specimens prepared with series F powder 'Bxxyy', where 'B' indicates a three-layer specimen, and 'xx' and 'yy' refer to the percent colloidal silica in the binders and sand size, as before, e.g., B8SS. For specimens prepared with series A powder, either A1 or A2 suffix will be appended to the label (A1 = no Ni; A2 = with 0.05%Ni), e.g., B28NS-A2.

The quality and microstructural features of the specimens were examined at the end of each processing step using optical and scanning electron microscopes. Green strength was qualitatively assessed on as-dewaxed specimens through visual inspection. The adhesive peel test [136] was performed to evaluate sintered strength of W (or adhesion of W/Al_2O_3, depending on locations where material was peeled-off) of as-fired specimens. To conduct the test, a piece of adhesive tape was applied onto the test specimens, and a load of 200g was placed onto the taped specimens for 2 minutes before the tape was removed quickly. Additionally, engineering adhesion was evaluated on as fired specimens using the tensile pull test [136, 137]. As discussed

in Chapter IV, the tensile pull test is a common method to examine the adhesion of bilayer materials [77, 83]. To prepare the test specimens, the specimens were coated with marine epoxy on both W and Al_2O_3 sides and attached to holders made from mounting resin. Inspection was performed to ensure that the epoxy did not penetrate into the inner layers of W/Al_2O_3 composites but remained on specimens' surfaces. Tensile fixtures connected to a universal testing machine (Instron, model No.1125) were gripped to the holders and the tests were performed with a displacement rate of 500 μm/min until failure occurred.

The descriptions of all test specimens and their associated processing steps are summarized in Table 5.2.

5.4.4 Results and Discussion

a. Two-layer specimens:

Drying profiles of A28LS-dry and A28LS-wet specimens dried under different conditions are shown in Fig. 5.5. The weight loss data for these specimens were collected by weighing the drying specimens on a scale interfaced to a data acquisition computer. The drying rates of A28LS-dry and A28LS-wet specimens in the constant drying rate period were determined to be 3.8 and 1.4 g/m^2s, respectively. As expected, a relatively longer drying time was required before reaching the end of the first drying period when dried in the wet condition. Despite the difference in drying rate, drying cracks were observed in the Al_2O_3 layer for both sets of specimens. Additionally, drying cracks also developed in A28SS-wet specimens, which were dried at relatively low rate. An example of the drying crack pattern formed in the Al_2O_3 layer is shown in Fig. 5.6. Similar results that show the independence of crack formation on drying rate were obtained in the case of A18yy-zzz specimens. Specifically, drying cracks in the Al_2O_3 layer were developed in specimens A18LS-dry and A18LS-wet, as well as in specimens A18SS-dry and A18-SS-wet. For specimens A18NS, however, no drying cracks were formed in either drying condition.

Figure 5.7 presents the influences of stucco sand and colloidal silica binder content on drying crack formation in the Al_2O_3 layer of the specimens, which were all dried under wet conditions. It was observed that the thickness of Al_2O_3 layer (2^{nd} dip) increased when ZrO_2 sands were applied between the W/Al_2O_3 interfaces and became larger with an increase in sand size. This underlines how stucco sand can be used to enhance shell buildup rate. Figures 5.8(a)-

(c) present cross-sectional SEM micrographs of some specimens, which show how layer thickness was increased with sand application. As noted earlier, drying cracks developed in specimens A28SS, A28LS, A18SS, and A18LS. Figure 5.7 shows that all of these specimens exhibited a relatively thick Al_2O_3 layer. In contrast, drying cracks were not formed in any of the specimens containing no sand, whose Al_2O_3 layer thickness was below 600 μm. For the case of specimens with the least content of colloidal silica in Al_2O_3 slurries, A8yy, no drying cracks developed even when the thickness of their Al_2O_3 layer was as large as that of the specimens in other groups.

The tendency for drying crack formation at high layer thickness as observed here may be explained by thin film mechanics. Hu et al. [138] examined the mechanics of cracking of elastic homogeneous thin films on rigid substrates, and suggested that there exists a critical cracking thickness below which a biaxially stressed film will not crack:

$$h_c = (K_c / 1.4\sigma)^2 \qquad (5.2)$$

where K_c is fracture toughness, and σ is the magnitude of the biaxial stress. At any particular h_c, the energy gained in relieving the stored strain energy in the film, which in turn relates to σ, needs to be high enough to overcome the energy required to form a crack. For a drying crack, σ can be directly related to the capillary pressure. From Eq. (5.2), we can deduce that if the thickness of the drying layer is large, it is more likely for a drying crack to form, as less stress is required. From our study, the critical crack thickness of specimens A28yy and A18yy are below approximately 760 and 930 μm, respectively. That no drying crack was observed in A8yy specimens whose Al_2O_3 layer was as thick as 1400 μm must be due the low level of biaxial stress in the material. This consequently suggests that low colloidal silica binder content may contribute to lower degree of stress development upon drying. It should be noted also that the idea of a critical cracking thickness has been used in a similar context by Chiu et al. [134, 139], who used critical thickness values coupled with biaxial stress measurements as a mean of evaluating fracture toughness of drying green ceramic materials, via Eq. (5.2).

Drying cracks, such as those formed in the Al_2O_3 (2^{nd} dipcoat) can easily propagate into the subsequent dipcoat layers, and therefore it is important that drying cracking is inhibited in each and every dipcoat layer. Interestingly, it was observed that when alumina sand (500 μm) was uniformly and immediately applied onto the wet Al_2O_3 dipcoats, drying cracks in the Al_2O_3 layer were suppressed in all cases (A8yy, A18yy, and A28yy). This may be due to the

strengthening of the drying network by the presence of the alumina sand. To reduce the tendency for drying crack formation, therefore, the thickness of dipcoats must be uniform and not too thick (i.e., below the critical thickness) and sand must be applied evenly on dipcoat surfaces. While it was found that drying rate did not affect crack formation in these water-based shells (at least in the range of drying rates considered), it is still important to carefully control drying conditions because (i) the kinetics of stress and strength evolution in the drying layers depends on drying conditions – this information can help determine a good next-dip schedule, and (ii) if the layers dry too quickly, several problems could arise including non-uniformity of layer and sand, the formation of an incoherent gel bond of the colloidal silica binder, etc.

b. Three-layer specimens:

i. Colloidal silica content

Figs. 5.9(a)-(c) show as-dewaxed, as-baked, and as-fired B8NS samples. These test shells contained 2.7wt.% of silica within their Al_2O_3 layers (i.e., $2.7SiO_2$:$97.3Al_2O_3$). After dewaxing, some specimens in this group cracked into smaller pieces, indicating inadequate strength of the low-silica alumina layer to sustain the pressure exerted during dewaxing, which arose due to volume expansion of wax upon solid-liquid phase transformation. In the as-baked B8NS specimens, edge delamination of the W facecoat from the alumina layer could be observed. After sintering, the specimens in this group were badly delaminated.

Figs. 5.10(a)-(c) present as-dewaxed, as-baked, and as-fired B18NS specimens. These test shells contained 5.9wt.% silica within their alumina layers (i.e., $5.9SiO_2$:$94.1Al_2O_3$). All specimens in this group remained intact after dewaxing, and had good facecoat appearance after baking. The W facecoat, however, delaminated after firing.

Finally, Figs 5.11(a)-(c) present as-dewaxed, as-baked, and as-fired B28NS samples. These test shells contained 8.9wt.% silica within their alumina layers (i.e., $8.9SiO_2$:$91.1\ Al_2O_3$). The specimens in this group stayed intact with no delamination of the W facecoat throughout each processing step; excellent W facecoat quality was observed in the final fired specimen.

The results obtained in this section clearly show that the quality of W/Al_2O_3 shells increases with silica content in the Al_2O_3 layers. Al_2O_3 needs to contain more than 2.7wt.% of SiO_2 for sufficient green strength. Similarly, to suppress interfacial delamination upon firing, SiO_2 content needs to be as high as 8.9wt.% when no stucco sand is present. One of the potential

explanations why adhesion of the W/Al_2O_3 composites is well-improved with SiO_2 addition is that colloidal SiO_2 may help modify the coefficient of thermal expansion (CTE) of Al_2O_3 to better match that of W. While the CTE (~1000 °C) of W and Al_2O_3 are respectively $6x10^{-6}$/°C and $8.3x10^{-6}$/°C, that of SiO_2 (vitreous) is as low as $0.5x10^{-6}$/°C [106]. A systematic study of how the CTE of Al_2O_3 evolves with colloidal silica content would help explain how silica contributes to the adhesion of the materials.

There was only one set of un-sanded specimens, namely B28NS, that stayed intact after firing; the adhesion pull test could therefore only be performed on those specimens, as discussed in a later section.

ii. Application of Stucco Sands

Following dewaxing, all three-layer specimens containing ZrO_2 sand between the W/Al_2O_3 interfaces were intact, except for B8SS specimens, which exhibited some cracking in the Al_2O_3 layer. Unlike what was previously observed in the case of as-dewaxed B8NS, no cracking of alumina layers occurred in the green B8LS specimens. This suggests that the stucco sands did help strengthen the green specimens against breaking, and large sand is more effective than small sand in this respect. It should be noted also that swelling of the W facecoat in small local regions was observed in some as-dewaxed B18NS specimens. This presumably occurred due to the absorption and expansion of water vapor during dewaxing in the autoclave. This type of defect did not exist in any sample containing ZrO_2 sands examined in this section. After baking, delamination of the W facecoat was observed along the edge of B8SS specimens, similar to what was found in B8NS specimens. All other as-baked sanded samples exhibited good specimen quality.

Figures 5.12a-c, 5.13a-c, and 5.14a-c respectively show W facecoats of as-fired B8yy, B18yy, and B28yy specimens. It was found, especially in the case of low-silica shells (B8yy and B18yy), that zirconia sand helped protect the W layer from delamination. For high-silica shells, no delamination was observed in all cases (B28NS, B28SS, and B28LS). Figures 5.15a and 5.15b show cross-sectional SEM micrographs of B18NS and B18SS specimens (as-dewaxed), respectively. The average thicknesses of the W layer in both specimens were comparable. In the case of the specimen containing zirconia sand, its W/Al_2O_3 interface was more irregular and W slurry appears to have wicked around the sand particles. It can be expected that this type of

structure may enhance mechanical interlocking along the W/Al_2O_3 interface, resulting in higher interfacial adhesion.

Looking at the W surfaces of all as-fired specimens containing large sand (B8LS, B18LS, and B28LS) in Figs. 5.12c, 5.13c, and 5.14c, one can see small pits which were distributed across the surface. This type of defect is unique to shells containing large sand. Optical micrographs of as-dewaxed, as-baked, and as-fired B28LS specimens (Figs. 5.16a-c) reveal that the observed pits are the result of W spallation at sand locations, and that this type of defect actually occurred as early as the dewaxing stage and persisted throughout each processing step. After firing, cracks were seen to emanate from such spallation sites. Figures 5.17a-c and 5.18a-c show the surface quality of B28SS and B28NS in different stages. In the case of samples with small sand, the same pitting defect was also detected, however the spallation size appeared to scale with the sand size (Compare Figs. 5.16a-c with Figs. 5.17a-c). The micrographs presented in Figs. 5.16-5.18 also show that another type of pitting defect, with a size smaller than those discussed earlier (~10-50 μm), can be observed in all groups of specimens after dewaxing.

The results from the adhesion pull test are presented in Fig. 5.19. For the test specimens whose W layer spontaneously delaminated from the Al_2O_3 layer after firing, a strength of zero is denoted on the chart. Various failure locations were observed in different sets of specimens. In specimens B8LS, fracture occurred at low load within the Al_2O_3 layer, indicating that the fired-Al_2O_3 layer was relatively weak compared to the W/Al_2O_3 bonding interface. This is due to the low content of SiO_2 used (See Appendix D). Cracking within the Al_2O_3 layer and along the W/Al_2O_3 interface was observed in all other specimens containing sands (B18SS, B18LS, B28SS, and B28LS). Finally, interfacial delamination was observed in specimens B28NS which contained no sand.

It is observed that the adhesion of these samples as assessed by the tensile pull test is on the order of 1 MPa, which is comparable to that of Mo/Al_2O_3 prepared by co-sintering and considerably lower than that of Mo/Al_2O_3 processed through additional joining strategies such as the glass migration technique [83] (See Chapter IV, Section 4.2). The results also show that the adhesion of W/Al_2O_3 increases with silica content. While the presence of sand and sand size were both found to be important factors that considerably affect the tendency for W delamination in the sintering cycle, the measured tensile load at failure did not vary significantly when such parameters were varied.

The adhesive peel test was performed on as-fired B28NS, B28SS, and B28LS specimens, and the results are shown in Figs. 5.20a-c. In the case of B28LS specimen, a large amount of W was peeled off by the adhesive and failure occurred specifically where large ZrO_2 sands resided underneath. It is likely that the relatively large pits and small cracks extending therefrom (as observed earlier on the W surface of as-fired B28LS specimens) gave rise to stress concentrations for the failure. In contrast, with small or undetected defects, the B28NS and B28SS specimens exhibited excellent peel test results with minimal W detached from the specimens. In all cases, no interfacial delamination of W from the Al_2O_3 layer occurred when the specimens were assessed by the adhesive peel test.

We therefore observe that stucco sand is very influential to the quality of co-sintered W/Al_2O_3 throughout the process of shell fabrication. During dewaxing, its impact is twofold – while sand helps prevent swelling of the facecoat, it usually induces pitting-type defects at this stage. During the firing step, sand may serve as a constraint that hinders the accommodation of sintering shrinkage mismatch stress. Yet it is found that sand also helps enhance mechanical interlocking along the W/Al_2O_3 interface and the net result is that sand helps prevent interfacial delamination of W during processing. Based on this study, it is advisable to use a stucco sand of a size that scales with the thickness of the dip coat. For W/Al_2O_3 composites with approximately 50μm-thick W layer, the results suggest that the use of small sand (100 μm) is appropriate. However, it is conceivable that, with small sand, there will be more loose sand particles only lightly adhered to the coating layers upon drying. Care must be taken to remove the loose sands to prevent the formation of bubbles and hence voids within the shells.

iii. Powder characteristics of W

As discussed earlier, low tap density 'series A' W powder was used to prepare B28NS-A1 and B28NS-A2 specimens. To achieve a good flowability of W aqueous slurry, it was found that the solid loading (SL) of W slurry containing series A powder could not be as high as that employed in the case of the slurry containing series F powder (45% SL), which exhibited viscosity of ~1500 centipoise (as measured by a Brookfield LVT viscometer). This is primarily due to the low compaction ability of series A powder, which is in turn controlled by its particle size distribution (PSD). Even though the particle size of series F and series A powders are approximately the same (Table 5.1), and the difference of PSD of the powders are subtle (Figs

5.2(a) and 5.2(b)), the slightly narrower PSD of series A powder leads to a low tap density of 42% theoretical density (TD) (Compare to that of series F, which is much higher (57%TD)). In the end, 35% SL 'series A' W slurry, which appeared to have slightly higher viscosity than 'series F' W slurry, was chosen for the study.

After dewaxing, specimens in B28NS-A1 and B28NS-A2 groups were intact and had good surface appearance, although swelling of the W facecoat could be observed near the edge of the samples. Good surface appearance was also obtained in all samples after firing. Figures 5.21a and 5.21b show cross sections of as-fired specimens prepared with series A powders without and with Ni additive (0.05wt.%). In comparison, a cross section of the as-fired specimen prepared with series F powder (B28NS) is provided in Fig. 5.21c. The W layer thickness and the estimated sintered densities of the W layers of specimens B28NS-A1, B28NS-A2, and B28NS, are 104, and 92, 29 μm, and 55, 63, 72%TD, respectively. These results indicate that the use of low tap density powder resulted in a W layer with a relatively high degree of porosity, and that Ni, which was added in the W slurry preparation step, did help enhance the sintering of W.

The results from the adhesive peel test performed on as-fired B28NS-A1 and B28NS-A2 specimens show that the W layer did not sinter well in the absence of Ni, as cloudy and spotty W-filled regions appeared throughout the peeled tape (Fig. 5.22a). With Ni addition, a minimal amount of W was observed on the tape (Fig. 5.22b), just as obtained earlier in the case of B28NS. When the adhesion pull test was performed on these as-fired specimens, it was observed that the failure of specimens B28NS-A1 and B28NS-A2 appeared to occur along both W and the W/Al_2O_3 interface, and purely along W/Al_2O_3 interface, respectively. The stress at failure for specimens B28NS-A1 was determined to be 2.2 ± 0.2 MPa, which was of the same order of magnitude but approximately twice as high as that obtained from the specimens made with series F powder. With the incorporation of 0.05 wt.% Ni in W, the measured adhesion was increased to 2.8 ± 0.2 MPa.

From this study, we therefore observe that the characteristics of W powder, specifically particle size, tap density, and impurity content, can significantly influence both processing and mechanical properties of co-sintered W/Al_2O_3. The use of a narrow PSD, low tap density W powder prevents the production of high-density sintered layer at low firing temperature. Furthermore, the Ni addition technique applied in this study is clearly feasible for low-

temperature W/Al_2O_3 shell production, and the sintered strength and the tensile bond strength of co-fired W/Al_2O_3 can be enhanced when an appropriate amount of Ni additive is used.

5.4.5 Conclusion

Several processing parameters important to the production of water-based W/Al_2O_3 dip casting shells were examined. It was found that the formation of drying cracks in the Al_2O_3 layer was controlled by layer thickness and colloidal silica binder content, and was insensitive to drying rate. With an increase of colloidal silica content in the Al_2O_3 layer, both green strength of as-dried Al_2O_3 and adhesion of co-fired W/Al_2O_3 were improved. The adhesion of the composites was further enhanced through the application of stucco sand with suitable size along the joined W/Al_2O_3 interface. The use of stucco sands also affected coating layer thickness, W facecoat quality, and helped suppress drying cracks. Finally, by controlling the particle size and sintering activator content of the W powder, co-sintered W/Al_2O_3 with good sintering and adhesion properties could be produced at low firing temperature through a slurry-based route.

Table 5.1: The characteristics of W powders in series F, A-1, and A-2.

Propery	Series F	Series A-1	Series A-2
Mean Size [mm]	1.3	1.2	1.2
Tap Density [%TD]	57	42	42
Ni [wt.%]	0.015	<0.001	0.05
Fe [wt.%]	0.049	<0.0005	<0.0005

Table 5.2: The descriptions of the test specimens used in the study and their processing steps.

Specimen Set	Dipping			Drying		Baking	Firing
	# layers	wt.% SiO_2 in binder for Al_2O_3 (xx)	Sand at W/Al_2O_3 interface (yy)	Dry	Wet		
A8yy	2	8	NS, SS, LS		•		
A18yy	2	18	NS, SS, LS	•	•		
A28NS	2	28	NS		•		
A28SS	2	28	SS		•		
A28LS	2	28	LS	•	•		
Bxxyy	3	8, 18, 28	NS, SS, LS		•	•	•
B28NS-A	3	28	NS		•	•	•

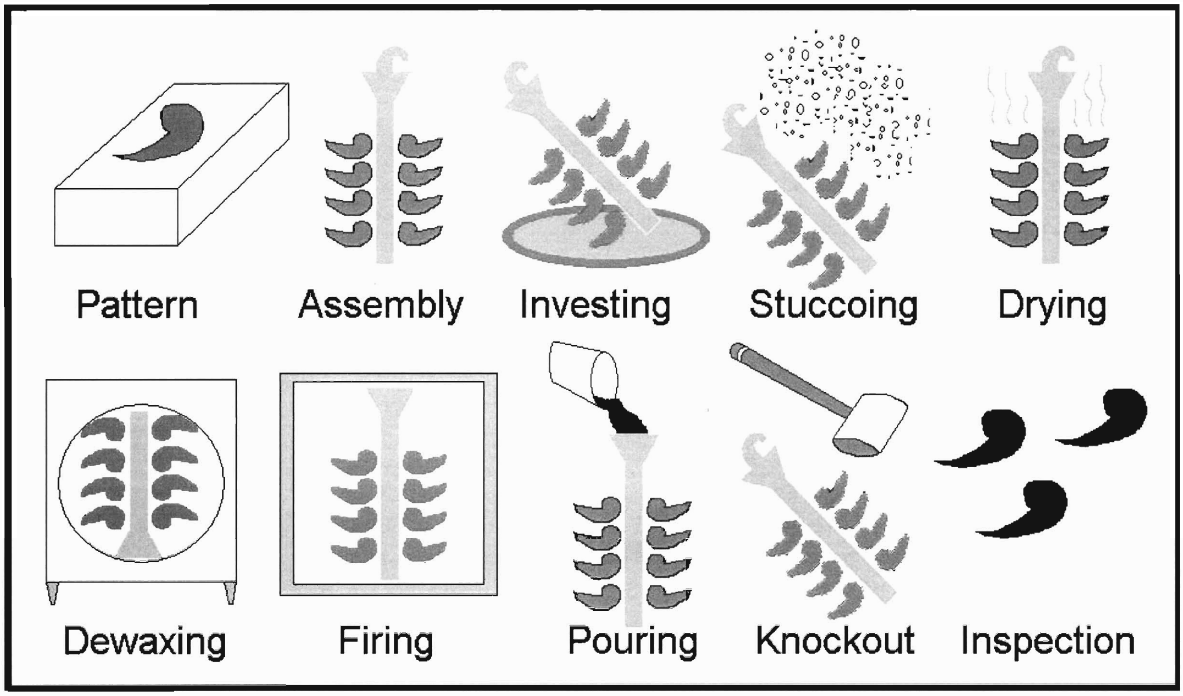

Fig. 5.1: Processing steps of investment casting.

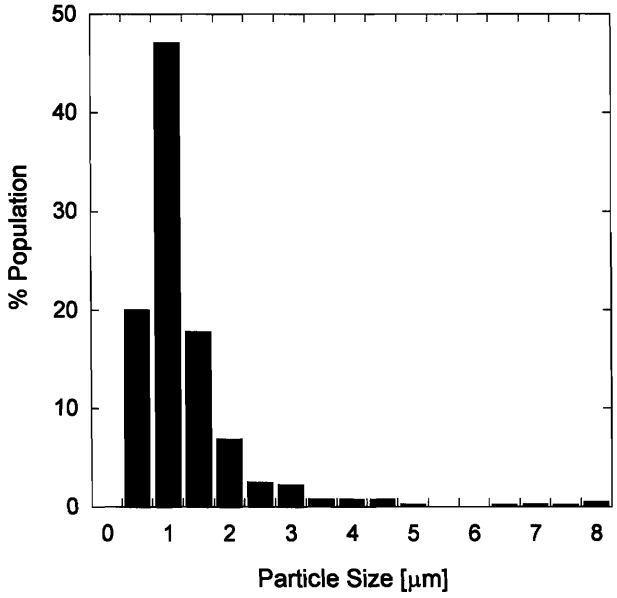

(a)

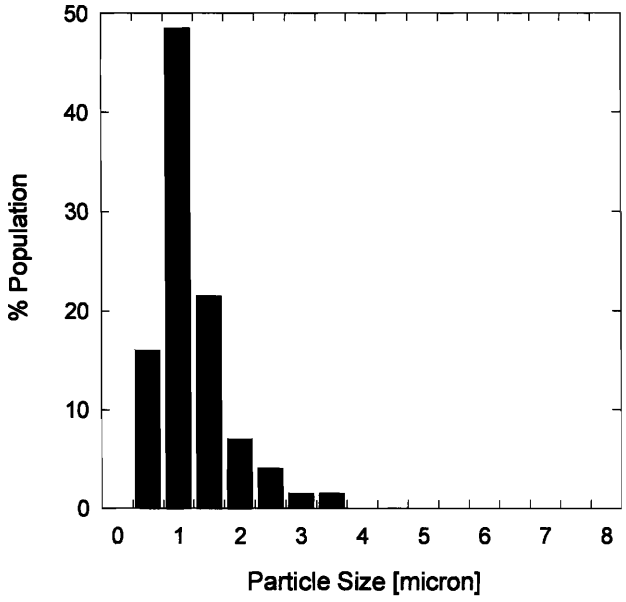

(b)

Fig. 5.2a-b: Particle size distribution of (a) 'series F' and (b) 'series A' tungsten powders.

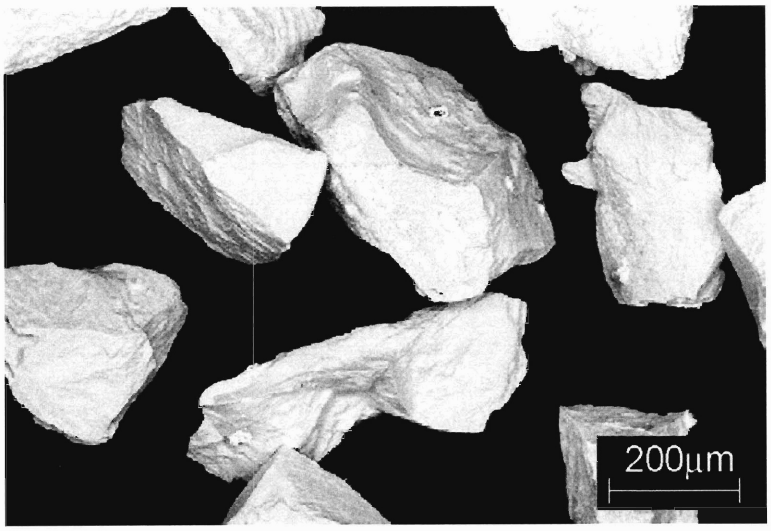

(a)

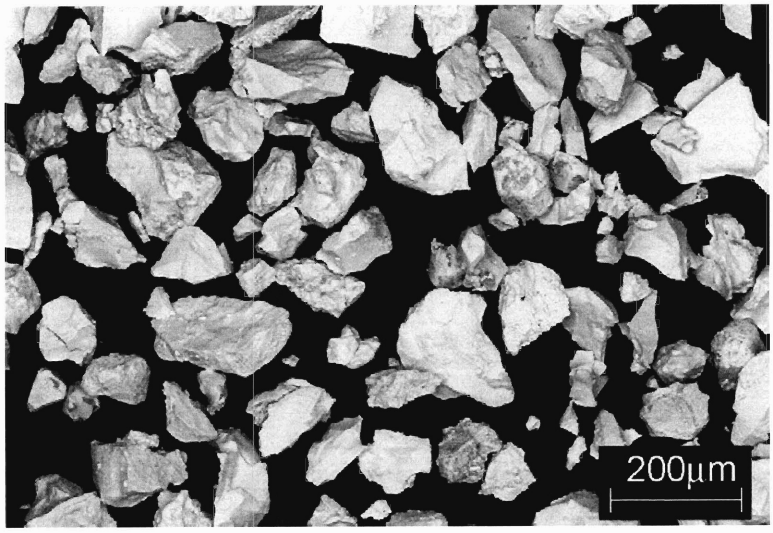

(b)

Figs. 5.3a-b: SEM images of large (a) and small (b) ZrO_2 sands.

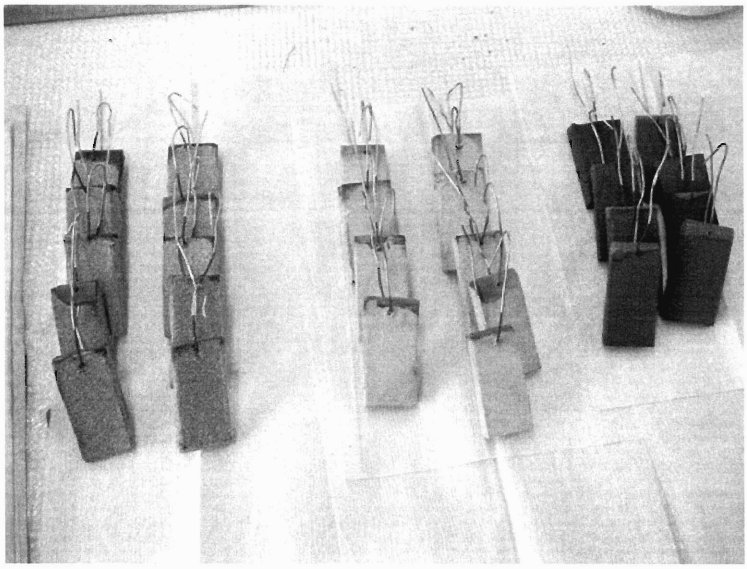

Fig. 5.4: Three sets of specimens which had been dipped with W slurry. Either large zirconia sand (left), small zirconia sand (center), or no sand (right) was applied onto the specimens. They had been hung for drying for one day and would be dipped with Al_2O_3 slurry next.

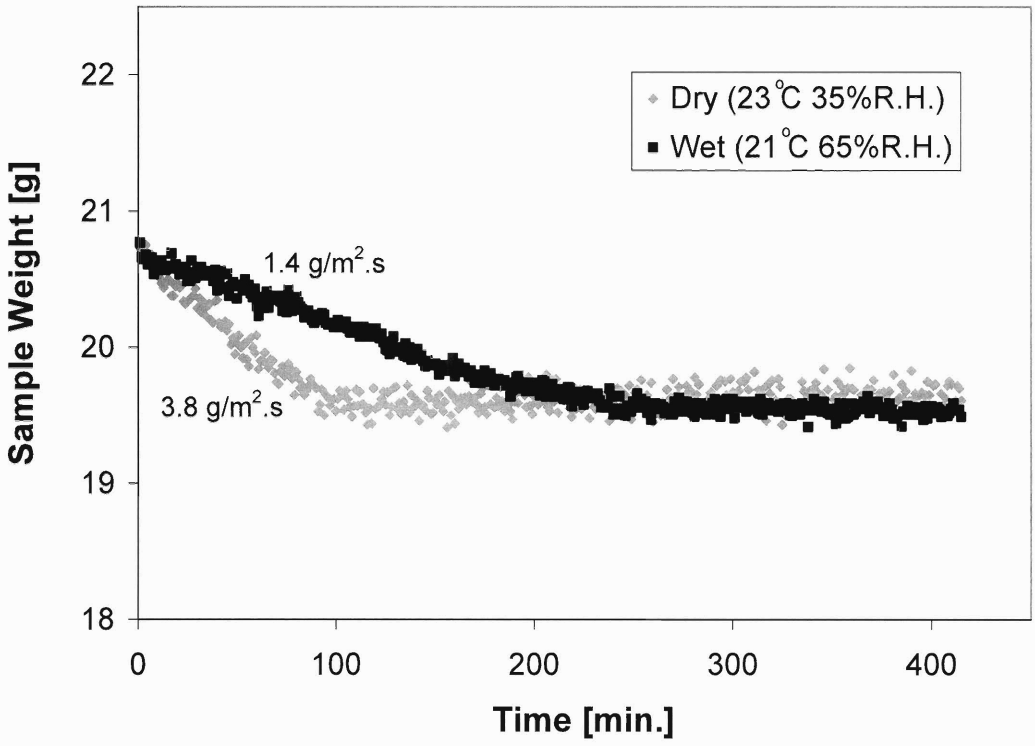

Fig. 5.5: Drying profiles of the Al_2O_3 layer of A28LS specimens which were dried in the 'dry' and 'wet' drying conditions. The drying rates in the 1st drying regime of the specimens are denoted on the chart.

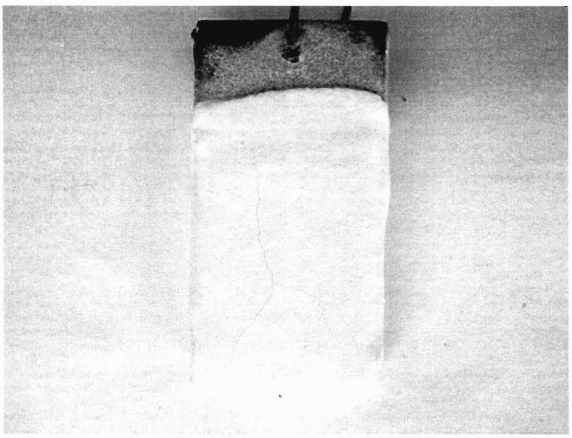

Fig. 5.6: Drying cracks developed on the alumina dipcoat of specimen A28SS-wet upon drying. After dipping the alumina layer, the specimen were dried under wet drying conditions ($21 \pm 1^{o}C$, $65 \pm 2\%$ RH).

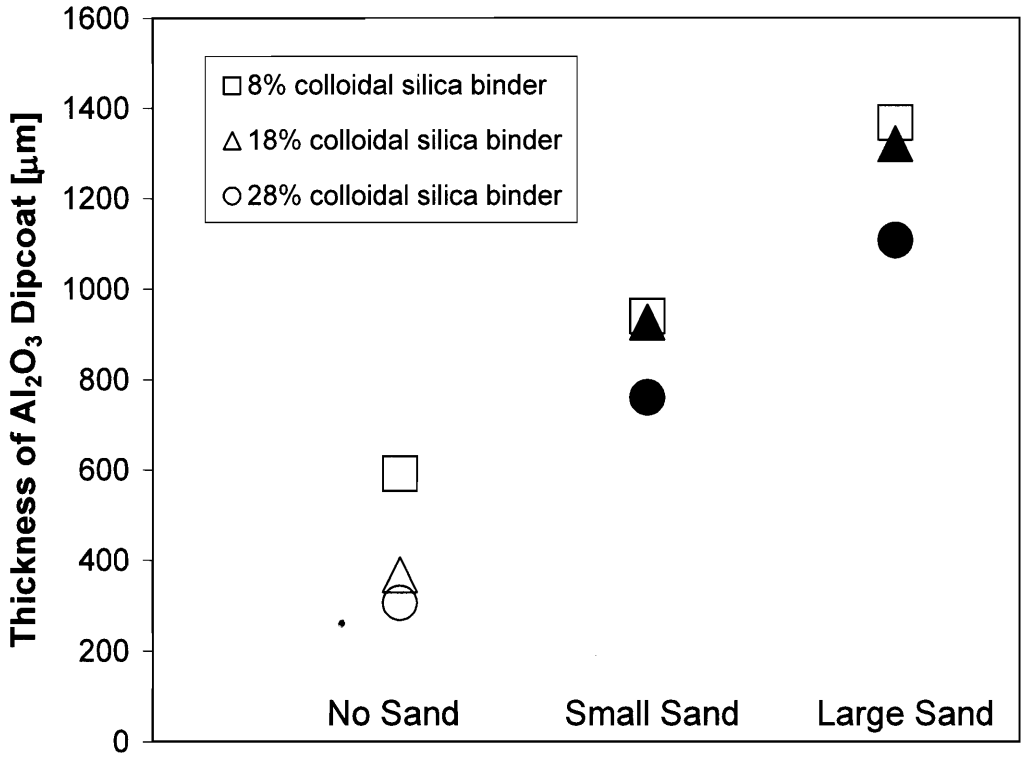

Fig. 5.7: The average thickness of alumina dipcoat of various sets of specimens. The filled marks (●) denote the formation of drying cracks in the alumina layer, while the un-filled marks (○) denote the absence of drying cracks in the alumina layer.

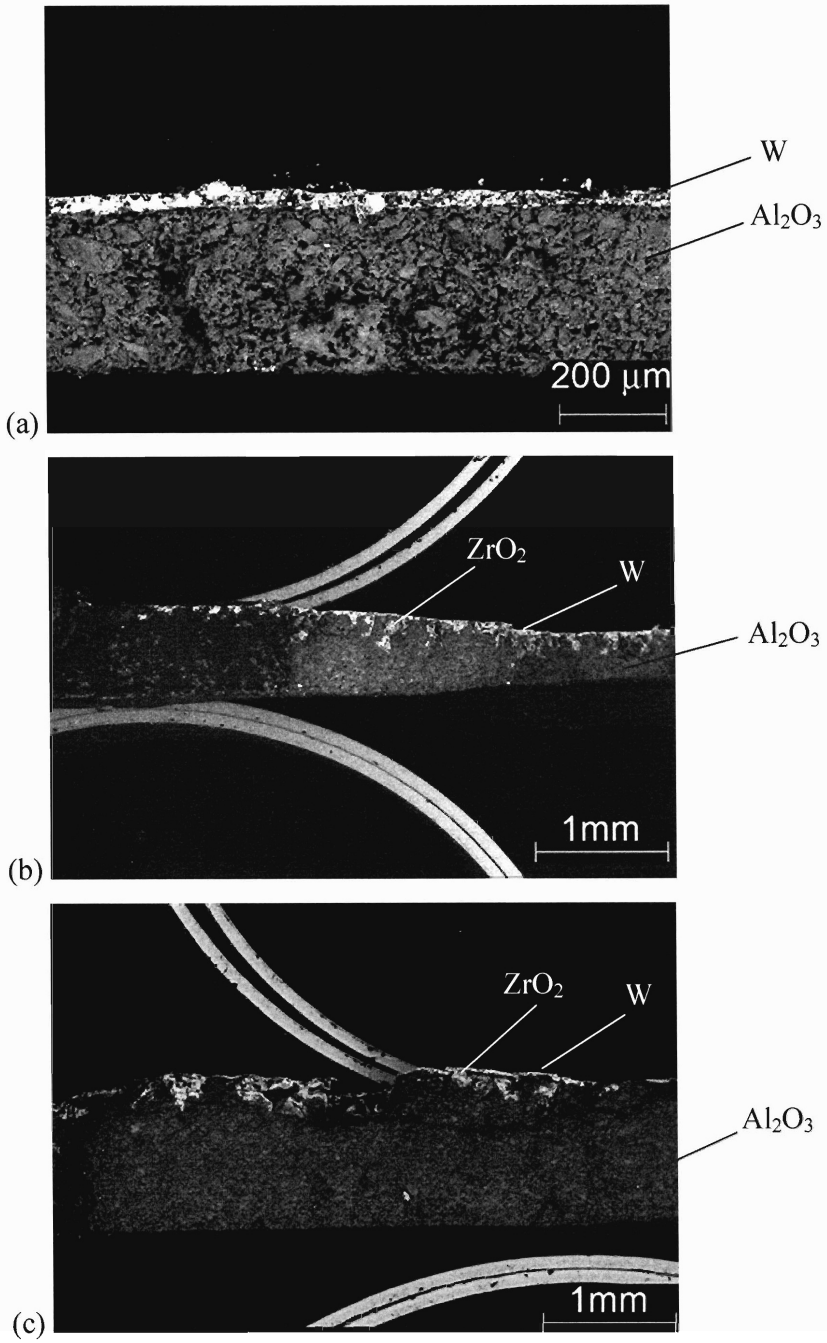

Figs. 5.8: SEM micrographs showing a cross section of (a) A28NS, (b) A28SS, and (c) A28LS specimens. When sands were applied on the W layer, the thickness of the next dipcoat (Al_2O_3 in this case) was significantly increased. This thickness scaled with the size of the sand particles.

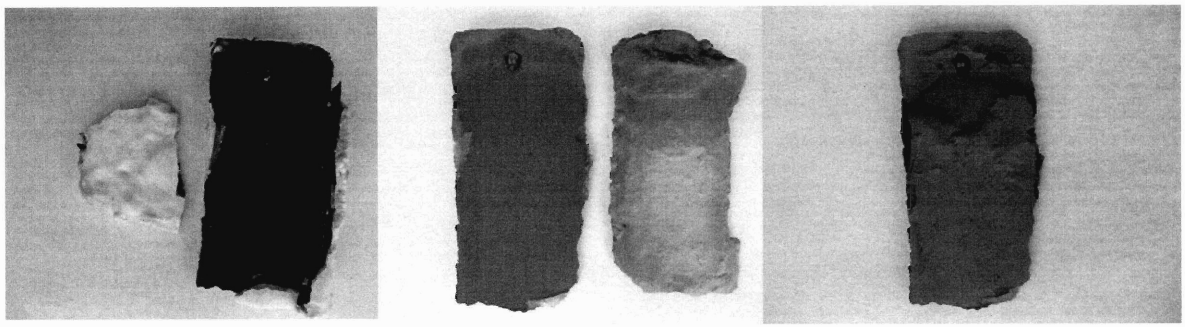

(a) (b) (c)

Figs. 5.9a-c: As-dewaxed (a), as-baked (b), and as-fired (c) B8NS specimens.

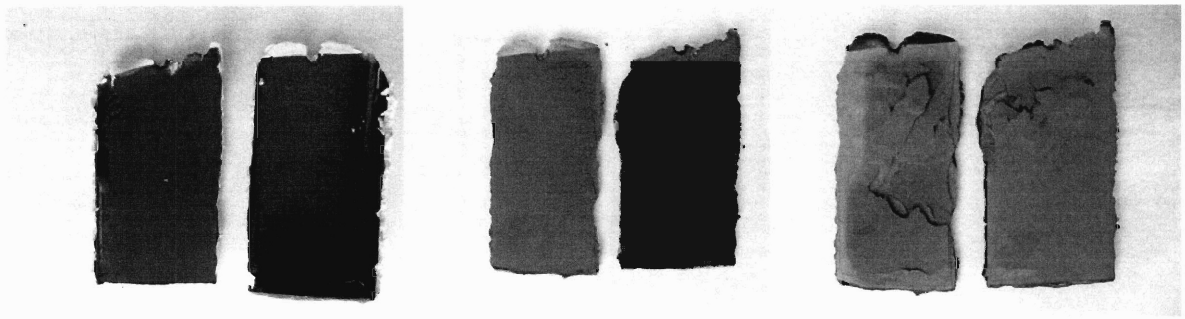

(a) (b) (c)

Figs. 5.10a-c: As-dewaxed (a), as-baked (b), and as-fired (c) B18NS specimens.

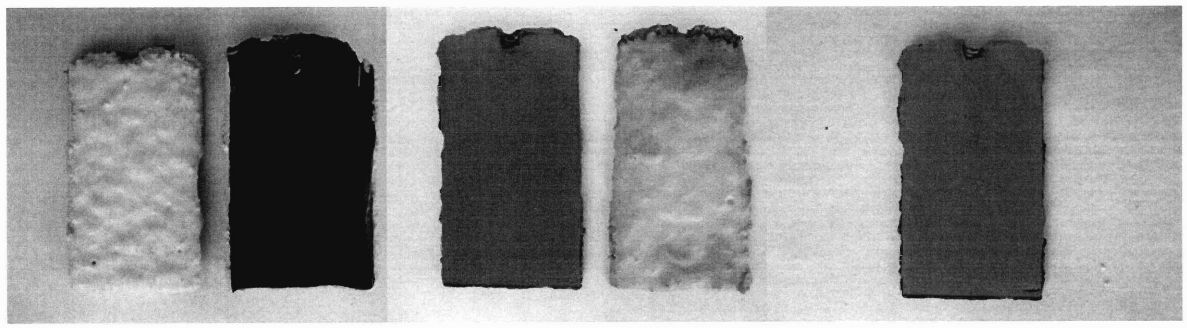

(a) (b) (c)

Figs. 5.11a-c: As-dewaxed (a), as-baked (b), and as-fired (c) B28NS specimens.

NOTE: In Figs. 5.9-5.11, the darker surfaces are W, while the lighter ones are Al_2O_3.

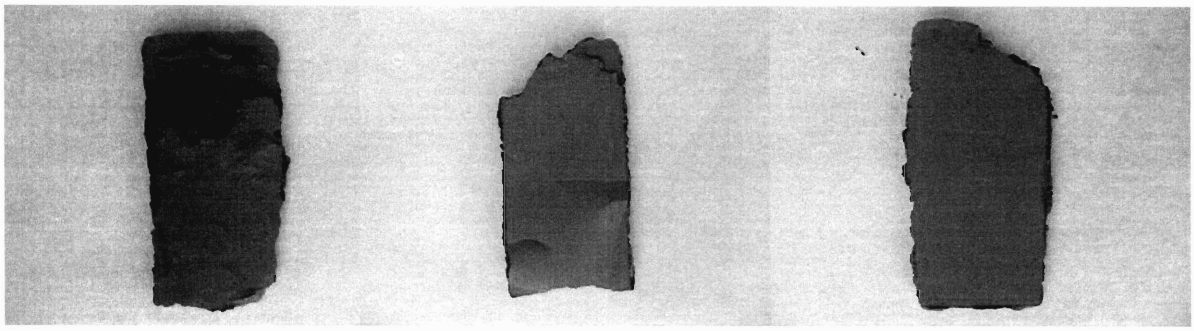

(a) (b) (c)

Figs. 5.12a-c: As-fired B8NS (a), B8SS (b), and B8LS (c) specimens.

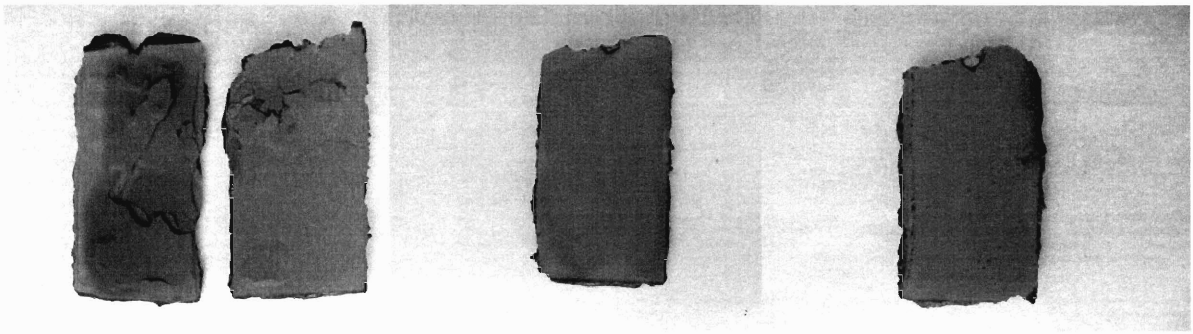

(a) (b) (c)

Figs. 5.13a-c: As-fired B18NS (a), B18SS (b), and B18LS (c) specimens.

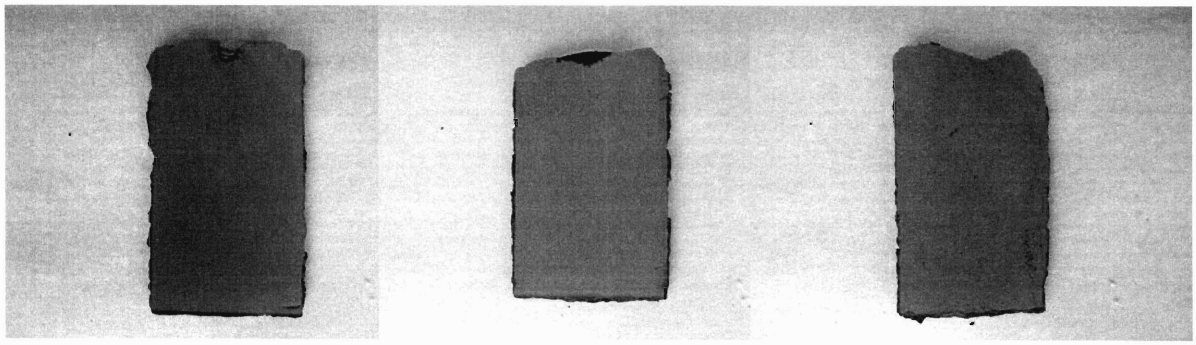

(a) (b) (c)

Figs. 5.14a-c: As-fired B28NS (a), B28SS (b), and B28LS (c) specimens.

NOTE: In Figs. 5.12-5.14, only W surfaces are shown.

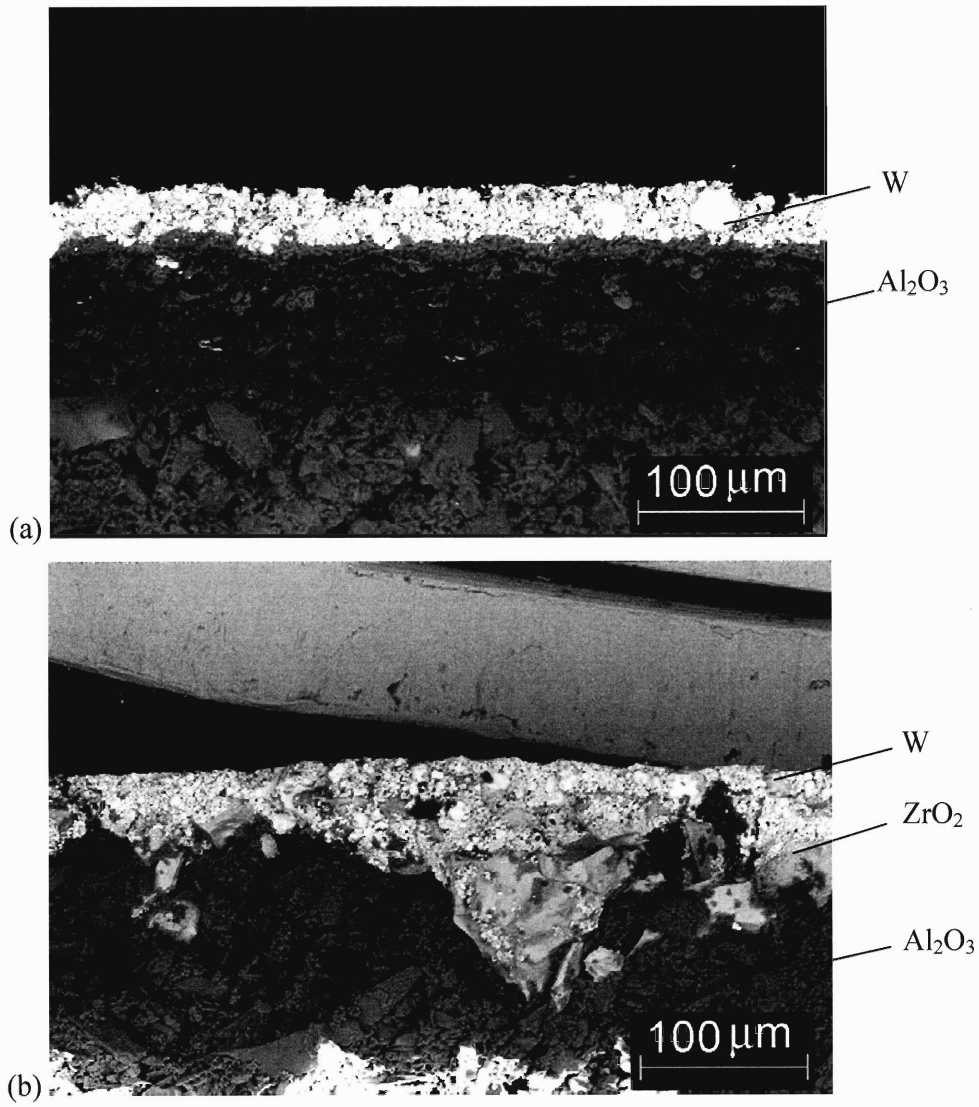

Figs. 5.15a-b: SEM micrographs showing a cross section of as-dewaxed (a) B18NS and (b) B18SS specimens.

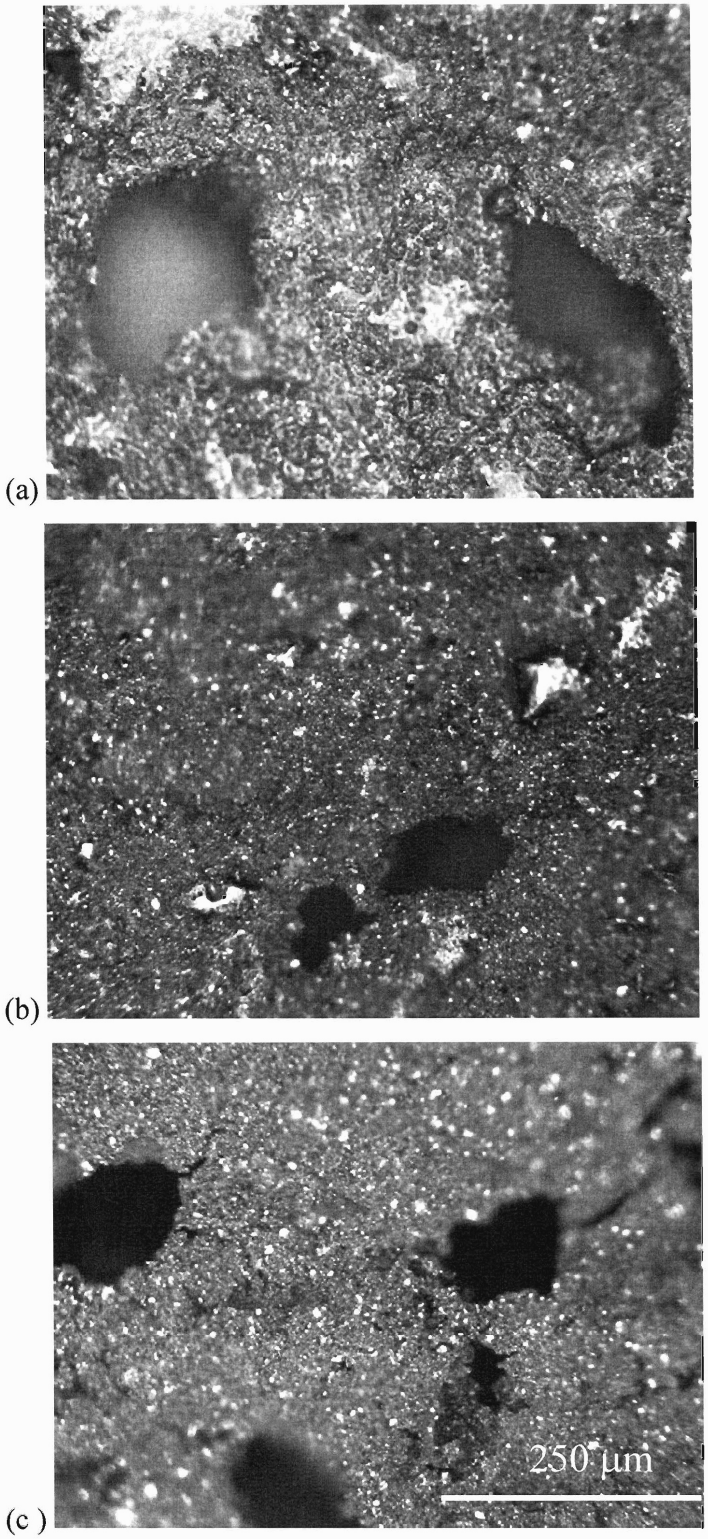

Figs. 5.16a-c: Optical micrographs showing the morphology of the W surface from (a) as-dewaxed, (b) as-baked, and (c) as-fired B28LS specimens.

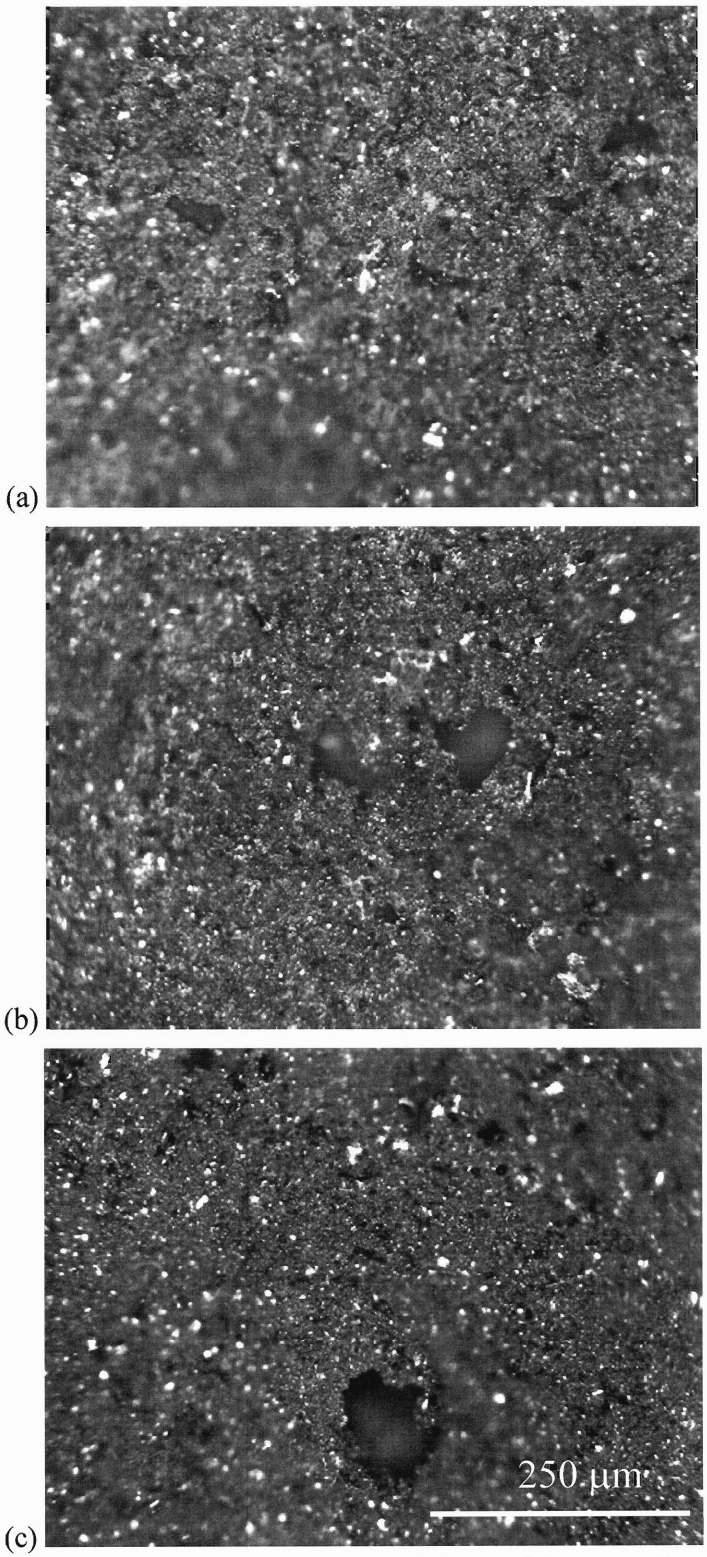

Figs. 5.17a-c: Optical micrographs showing the morphology of the W surface from (a) as-dewaxed, (b) as-baked, and (c) as-fired B28SS specimens.

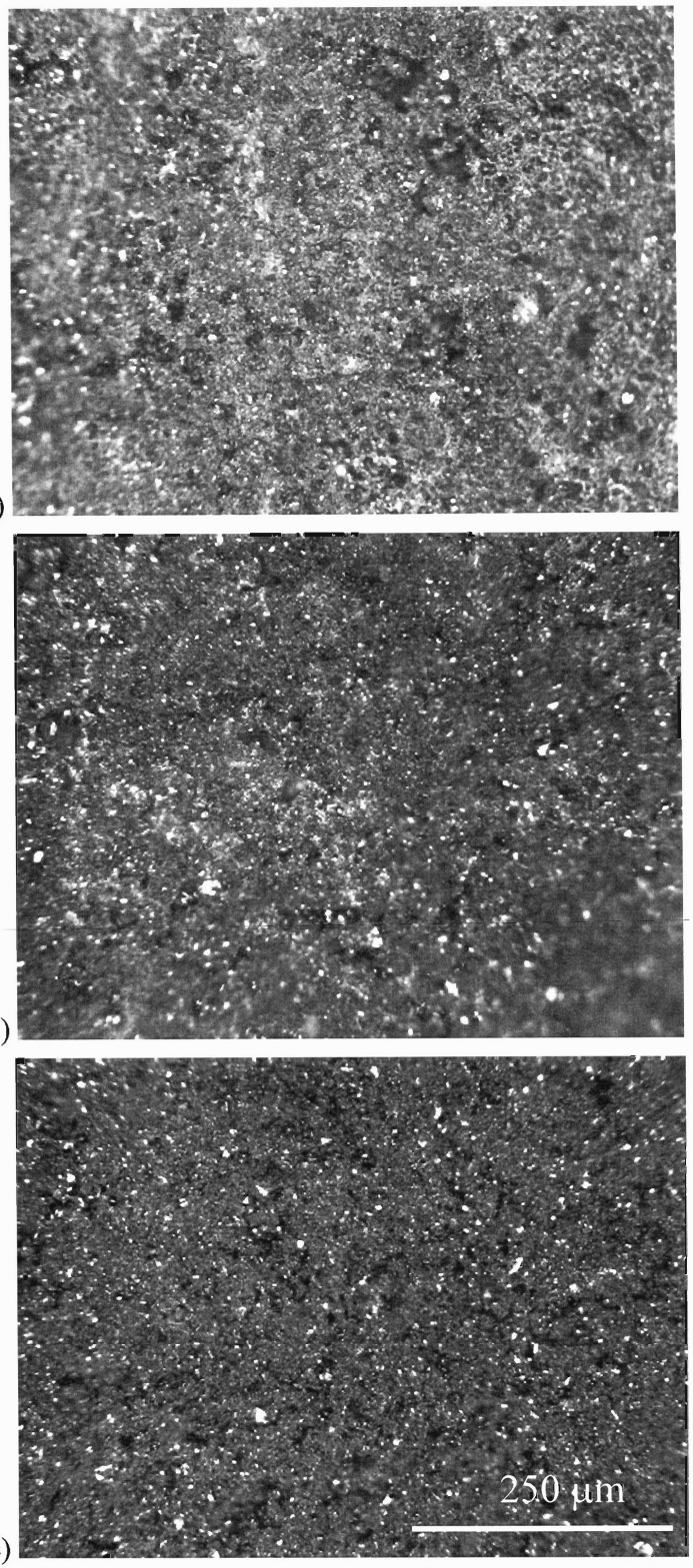

Figs. 5.18a-c: Optical micrographs showing the morphology of the W surface from (a) as-dewaxed, (b) as-baked, and (c) as-fired B28NS specimens.

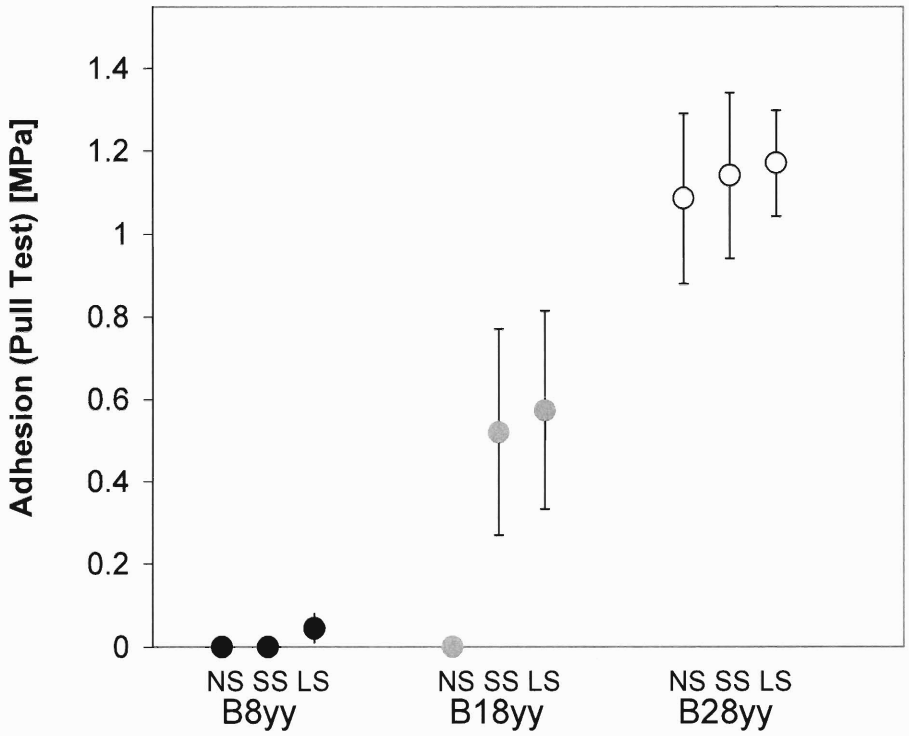

Fig. 5.19: The stress at failure of as-fired B8yy, B18yy, and B28yy specimens, all dried in the wet drying condition, as assessed by the tensile pull test.

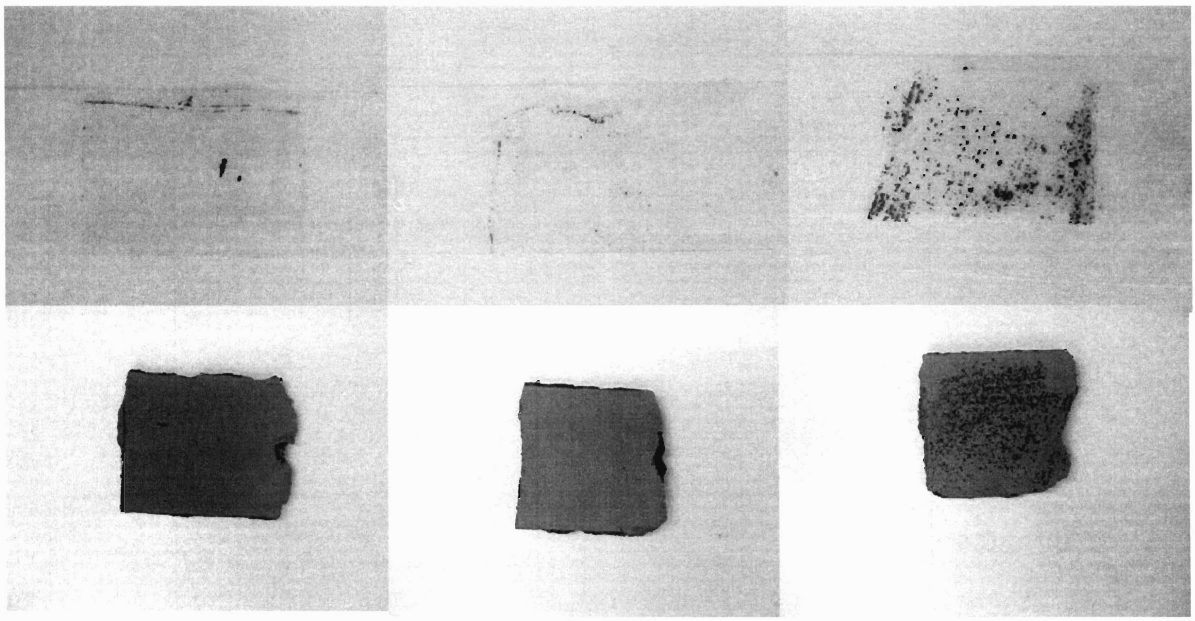

(a) (b) (c)

Figs. 5.20a-c: The results from the adhesive peel test performed on as-fired (a) B28NS, (b) B28SS, and (c) B28LS specimens. The top row presents adhesive tapes, which had been removed from W surfaces of the W/Al_2O_3 co-fired specimens. Tungsten particles can be observed on the tapes, especially in (c). The appearances of the W layer of the specimens after the test are shown in the bottom row.

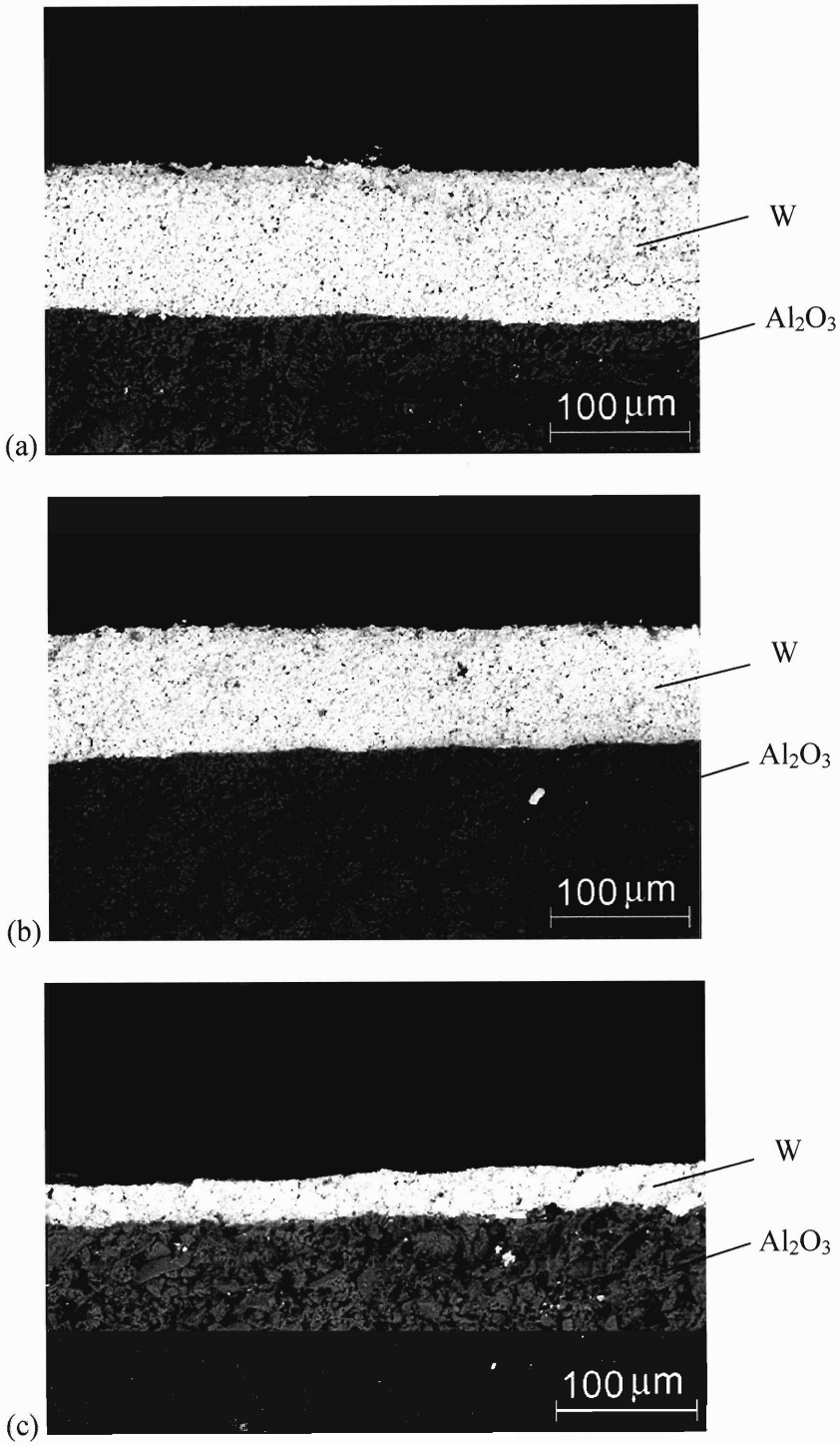

Fig. 5.21a-c: SEM micrographs showing a cross section of as-fired (a) B28NS-A1, (b) B28NS-A2, and (c) B28NS specimens.

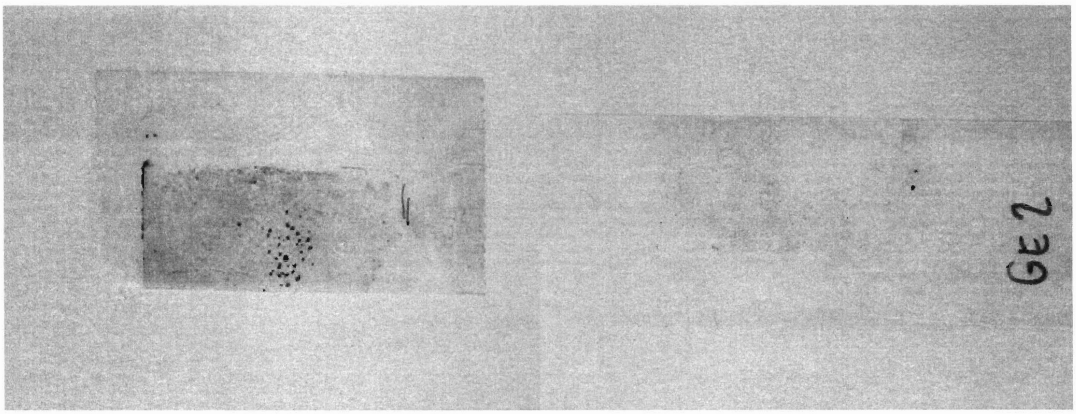

(a) (b)

Figs. 5.22a-b: Adhesive peel test results of specimens prepared with series A tungsten powder (a) and series A powder with 0.05% Ni addition (b). Notice the very dusty tape in (a); this is the characteristic of a poorly sintered W layer, which is very different from what is observed in the case of B28LS (Fig. 5.20c) where many of spotty W agglomerates were observed on a rather clear tape.

Chapter VI. Bonding Strategies of W and Al_2O_3 at Low Temperatures

6.1 Introduction

As mentioned in the earlier chapters, the adhesion of co-fired materials that are joined primarily through mechanical interlocking of sintered particles is relatively weak. To enhance the bonding, the materials may be chemically-joined with techniques that involve the use of chemical additives to induce the development of a third phase along the joining interface. For brazing and microelectronic packaging applications, for example, a metallization process (i.e., a process where a thin layer of W paint is applied on the ceramic and co-fired) usually involves the migration of liquid phase along the joining interface of the materials [140, 141]. As the performance of co-fired composites relies on the bond quality between joined materials, development of bonding techniques that can provide strong seals has been a subject of investigation for several decades.

Bonding of metal and ceramic through the metallization process was first developed in 1936 by a German scientist, Pulfrich, who painted layers of Mo, Rh, or W powder onto a non-porous steatite ($Mg_3Si_4O_{10}(OH)_2$) surface and then co-fired the materials in a reducing atmosphere [76]. The joining of W metallization layers to Al_2O_3 substrates was later investigated by Chance in 1970 [84]. As described earlier, for his material system, bonding was controlled by mechanical interlocking of sintered particles along the joined interface; the resulting bond strength is relatively low, and may not be adequate for some applications. For this reason, various joining techniques that involve the use of chemical additives have been developed to improve the adhesion of co-fired W/Al_2O_3, including the so-called 'Mo-Mn process' [142-144] and the glass migration process [78-80]. These two most widely-adopted techniques rely on the formation and migration of liquid phases at high temperatures, and joints produced by these methods have proven superior to those formed via pure interlocking of sintered particles [77, 83, 84]. Descriptions of these conventional bonding techniques are provided in the subsequent section.

While it has been found that the established joining strategies for W and Al_2O_3 are feasible when processing is carried out at high temperatures, near or above 1500°C [80, 145], investigation of joining strategies at low processing temperatures (<1200 °C) is very limited. In this chapter, several strategies for bonding W and Al_2O_3 will be examined at low firing

temperatures, including conventional joining processes, as well as a class of new techniques concerned with the use of a low melting point ceramic additive, particularly Na_2SiO_3, that forms a transient liquid phase; joining and mechanical testing will be performed on W/Al_2O_3 co-sintered compacts. The work conducted in this chapter is intended as an illustration of chemical joining techniques and a simple feasibility study of their use at low temperature. It is an extension of the main body of the thesis, and intended as a first brushstroke on a major area for future work.

6.2 Descriptions of strategies for bonding W and Al_2O_3

a. The Mo-Mn Process

This bonding process was first developed in 1950 by Nolte and Spurek, two scientists at General Electric [143, 144]. In their invention, Mn was added into Mo paint to improve the bonding between Mo metallizaing layer and a ceramic substrate. The process was later extended to W, but the name 'Mo-Mn process' was still maintained. The Mo-Mn process generally involves the addition of Mn into W slurry with a W:Mn weight ratio of 4:1. In the presence of a wet atmosphere during firing, Mn in the W layer can oxidize to form MnO, which can react with the Al_2O_3 substrate, resulting in manganese aluminate spinel ($MnAl_2O_4$) at or near the interface, at temperatures as low as 1250°C. When fired at higher temperature, the spinel compound liquefies, and can migrate to fill voids in the W and Al_2O_3 layer, due to capillary action. The liquid solidifies upon cooling and the resulting void-free network along the interface leads to the improvement of mechanical and chemical interactions of the bonded materials. Depending on the composition of Al_2O_3, the Mo-Mn process has been executed successfully within the temperature range of 1400-1700°C [83, 142, 146, 147].

b. The Glass-Migration Process

In the early 1960s, a new bonding technique for a metallic layer and a ceramic substrate was developed, involving the use of ceramic additives such as MgO, CaO and SiO_2 in Al_2O_3, and soon became a standard method in metallization. By adding ceramic additives to Al_2O_3, chemical interactions occur upon firing, and this can lead to the formation of a glass phase whose melting point is lower than that of any of the mixed materials. This glass phase can liquefy and

migrate from the Al_2O_3 substrate into the porous W interstices due to the capillary pressure difference between the two porous layers [77, 78]. Total wetting of the W by the glass phase is possible and may result in retardation of W sintering. However, upon cooling, the glassy phase mechanically interlocks the metal and ceramic grains, and may also chemically interact with the metal resulting in an intermediate phase which provides bonding between glass and metal [148]. Mn addition may also be employed with the glass-migration technique. If Mn is present in the metallizing paint, MnO will be induced in the wet atmosphere and the oxide can act as a flux for the intergranular glassy phase and hence help accelerate the permeation of the liquid [83, 142]. Examples of ceramic systems for the glass migration process are 94.1%Al_2O_3-2.6%SiO_2-2.2%CaO [79] and 96.3%Al_2O_3-2.8%SiO_2-0.9%MgO [77], and such systems are typically processed at temperatures above 1500°C in a wet atmosphere.

The glass-migration technique was shown to give satisfactory metal/ceramic seals and proved superior to the Mo-Mn technique. Cole and Sommer studied the glass-migration mechanism and the strength of Mo/Al_2O_3 seals [83]. The authors observed that with a firing temperature of 1700 °C, the tensile strength of the seals of the specimens with high additive content (94% Al_2O_3) is higher than for purer Al_2O_3 specimens (99% Al_2O_3) with 20%Mn addition in the Mo paint (66.2 and 20.0 MPa, respectively). A similar observation has been reported by Varadi and Dominguez [81]. They measured the tensile bond strength in samples of pure W and 94% Al_2O_3, sintered at 1600°C, to be 85.86 MPa which they claimed to be greater than that obtained from the Mo-Mn process. When Mn and glass phase were used concurrently, Cole and Sommer found a slight decrease in the seal strength (64.8 MPa).

Various parameters control the process of glass migration. In general, glass migration is favored by a high metallizing temperature, and the use of a reducing atmosphere with high dew point [149, 150]. When the pores in the glass-filled Al_2O_3 side are bigger than those in the metallizing layer, a capillary flow of the glass is facilitated, resulting in strong bonding [78, 79].

c. Bonding with Na_2SiO_3

The motivation for the use of Na_2SiO_3 in bonding W and Al_2O_3 is similar to that for the glass migration process. With its very low melting temperature (1089° C), Na_2SiO_3 offers flexibility with regard to low temperature processing, liquefaction and migration. However, unlike traditional glass migration processes, Na_2SiO_3 also may react with solid Al_2O_3 particles to

form higher melting temperature compounds during firing [151]; this system offers the potential for a *transient* migration phase that solidifies after migrating, and remains stable at (and potentially above) the processing temperature. The use of Na_2SiO_3 particles as an interlayer material to bond W and Al_2O_3 will be examined in this work.

6.3 Experiment

The feasibility of the various strategies for bonding W and Al_2O_3 at low firing temperatures (below 1200°C) will be investigated here. The compositions of the materials used to prepare the test specimens are listed in Table 6.1; each 'set' of materials corresponds to a number of nominally identical specimens produced with the same starting materials. For example, set G represents a system of commercial purity W (2 μm average diameter, 0.02 wt.% Ni, and 0.04% wt.% Fe) and Al_2O_3 (4 μm), whereas in set H, the W powders were dry mixed with Mn (<45 μm). In set I, various contents of SiO_2 (<45 μm), MgO (<45 μm) and CaO (<10 μm) were mixed with Al_2O_3 powders.

To prepare two-layer joining specimens, the pre-mixed W and Al_2O_3 powders were sequentially loaded into a die of rectangular cross-section and cold pressed at 150 MPa. These green specimens were co-fired in a furnace with a heating rate of 5°C/min and an isothermal hold at 1177°C for one hour, followed by slow furnace cooling. To prevent the oxidation of W, the processing was carried out in a dry 3%H_2-97%N_2 atmosphere, except in the case of specimens from set H, which were fired in a wet atmosphere with 30°C dew point, which is typical for the 'Mo-Mn process', which relies upon atmospheric oxygen to form MnO. The geometry of each fired specimen was W8.3 x L24.7 x H5.2 mm (H_W = 4.5 mm; H_{Al2O3} = 0.7 mm). The general appearance of the test specimens was similar to those bi-layer specimens prepared for the study discussed in Ch. IV (Fig. 4.2a).

In addition to the conventional joining processes examined in sets G, H, and I, new joining techniques which involve the use of Na_2SiO_3 were investigated in set J. For set J-1, the specimens were composed of pure W and pure Al_2O_3, with the addition of Na_2SiO_3 granular powders (300 μm) that were spread uniformly along the metal/ceramic interface during the cold pressing step. Relatively large Na_2SiO_3 particles were employed to slow the potential solid state reaction between Na_2SiO_3 and Al_2O_3 upon heating [151], and to promote liquefaction of Na_2SiO_3

prior to reaction. Set J-2 is similar to J-1, except that a new interlayer was introduced between the W and Al_2O_3 layers. This interlayer was composed of dry-mixed powders, 85%W+15%Al_2O_3 by weight. Furthermore, along the interface between the interlayer (W+Al_2O_3) and Al_2O_3 layer, Na_2SiO_3 particles (300 μm) were applied.

Interfacial strength was evaluated for five specimens from each set, using the four-point bending delamination test already presented in Ch. IV [96]. To prepare the specimens for the test, each specimen was pre-notched at the middle of the sample in the porous Al_2O_3 layer, using a razor blade. The tests were carried out in a universal testing machine with a crosshead speed of 50 μm/min. Microstructural characterization was conducted using scanning electron microscopy (SEM), and energy dispersive spectroscopy (EDS) was employed to characterize the specimens' chemical composition.

6.4 Results and Discussion

After the sintering cycle, all specimens were intact and no macroscopic interfacial cracks were present. Through-cracking of the W layer with and without an initiation of interfacial delamination were observed when the four-point bending delamination test was performed on different sets of specimens. For those with interfacial delamination, the same characteristics of force-displacement curves as obtained from the test performed in Ch. IV were observed. A summary of the delamination test results for the specimens is presented in Fig. 6.1, represented by the force at failure. This measure is presented because the specimens all have identical geometry (no size normalization is required), and because it allows direct comparison of the net specimen 'strength' even when different mechanisms of failure occur. For example, in Fig. 6.1 the white columns represent failure by interfacial delamination, while the filled columns correspond to a through-crack failure in the W substrate, without interfacial delamination. In the latter cases, the reported values represent lower bounds on the interfacial delamination strength.

In the following sections, each of the specimens is discussed in turn, linking the strength measurements above with microstructural observations and thermodynamic discussion of the system.

i. W/Al_2O_3 (set G)

Specimens of this set are the baseline for low-temperature co-sintering of the W-Al_2O_3 system, without any joining additives. Similar to what observed in the study performed in Ch. IV, the W and Al_2O_3 layers of these specimens were partially sintered and bonded to one another through pure mechanical interlocking of sintered particles (see Fig. 4.2b). The results reported in Fig. 6.1 show that interfacial delamination occurred in the specimens of set G with an average force of 338 N.

ii. $W+Mn/Al_2O_3$ (set H)

The addition of Mn in set H specimens led to significant changes in the specimen quality after firing. There was no evidence for the formation of a liquid phase at the interface, as would typically be seen in the Mo-Mn process when it is conducted at temperatures above 1500° C. This result is readily rationalized based on the system thermodynamics, because the eutectic temperature of the MnO-Al_2O_3 system is 1520° C [151], and our firing temperature of 1177° C is too low to result in a liquid phase.

The Mn addition also led to a clear change in the failure mode of the test specimens; the data in Fig. 6.1 indicate through-crack failure of the W substrates prior to interfacial delamination. This implies that independently of changes in the interfacial strength, Mn addition substantially weakened the W layer. This is most likely due to the use of a wet atmosphere, which leads to the formation of $WO_2(OH)_2$ at the firing temperature, and which can slow sintering [9, 149].

Clearly, the traditional Mo-Mn process offers no benefit for joining W and Al_2O_3 at low temperatures, and in fact degrades the sintered strength of the W layer as well. This result underscores the need for new joining processes for lower temperature bonding of W and Al_2O_3.

iii. Glass Additions in the Al_2O_3 Layer (set I)

As described earlier, for these specimens various ceramic additives were incorporated into the alumina layer, on the expectation that they would form a vitreous glass that could penetrate the W layer and create a sound mechanical bond. In this section we explore two different compositions of glass-forming additives from sets I-1 and I-2, to identify the conditions required for glass migration bonding at low temperatures.

In the case of the I-1 specimens, the Al_2O_3 layer was doped with small amounts of SiO_2, MgO, and CaO, in the proportions given in Table 6.1. Fig. 6.2 depicts the microstructure of these specimens, where it appears to be a glass migration layer, with a depth of approximately 100 μm below the interface. It can be expected that the glass migration layer would give rise to strong adhesion of W and Al_2O_3; the results from the bending delamination test (Fig. 6.1) suggest a relatively high interfacial toughness of the I-1 specimens, as failure occurred via a body crack prior to interfacial delamination, at a very high applied load.

For a glass migration process, the composition of the glass additives must be carefully chosen to match the temperature of the process. As a control experiment to illustrate this point, we examined the H-2 composition, which is comparable to H-1 in terms of the weight ratio of different ceramic powders, but here only MgO and CaO (and not SiO_2) powders were mixed with Al_2O_3. According to the Al_2O_3-MgO-CaO ternary phase diagram [151], no liquid phase should be present in the ceramic of this composition processed at 1177° C, and so unlike the silica-containing (H-1) system described above, glass migration was not expected in this case. The absence of a glass migration layer was confirmed when a cross-sectional SEM micrograph of the specimen was examined (Fig. 6.3). When subject to the bending test, these specimens failed through delamination at a relatively low load, below the baseline value achieved by co-sintering W and Al_2O_3 without additives (Fig. 6.1).

These experiments demonstrate that the conventional glass migration technique has promise for lower-temperature joining in the W-Al_2O_3 system, provided that the additive composition is carefully chosen and controlled. For the specific cases examined, it would appear that some SiO_2 addition is required to induce glass migration at low processing temperatures.

iv. Application of Na_2SiO_3 (set J)

Fig. 6.4 shows in cross-section the microstructure of a typical J-1 specimen which has Na_2SiO_3 particles applied along the W/Al_2O_3 interface. A uniform glass migration layer can be observed clearly below the Al_2O_3 layer. This indicates that the migrating glass has good wetting characteristics when interfaced with W and Al_2O_3. In addition to the glass migration layer, large pores are present at the places where the Na_2SiO_3 particles (300 μm diameter) were originally located along the interface. When the bend test was performed on J-1 specimens, no delamination occurred and failure instead occurred at high loads via through-cracks (Fig. 6.1).

As described above, J-2 specimens also employed additions of Na_2SiO_3, but additionally involved an interlayer composed of both Al_2O_3 and W. In these specimens, the liquefied Na_2SiO_3 migrates through this interlayer, reacting with Al_2O_3 as it does so. Fig. 6.5 shows a cross sectional SEM micrograph of a typical J-2 specimen. Four distinct regions can be observed, including (from the top down) the Al_2O_3 layer, a glass migration layer, the W+Al_2O_3 interlayer, and the W layer. The glass migration layer has a thickness of about 200 μm, and occupies a region of the specimen which was originally part of the mixed W+Al_2O_3 interlayer.

EDS composition maps of the J-2 specimen in the region of glass migration are shown in Fig. 6.6. These results indicate that Al_2O_3 particles in this region were partially dissolved into the migrating Na_2SiO_3 phase, which formed a dense and contiguous matrix around the particles of the interlayer. The composition of this migrated matrix phase was examined with EDS, and it was found that the average Al_2O_3-to-$Na_2O.SiO_2$ ratio of the glass was about 5:4 (atomic fraction). According to the ternary phase diagram of the Na_2O-Al_2O_3-SiO_2 system [151], this global composition could constitute a glass with a melting point above 1600° C. This result highlights the potential value of Na_2SiO_3 as a transient liquid former; although it liquefies, migrates, and promotes interlocking and bonding during low temperature firing, it also simultaneously reacts with Al_2O_3 to form a stable solid compound. Given an optimum interlayer geometry and processing history, it is expected that joints formed by this 'transient liquid phase co-sintering' method may retain appreciable strength even in service above the processing temperature.

As was seen for the J-1 specimens, delamination did not occur when the bend test was performed on the J-2 specimens. This indicates successful strengthening of the interfacial regions through the use of Na_2SiO_3. In this case the body strength of the system is rather low as compared to specimens from set J-1, and this is attributed to the relatively large 'unused' interlayer that was not infiltrated with glass during firing (Fig. 6.5). In an optimized system, the W+Al_2O_3 interlayer would be fully infiltrated with the migrating glass phase, improving the body strength of the system.

6.5 Conclusion

Several strategies for bonding W and Al_2O_3 through co-sintering have been explored, including two conventional techniques (the Mo-Mn process and the conventional glass migration process) and a new transient liquid phase technique based on Na_2SiO_3, and the focus has been on the feasibility of these techniques at low processing temperatures (below 1200° C). The Mo-Mn technique was found unsuitable for low-temperature joining, while glass migration processes can be adapted for low temperature use if the additive composition is carefully controlled. The new transient liquid phase co-sintering technique presents a rather simple low-temperature process involving only a single additive, and is shown to produce sound joints that resist delamination.

Table 6.1: Ceramic and metal compositions of various specimen sets.

Specimen Sets	Ceramic Composition [wt.%]				Metal Composition [wt.%]		Interlayers
	Al_2O_3	SiO_2	MgO	CaO	W	Mn	
G	100	-	-	-	100	-	-
H	100	-	-	-	95	5	-
I-1	94	4.5	1	0.5	100	-	-
I-2	98.43	-	1.05	0.52	100	-	-
J-1	100	-	-	-	100	-	Na_2SiO_3
J-2	100	-	-	-	100	-	Na_2SiO_3, 85W+15Al_2O_3

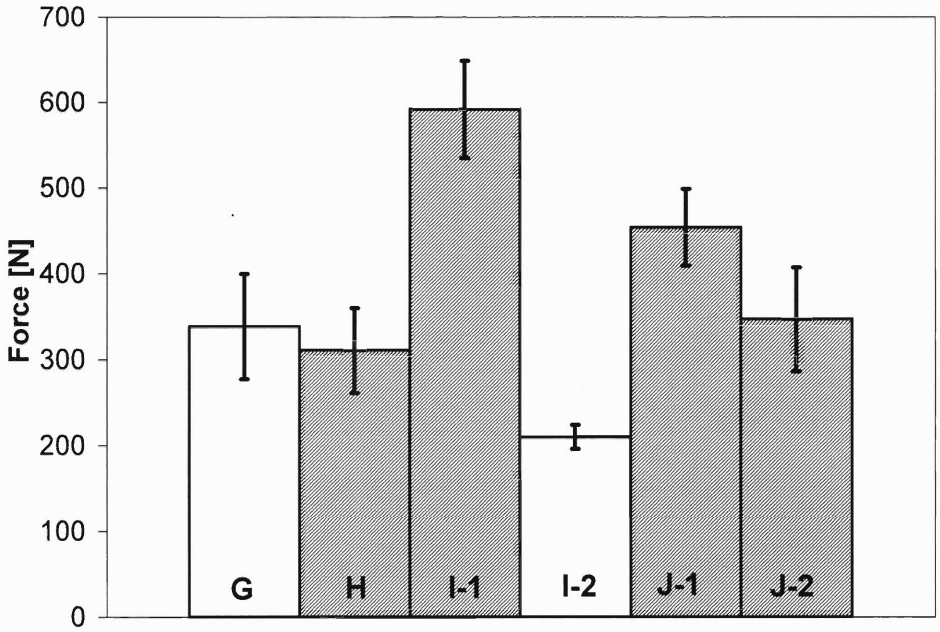

Fig. 6.1: The interfacial strength (white) or the body strength (filled) of the W layer as measured by four-point bending test on the W/Al_2O_3 specimens. The compositions of the different specimens are described in Table 6.1.

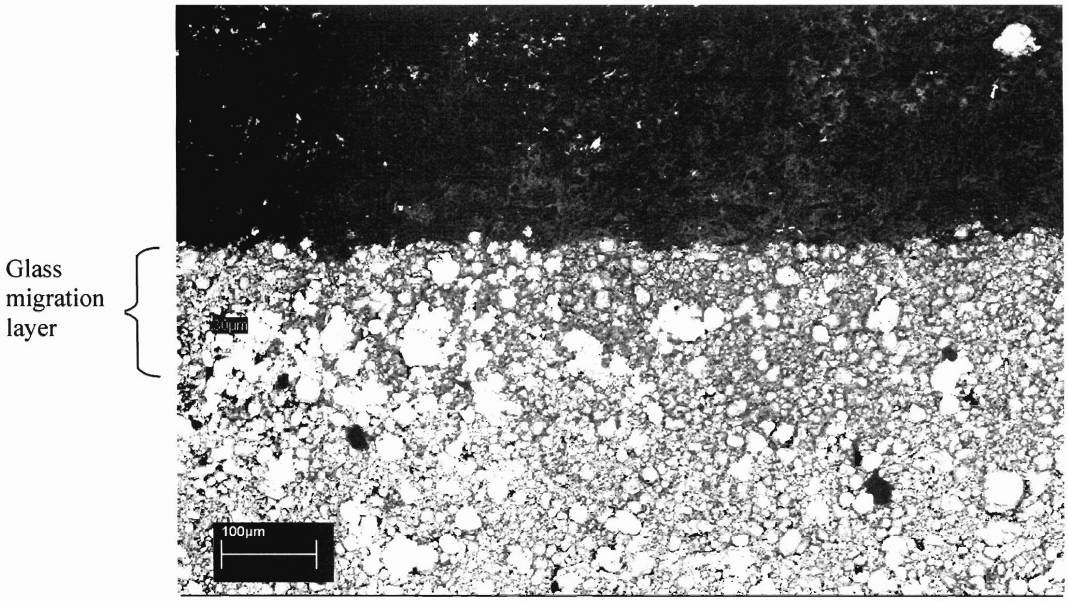

Fig. 6.2: A cross section of specimen I-1 (W(bottom)/94Al_2O_3-4.5SiO_2-1MgO-0.5CaO (top)). A glass migration layer with approximate thickness of 100 μm is present below the interface.

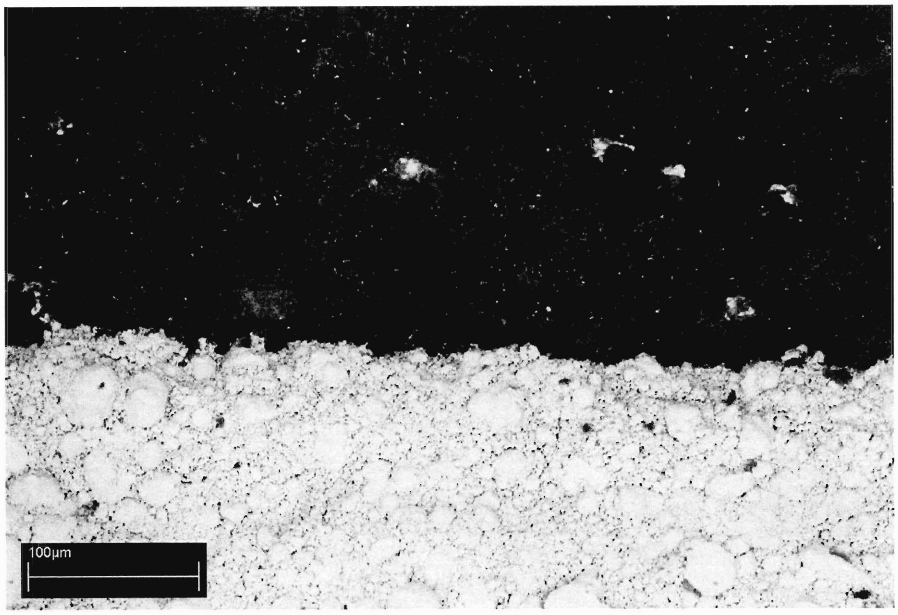

Fig. 6.3: A cross section of specimen I-2 (W(bottom)/98.43Al_2O_3-1.05MgO-0.52CaO (top)). No glass migration layer is present in this case.

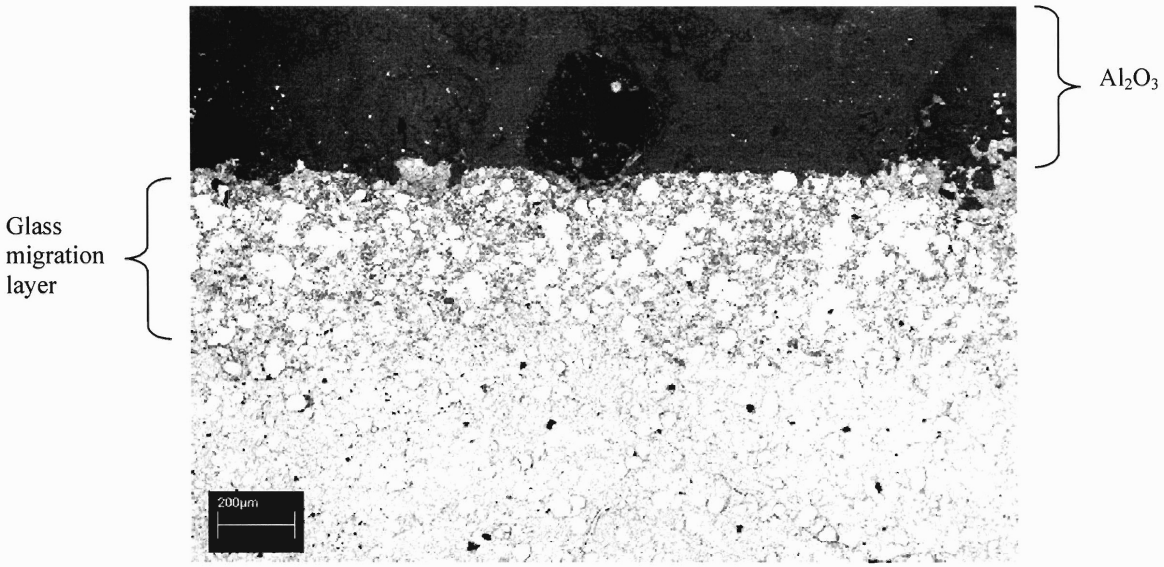

Fig. 6.4: A cross section of specimen J-1 ($W/Na_2SiO_3/Al_2O_3$). A glass migration layer approximately 200 µm deep can be observed below the interface, as can large voids above the interface where Na_2SiO_3 particles once sat.

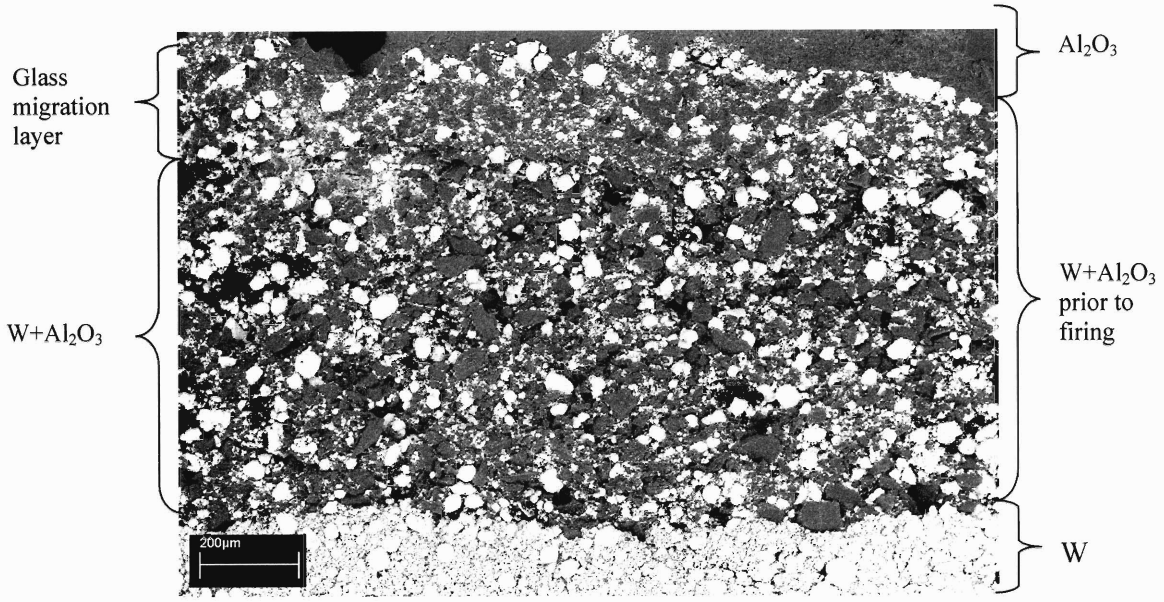

Fig. 6.5: A cross section of specimen J-2 ($W/W+Al_2O_3/Na_2SiO_3/Al_2O_3$). The structure is composed of four distinct layers—Al_2O_3 layer (top), the glass migration layer which is comprised of W, Al_2O_3, and an infiltrated glass, the interlayer of 85wt.% W (light particles) + 15wt.% Al_2O_3 (dark particles), and the W layer (bottom).

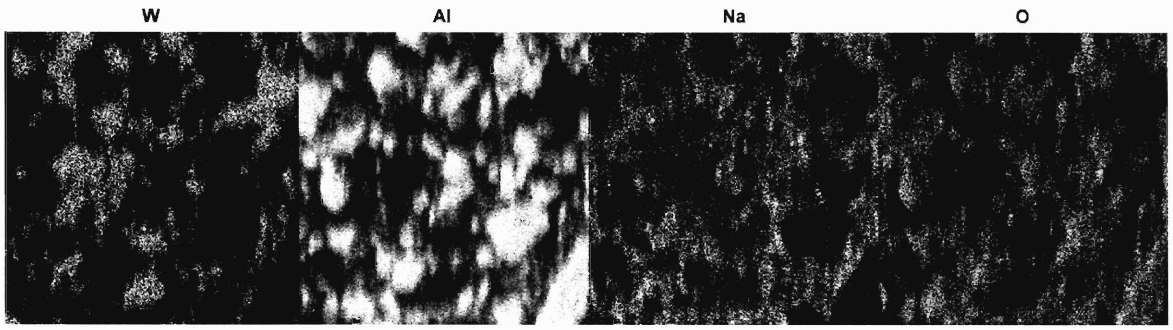

Fig. 6.6: The EDS composition maps of W, Al, Na, and O in the glass migration layer of specimen J-2 (see Fig. 6.5). The maps indicate that glass migration and dissolution of Al_2O_3 particles into the glass phase occur.

Chapter VII. Conclusions and Future Work

7.1 Conclusions

The production of sintered W typically requires temperatures much higher than 1500°C to attain high density, such as would be required in the case of W filaments. Similarly, it has been shown in past studies that co-fired W/Al_2O_3 can be fabricated at high temperatures near or above 1500°C with conventional bonding techniques. Since, in a variety of refractory applications, it is potentially useful or even necessary to produce W/Al_2O_3 composites at low firing temperatures (<1200°C), low-temperature processing techniques and a better understanding of mechanical properties of the materials produced at such emperatures need to be developed. In this thesis, a set of studies have been performed to gain fundamental understanding of how various processing parameters may influence the sintering of W and adhesion properties of low-temperature co-sintered W/Al_2O_3, as well as to investigate processing techniques that can be practically useful for joining W and Al_2O_3 at low firing temperatures. The major contributions of the thesis in this regard are summarized below:

1) For many years it has been known that W sinters very poorly at low firing temperatures, and activated sintering techniques for W were later developed to overcome this problem. The technique is however not yet widely adopted, and the study of mechanical response of materials processed by this technique was, until this thesis, notably lacking. Of particular interest to this thesis is the use of activated sintering techniques employing only a minimal additive content (below what is suggested as optimum) and processed at relatively low firing temperatures (<1200°C). The results obtained here indicate that the addition of Ni, Fe, or a combination of the two with a content in the range of sub-monolayer coverage to a few monolayers can already improve the sintering of W significantly. At the firing temperatures near or below 1200°C, the activated W with particle size on the order of 1 μm remains in the initial stage of sintering. Hardness and fracture toughness of partially sintered W were found to be critically dependent on the sintering behavior of W, which was in turn affected by the sintering additives. However, the relationship between mechanical response and sintered

density of the materials did not seem to be dependent on the type and content of additives used. The analysis performed in the study showed that both hardness and fracture toughness were controlled predominantly by the relative interparticle neck size of sintered particles. While fracture toughness could be described solely though the densification parameter, hardness appeared to scale with a factor that contained both sintered density and densification. It is anticipated that the understanding gained here could be used to explain the mechanical response of other partially-sintered materials.

2) Whereas the fabrication of co-sintered W/Al_2O_3 bilayer composites has conventionally been carried out at temperatures above 1500°C, this thesis presents the first effort to co-sinter these materials at low temperatures through the use of sintering activators. Not only did sintering additives help enhance the mechanical response of sintered W, but they also affected the adhesion of W/Al_2O_3 composites. Using a four-point bending delamination test and numerical analysis, it was observed that the interfacial adhesion could be affected by (i) the enhancement in sintering of the joined layers, and (ii) the degree of shrinkage mismatch, both of which varied with activator content. For the bending compact specimens used in the study, the adhesion (*practical adhesion*) was improved initially with an increasing additive content, due to the improved stiffness of the W layer. At higher additive content, a decrease of adhesion (*both practical and fundamental adhesion*) was observed, and was attributed to the loss of some mechanical interlocks at the interface owing to the higher degree of shrinkage mismatch. To maximize adhesion of the co-sintered bilayer, therefore, both the densification-related properties of the individual layers and the sintering mismatch need to be well controlled.

3) Partially-sintered W/Al_2O_3 composites are potentially useful for a variety of applications, including investment casting shells, which are fabricated through a slurry-based route. Unlike simple dry pressing, many more processing parameters are involved in slurry-based production of W/Al_2O_3 composites, and this thesis presents the first comprehensive study of the influences of these parameters on sintering and adhesion properties of W/Al_2O_3 composites. The major conclusion of this work is that W/Al_2O_3 shells with acceptable sintering and adhesion properties can be produced at low firing

temperatures, provided that the binder system, the application of stucco sand, and powder characteristics are well controlled. In W/Al_2O_3 mold production, incipient defects and delamination sites can form as early as the slurry drying steps. The formation of drying cracks can be prevented by dipping a layer with minimal thickness and applying a uniform layer of stucco sands following dipping. The thickness of dipping layers in turn can be controlled by the characteristics of stucco sands in the previous layers as well as the slurry characteristics. Colloidal silica content in the Al_2O_3 layer silica binder was found not only to provide green strength to the dried, green Al_2O_3, but also improved both the sintering of Al_2O_3 and the adhesion of co-fired W/Al_2O_3 shells. Similarly, zirconia stucco sands applied along the W/Al_2O_3 joined interface also helped enhance adhesion. Pitting defects on the W surface were however generated when sands of too large a size were used. Without sand application, delamination-free W/Al_2O_3 shells with good sintering properties of individual layers could be produced when the materials contained 0.7 monolayer of Ni in the W layer, and 28wt.% colloidal silica binder in the Al_2O_3 layer.

4) Past studies have suggested that adhesion of co-fired materials can be further improved with the use of bonding techniques that induce migration of a liquified phase along the joined interface. In this thesis, the feasibility of several such bonding strategies were investigated in the relevant low range of processing temperatures for co-fired W/Al_2O_3. These strategies, which involved the use of chemical additives, included the conventional Mo-Mn and the glass migration processes, and a new transient migrating phase method involving the use of Na_2SiO_3 particles. While the Mo-Mn technique was found unsuitable for low-temperature joining, the glass migration processes could be adapted for low temperature use if the additive composition was carefully controlled. The use of Na_2SiO_3 resulted in a novel transient liquid phase bonding technique that provided a sound joint for co-sintered W/Al_2O_3, which could potentially be used in service at temperatures several hundred degrees higher than that used in processing, without deterioration of the joint.

The studies performed in this thesis therefore have illustrated that the production of co-fired W/Al_2O_3 at low firing temperature is generally feasible, and that both sintering properties of the individual joining layers and the characteristics of the interfaces affect the quality of the composites. Consequently, processing parameters associated with powder consolidation, sintering, and bonding strategies need to be tightly controlled for successful fabrication.

7.2 Future Work

The understanding gained from this comprehensive study has provided a framework, both fundamental and practical, upon which interesting future research may be performed. Additionally, some areas of study in this work that can benefit from further investigation have been identified. Some of these potential future studies are presented below.

- While it has been suggested that a minimal content of Ni as used for the W activated sintering process does not significantly affect the coefficient of thermal expansion (CTE) of W, it is unclear how the CTE of Al_2O_3 would be influenced by the addition of SiO_2 on the order of a few to ~10 weight percents. Investigation of the effects of SiO_2 on the CTE of Al_2O_3 and the interactions of the two materials would help explain the mechanical response of the W/Al_2O_3 shells containing SiO_2, as measured in the study.

- The bonding strategies discussed in Ch. VI could be further developed to achieve optimal strength in applications for which the techniques will be employed. Additionally, other candidate additive materials and processing techniques should be explored for improving the bonding of low-temperature co-fired materials. For slurry-route processing, the challenge for these bonding strategies would be to develop binder solutions that are compatible with host materials as well as additives.

- Testing methods for assessment of the interfacial strength of *thin brittle coating layers on substrates*, such as the scratch test or pull test, could be employed to

evaluate practical adhesion specific to some particular loading configurations. Additional testing techniques should be explored and developed in order to study interfacial fracture mechanics of such materials.

- Low-temperature processing is attractive for several reasons as discussed in this thesis. In addition to co-fired W/Al_2O_3 composites, it would be worthwhile to investigate low-temperature processing techniques for other co-fired refractory systems. Powder consolidation methods, sintering techniques, and bonding strategies of the joined materials need to be examined.

Appendices

Appendix A. Interfacial Fracture Mechanics

In a system of two linear elastic isotropic materials which are joined to one another, the near tip field of an interfacial crack between the two materials can be characterized through the complex stress intensity factor, which we can define as:

$$K = K_I + iK_{II} \tag{A-1}$$

The in-plane traction vector, σ, at distance λ ahead of the interfacial crack can then be described by [152]:

$$\sigma_{yy} + i\sigma_{xy} = \frac{(K_I + iK_{II})}{\sqrt{2\pi r}} \lambda^{i\varepsilon} \tag{A-2}$$

where ε is the bimaterial constant which is a function of β, the second Dundurs parameter [153]. These parameters are given by:

$$\varepsilon = \frac{1}{2\pi} \ln\left(\frac{1-\beta}{1+\beta}\right), \tag{A-3}$$

$$\beta = \frac{1}{2} \cdot \frac{\mu_1(1-2\nu_2) - \mu_2(1-2\nu_1)}{\mu_1(1-\nu_2) + \mu_2(1-\nu_1)} \tag{A-4}$$

In Eq. (A-4), μ and ν are the shear modulus and the Poisson's ratio, respectively. The subscripts 1 and 2 refer to materials 1 and 2.

The strain energy release rate, G, can be related to the stress intensity factor through [101, 154]:

$$G = \frac{1}{E^*} \cdot \frac{|K|^2}{\cosh^2(\pi\varepsilon)}, \text{ where} \tag{A-5}$$

$$|K|^2 = \bar{K} \cdot K = K_I^2 + K_{II}^2, \tag{A-6}$$

and E^* is the effective Young's modulus. For the plane strain condition, it is equal to:

$$E^* = \frac{2E_1E_2}{E_1(1-\nu_2^2) + E_2(1-\nu_1^2)} \tag{A-7}$$

In this equation, E_1 and E_2 are the Young's moduli of the two materials. Note that the Young's modulus, E_n, and the shear modulus, μ_n, are related to one another by (n=1or 2):

$$E_n = 2(1+\nu_n)\mu_n \tag{A-8}$$

The phase angle, ψ, which describes the relative proportion of shear to normal tractions at the characteristic distance, h, ahead of the crack tip, can be defined through the relation [109]:

$$Kh^{i\varepsilon} = |K|e^{i\psi}, \text{ or} \tag{A-9}$$

$$\psi = \tan^{-1}\left(\frac{\mathrm{Im}[Kh^{i\varepsilon}]}{\mathrm{Re}[Kh^{i\varepsilon}]}\right) \tag{A-10}$$

The specimen dimension or crack length can be employed for the characteristic distance, h [155]. Since it is known that the interfacial strength of materials can vary with phase angle [156], it is essential that phase angle is evaluated and reported with the value of strain energy release rate.

A contour integral method [157], a virtual crack extension procedure [158, 159], or a crack surface displacement method [109, 160] can be employed to determine G and ψ. In the crack surface displacement method, the relative plane-strain displacements of two points on the top and bottom crack surfaces (Δu_x and Δu_y in the x and y directions, respectively) are related to K by [109]:

$$\Delta u_y + i\Delta u_x = [\Delta u_x^2 + \Delta u_y^2]^{1/2} e^{i\phi} = \frac{2\left(\frac{(1-\upsilon_1)}{\mu_1} + \frac{(1-\upsilon_2)}{\mu_2}\right)\left(\frac{\lambda}{2\pi}\right)^{1/2} K\lambda^{i\varepsilon}}{(1+2i\varepsilon)\cosh(\pi\varepsilon)} \tag{A-11}$$

where ϕ is the angle of the surface displacement vector. With the use of Eq. (A-9) and modification of the denominator, Eq. (A-11) above becomes:

$$[\Delta u_x^2 + \Delta u_y^2]^{1/2} e^{i\phi} = \frac{2\left(\frac{(1-\upsilon_1)}{\mu_1} + \frac{(1-\upsilon_2)}{\mu_2}\right)\left(\frac{\lambda}{2\pi}\right)^{1/2} |K|}{(1+4\varepsilon^2)^{1/2}\cosh(\pi\varepsilon)} e^{i\varepsilon\ln(\lambda/h)} e^{-i\arctan(2\varepsilon)} e^{i\psi} \tag{A-12}$$

Using Eqs. (A-5), (A-7), and (A-8) in Eq. (A-12), the strain energy release rate, G, can be calculated as:

$$G = \frac{\pi(1+4\varepsilon^2)\cdot(\Delta u_x^2 + \Delta u_y^2)}{8\lambda\cdot\left[\frac{(1-\upsilon_1)}{\mu_1} + \frac{(1-\upsilon_2)}{\mu_2}\right]} \tag{A-13}$$

Finally, also from Eq. (A-12), the phase angle, ψ, can be determined as:

$$\psi = \tan^{-1}\left(\frac{\Delta u_x}{\Delta u_y}\right) - \varepsilon\ln\left(\frac{\lambda}{h}\right) + \tan^{-1}(2\varepsilon) \tag{A-14}$$

Appendix B.
Calculations of Sintering Parameters as Affected by Sintering Activators

As discussed in detail in Ch. III and Ch. IV, sintering activators, namely Ni and Fe, help enhance the sinterability of W. Depending on the additive content, the influence of sintering activators on sintering parameters and hence final mechanical properties of sintered products can vary. To design a fabrication process for sintered materials that would result in appropriate final material properties, it is therefore important that we understand the relationship between additive content and sintering parameters. In this section, a calculation procedure that determines how sintering parameters (including shrinkage and densification) for powders with a given particle size distribution vary with additive content is outlined. As an example, the discussion is presented in relation to series-A W powder containing Ni additives (See Ch. III for the characteristics of the powder). The relevant equations and calculations are described below.

It can be shown that the linear shrinkage (α) of sintered materials is related to sintered density (ρ_s) and green density (ρ_g) by:

$$\alpha = 1 - \sqrt[3]{\frac{\rho_g}{\rho_s}} \tag{B-1}$$

And by definition, the relationship between densification ($\tilde{\rho}$), sintered density, and green density is:

$$\tilde{\rho} = \frac{\rho_s - \rho_g}{1 - \rho_g} \tag{B-2}$$

From Eqs. (B-1) and (B-2), linear shrinkage may therefore be written as:

$$\alpha = 1 - \sqrt[3]{\frac{1}{1 + \tilde{\rho}(\frac{1}{\rho_g} - 1)}} \tag{B-3}$$

In Ch. III, we have shown that the relative interparticle neck size (r/R) of partially sintered W is related to densification by:

$$\left(\frac{r}{R}\right)^2 = 1 - (1 - \tilde{\rho})^{4/3} \approx 1.3\tilde{\rho} \text{ (for the initial stage)} \tag{B-4}$$

The interparticle neck size of sintered materials can also be described from a kinetic standpoint. Assuming volume diffusion as the dominant sintering mechanism for activated W, the expression for relative particle neck size is given by [3]:

$$\left(\frac{r}{R}\right)^2 = 4\cdot\left(\frac{A_o}{T\cdot r^3}\right)^{1/2}\cdot t^{1/2} = 4\cdot\left(\frac{A}{r^3}\right)^{1/2} \qquad \text{(B-5)}$$

where A_0 is a sintering parameter which relates to diffusivity, activation energy for sintering, surface energy, and atomic volume, t is time, and T is firing temperature. These parameters can be grouped into what we will term "A", *the activation parameter*. Combining Eqs. (B-4) and (B-5), the densification can be estimated as:

$$\tilde{\rho} \approx 3\cdot\left(\frac{A}{r^3}\right)^{1/2} \qquad \text{(B-6)}$$

Using Eq. (B-6), linear shrinkage in Eq. (B-3) may now be written as:

$$\alpha = 1 - \sqrt[3]{\frac{1}{1+3\cdot\left(\frac{A}{r^3}\right)^{1/2}\left(\frac{1}{\rho_g}-1\right)}} \qquad \text{(B-7)}$$

As shown in Ch. III, sintering activators reduce the activation energy for sintering of W. The activator parameter, A, in Eq. (7) will clearly be affected by additive content, resulting in the change of linear shrinkage. To determine A as a function of additive content for powder with a given particle size distribution, we can employ Eq. (B-8) below:

$$<\alpha> = \frac{\int(P(r)\cdot\alpha)dr}{\int P(r)dr} \qquad \text{(B-8)}$$

In Eq. (B-8), $<\alpha>$ is the average linear shrinkage, and P(r) is the number population of W powders at any particle size. $<\alpha>$ can be measured experimentally from the change in geometry of fired compact specimens, and the values of this parameter for series-A W powder which has been sintered at 1177°C for 1 hr. are presented in Table B-1. Also shown in Table B-1 are the values of the average monolayer coverage of Ni in series-A W powder, as determined by Eq. (3.1) (See Ch. III). P(r), on the other hand, can be obtained from particle size analysis, and the values of this parameter can be written in a polynomial form as shown in Eq. (B-9) for series-A powder.

$$P(r) = -480.95+3948.03\cdot(2r)-13574.19\cdot(2r)^2+25472.93\cdot(2r)^3-28126.79\cdot(2r)^4+18712.01\cdot(2r)^5$$
$$-7368.54\cdot(2r)^6+1581.38\cdot(2r)^7-142.52\cdot(2r)^8 \quad \text{(B-9)}$$

Using Eqs. (B-7) and (B-8) and all necessary parameters obtained experimentally, the activation parameter for series-A W powder was calculated, and the results are tabulated in Table B-1. The relationship between the average monolayer coverage of Ni appears to follow a function described by Eq. (B-10), and the result is also plotted in Fig. B-1.

$$A(M) = -4.65\cdot10^{-6}\cdot M^3 + 1.705\cdot10^{-4}\cdot M^2 + 1.4\cdot10^{-5}\cdot M + 2.4\cdot10^{-6} \quad \text{(B-10)}$$

Having obtained the values for the activation parameter, we can now determine the other sintering parameters of interest at different additive contents. For example, using A(M), linear shrinkage can be calculated from Eqs. (B-7) and (B-8). To estimate densification, the parameter which largely controls the mechanical properties of partially sintered W as described in Ch. III, Eq. (B-11) can be used:

$$<\tilde{\rho}>=\frac{\int(P(r)\cdot 3\cdot\left(\frac{A(M)}{r^3}\right)^{1/2})dr}{\int P(r)dr} \quad \text{(B-11)}$$

The calculated linear shrinkage and densification are shown in Fig. B-2 as a function of average monolayer coverage of Ni for series-A W powder.

Table B-1: The average monolayer coverage of Ni ($\overline{M}$), the *measured* percent linear shrinkage (%<α>), and the calculated activation parameter (A) for series-A W powder sintered at 1177°C for 1hr.

$\overline{M}$	%<α>	A [$\mu m^3 x10^{-5}$]
0	0.46	0.24
0.64	2.55	8
1.28	4.54	29
2.55	7.79	107

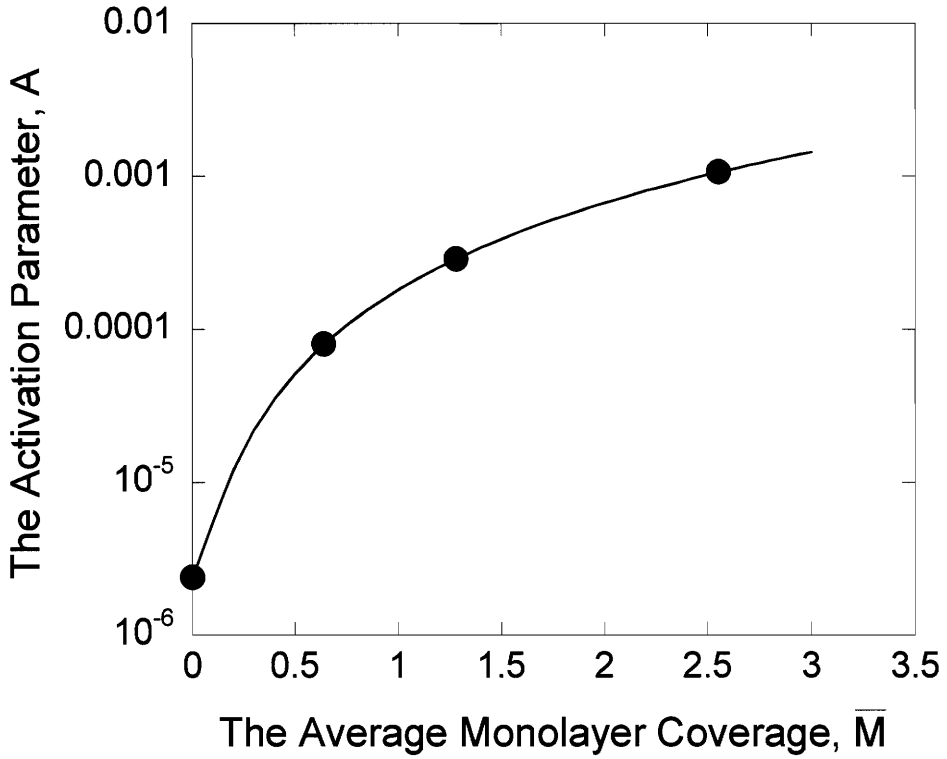

Fig. B-1: The activation parameter as a function of the average monolayer coverage of Ni for series-A W powder which has been sintered at 1177°C for 1hr.

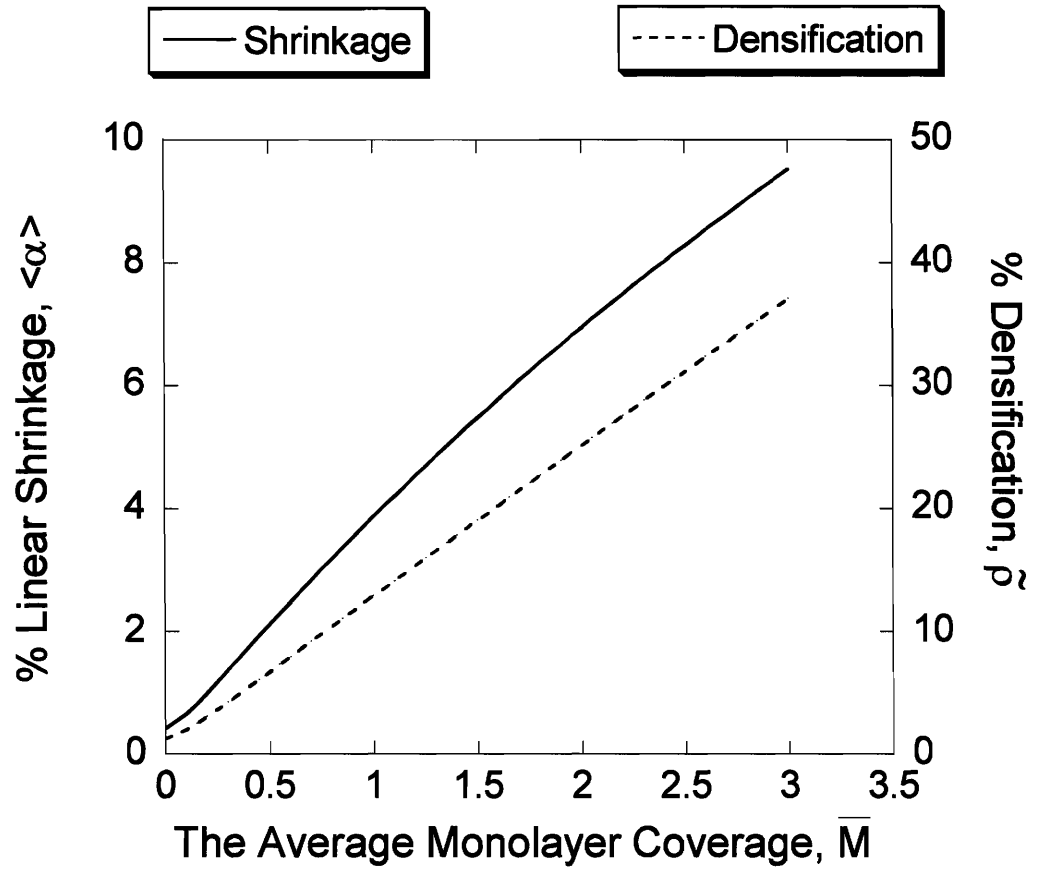

Fig. B-2: The *calculated* percent linear shrinkage and the calculated percent densification as a function of the average monolayer coverage of Ni for series-A W powder which has been sintered at 1177°C for 1hr.

Appendix C.
Comparison Study of Aqueous Binder Systems for Investment Casting[†]

I. Introduction

Organic solvents, such as alcohols, ketones, and hydrocarbons, are commonly used as liquid vehicles for powders in slurry-based processing, as they provide for relatively fast drying and exhibit good compatibility with other materials in the system [117, 118]. However, due to their toxicity and volatile nature, organic solvents usually pose environmental problems. A more environemtally-friendly solvent, namely water, is therefore desired. To effectively employ water-based slurries, it is important to develop binder systems (i.e., binders and additives) that are compatible with water and provide the desired properties to final products. In this study, we investigated the performance of various aqueous binder solutions in the process of mold production for investment casting, with specific focus on the influence of binders on the quality of pre-fired shells. While the study was solely performed on W/Al_2O_3 dip casting shells, it is anticipated that the understanding gained from the study can be extended to different materials systems and applications.

II. Experiment

a. Materials

Water-based W/Al_2O_3 shell specimens were prepared using the same lots of W (~1 μm) and Al_2O_3 (~4 μm) powders, and various types of binder systems in aqueous solvent. A 28wt.%-colloidal silica binder was employed for the Al_2O_3 dipping layer, while different kinds of binders were used for the W layer as described below:

- *Thermoplastic Starch*: The starch thermoplastic was created using inexpensive, readily available, and environmentally friendly components: 6.5 g starch, 200 mL of 1% glycerol solution, and 50 mg of NaCl. These elements were combined, and the solution was heated by a hot plate and continuously mixed until the boiling point of

[†] Acknowledgement: This study involved close collaboration with James LeBeau, a student in CMSE REU program, from Rensselaer Polytechnic Institute.

the solution (92°C) was reached. At the boiling point, the product was removed from the hot plate, covered, and allowed to cool for approximately 12 hours.

- *Latex*: A latex is a stable colloidal dispersion of polymeric sub-micron particles in an aqueous medium [119]. During drying of the solvent, these particles coalesce and form a polymeric network, providing green strength to a material. Two commercial latex binders were examined here: (i) Latrix 6300, a styrene-butadiene latex (Ondeo Nalco Company) and (ii) UCar DT211, an acrylic latex (Dow Chemical Company). De-ionized water was added to both latexes to achieve a composition of 50 wt.% as-received latex and 50wt.% water.

- *Polyvinyl Alcohol*: Polyvinyl Alcohol (PVA) is a thermoplastic polymer which is soluble in water, has good flexibility and a short drying time [119]. In this study, Evanol 52-22 L10, a partially hydrolyzed commercial PVA (DuPont Corp.) was used. De-ionized water was added to the as-received PVA giving a final binder solution composition of 50 wt.% PVA and 50 wt.% water.

- *Crosslinked PVA*: Because unmodified PVA is soluble in water once dried, the use of a crosslinking agent to prevent the dissolution of the binder in steam enviroment was examined (See section c. below). To provide the desired crosslinks, Tyzor LA (DuPont Corp.) was added to the mixture of PVA and water at room temperature. An optimum amount of Tyzor LA was found by testing samples of the mixture containing varying amounts of the crosslinking agent for water dissolution once dried. The final composition of the mixture selected for further testing, based on viscosity and solubility, contained 1.2 wt.% Tyzor LA, 49.4 wt.% PVA, and 49.4 wt.% water.

b. Specimen Preparation

Various sets of W slurries were prepared with different types of aqueous binder systems. The W solid loading content (%volume of W in a slurry) that resulted in good coating characteristics of W slurry on wax was individually determined for each binder system, and thus varied from one system to another. Slurry mixing and dipping processes were performed with

similar procedures as described in Ch. V. A small amount of a commercial wetting agent (Victawet) was used to adjust the wetting characteristics of the W slurry on wax, and for the case of Ucar-W slurry, a small amount of dispersant (Dexad) was also added. In most cases, CaO-partially stabilized zirconia stucco sands (300 μm) were applied between the 1st-dip (W) and 2nd-dip (Al_2O_3) coating layers. Al_2O_3 powder and colloidal silica binder (28% silica) were used to form a 2nd-dip slurry with binder-to-powder weight ratio of 0.27. The application of 2nd dip coat and dewaxing were performed after a drying duration of 1 and 2 days, respectively. All drying stages took place at a temperature of $23 \pm 2^{\circ}$ C and $54 \pm 7\%$ humidity. Dewaxing was conducted with a lab-scale autoclave with a 10 minute ramp and 3 minutes soak at 106° C and 40 psi.

c. Testing Methods

To successfully use water-based slurry in a multi-step dip casting process, several quality criteria need to be achieved. These include stability of the slurry, good wettability on wax and resistance to redissolution in water upon drying (a necessary condition for multiple dipping and autoclave operations). It is expected that these characteristics are largely controlled by the type of binders used in the aqueous slurry. A set of tests as listed below were employed to help identify the types of binders and slurry compositions that would meet such requirements, and to help gain a better understanding of what contributes to the quality of final dewaxed products.

- pH and viscosity measurements of W slurries
- Fallout-sedimentation and centrifuge-sedimentation for measuring settling time and packing fraction
- Coating of waxes for a qualitative assessment of wetting behaviors
- Dissolution of the W layer in water
- Surface and cross-sectional quality inspections after autoclaving

III. Results and Discussion

Table C-1 and Figs. C-1 and C-2 present the characteristics of W slurries prepared with various binder systems. These include solid loading, packing fraction of W powder in the slurry, viscosity, qualitative wetting quality on wax, water dissolution of W layer, slurry sedimentation trends, and acidity level. The characteristics of the W slurries and of dewaxed W/Al_2O_3 shells are discussed for each binder system below:

1) Starch: To achieve good flowability of the starch-W slurry, relatively low solid loading of W powder (20%) was used. Even at such low solid loading level, the viscosity of the slurry surpassed that of other systems. Additionally, the startch-W slurry exhibited a low powder fall-out rate (Fig. C-1). Such high viscosity and good slurry stability likely stem from the steric interaction of starch molecules with W powders. When the dissolution test was performed, whereby a wax coated with a dried W slurry layer was submerged in water for five minutes, it was observed that the W layer remained intact on the wax surface.

Figures C-3a and C-4a respectively show W surface quality and a cross section of as-dewaxed W/Al_2O_3 shells prepared with starch binder. As seen in Fig. C-3a, the quality of the W surface was rather poor in this case, with small pores distributed throughout. With high viscosity and low packing fraction of the W slurry, a relatively thick W layer was obtained (Fig. C-4a).

2) Latex:

2.1) Latrix6300: Slurry with good flowability could be produced at high solid loading (50%) using Latrix6300 binder. Following the addition of W powder into the binder solution, the pH of the slurry became rather neutral, unlike most systems which became somewhat acidic when W powders were added (Fig. C-2). The dissolution test showed that the W layer prepared with Latrix6300 was water-resistant. Following dewaxing, it could be observed that this binder system provided an excellent facecoat quality with a relatively thin W coating layer (Figs. C-3b and C-4b).

2.2) UCar DT211: W slurry with 55% solid loading was produced for this system. A rather neutral slurry and excellent water-proof quality of as-dried W layer were also observed in this system. Similar to the starch-W slurry, the present system was very stable (Fig. C-1). However, it also exhibited a significant shear thinning characteristic, which could pose a major problem for the application of slurry on waxes of large and complex geometry in an actual dip casting operation. Figures C-3c and C-4c show that the use of this latex binder system resulted in a superior facecoat finish and a uniform thickness of the W layer.

3) PVA: W slurry with solid loading content of 30% was prepared in this case. Without any crosslinking additive, the W layers prepared with PVA binder readily disintegrated when

submerged in water. However, when a controlled amount of crosslinking agent was added and the same dissolution test performed, swelling and peeling off of the W layer *in one single piece* were observed after a few minutes of water immersion. This signifies that crosslinking did occur, but might not be sufficient for a dip casting operation.

A uniform W surface with pores distributed evenly throughout was observed in the case of pure PVA (Fig. C-3d). A worm-like surface with small pores, similar to what found in starch shells (Fig. C-3a), was observed in the case of PVA+crosslinker (Fig. C-3e). Figs C-4d and C-4e reveal that the W layers of these two systems are of non-uniform thickness. Interestingly, when this specimen was reproduced without using zirconia stucco sands between the W and Al_2O_3 layers, a superior surface quality was obtained (Fig. C-3f). This result suggests that (i) the presence of sand and potentially the size of the sand particles critically influence the quality of green shells in the dewaxing stage and (ii) the crosslinking agent as used here did help PVA survive the autoclave environment. The former issue is addressed in more detail in Ch. V.

IV. Conclusion

The feasbility of various environmentally-friendly binder systems for investment casting was examined in this study. Based upon a variety of quantitative and qualitative properties, water-soluble latexes and cross-linked PVA exhibited the best performance and were selected as candidates for further optimization and production use. Continued studies with optimized or modified thermoplastic starch-based systems may lead to the development of a completely clean alternative. Finally, this study addressed the potential undesirable effects of stucco sands on the quality of the as-dewaxed coating surface. The application of stucco sands therefore needs to be carefully controlled and may require proper adjustment when different types of binders are used.

Table C-1: The characteristics of W slurries and W layer prepared by various binder systems

Binder	Solid Loading [vol%]	Packing Fraction	Viscosity [cP]	Wetting	Dissolution of W layer [%]
Starch	20	0.39	18520	Good	0.1
PVA	30	0.50	760	Excellent	12.9
PVA+Crosslinker	30	0.47	1096	Excellent	1.8
LatexI (Latrix)	50	0.69	326	Good	0
LatexII (Ucar)	55	0.62	1250	Excellent	0.2

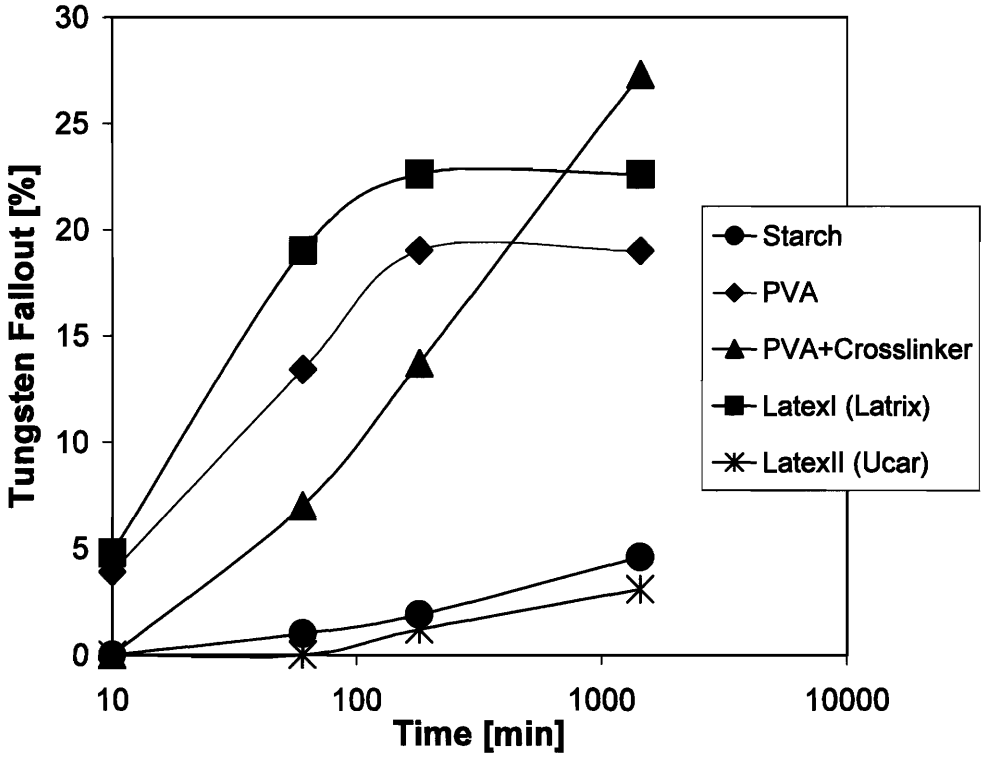

Fig. C-1: The trends of slurry sedimentation as observed in various sets of W slurries which contain different types of binders.

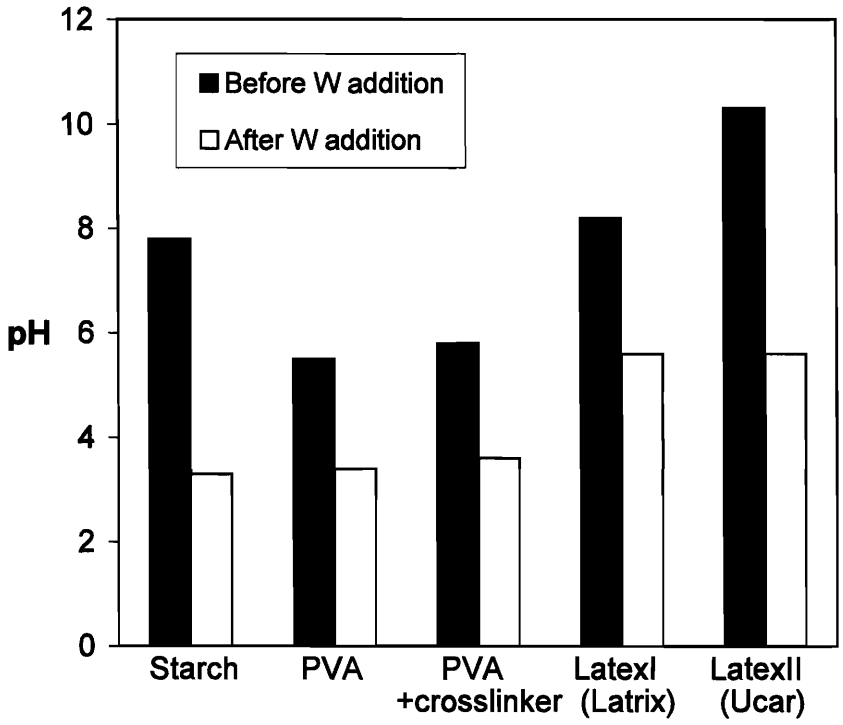

Fig. C-2: Change in pH with W addition of various sets of W slurries containing different types of binders.

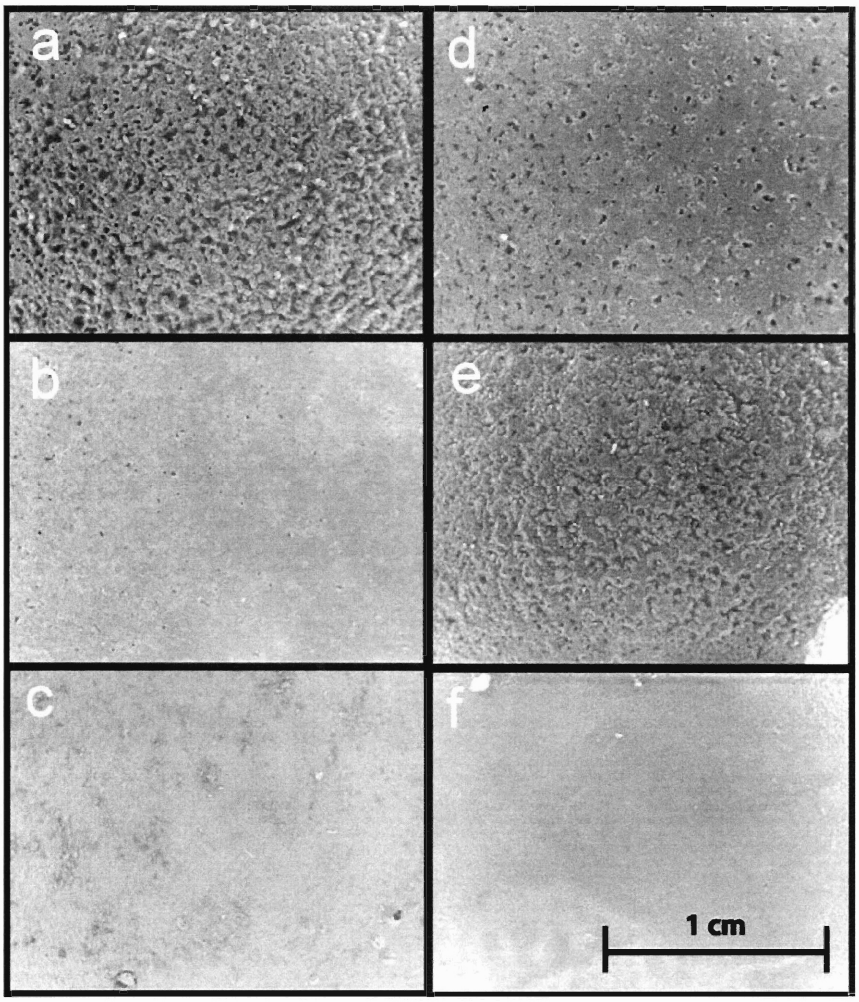

Fig. C-3a-f: Optical micrographs showing the morphology of the W surfaces prepared by slurries that contained (a) starch, (b) latex I (Latrix), (c) latex II (Ucar), (d) PVA, and (e and f) PVA+crosslinker, as a binder. All specimens (a-e) contained zirconia sand between the W and Al_2O_3 layers, excepts for that shown in (f) which did not have stucco applied.

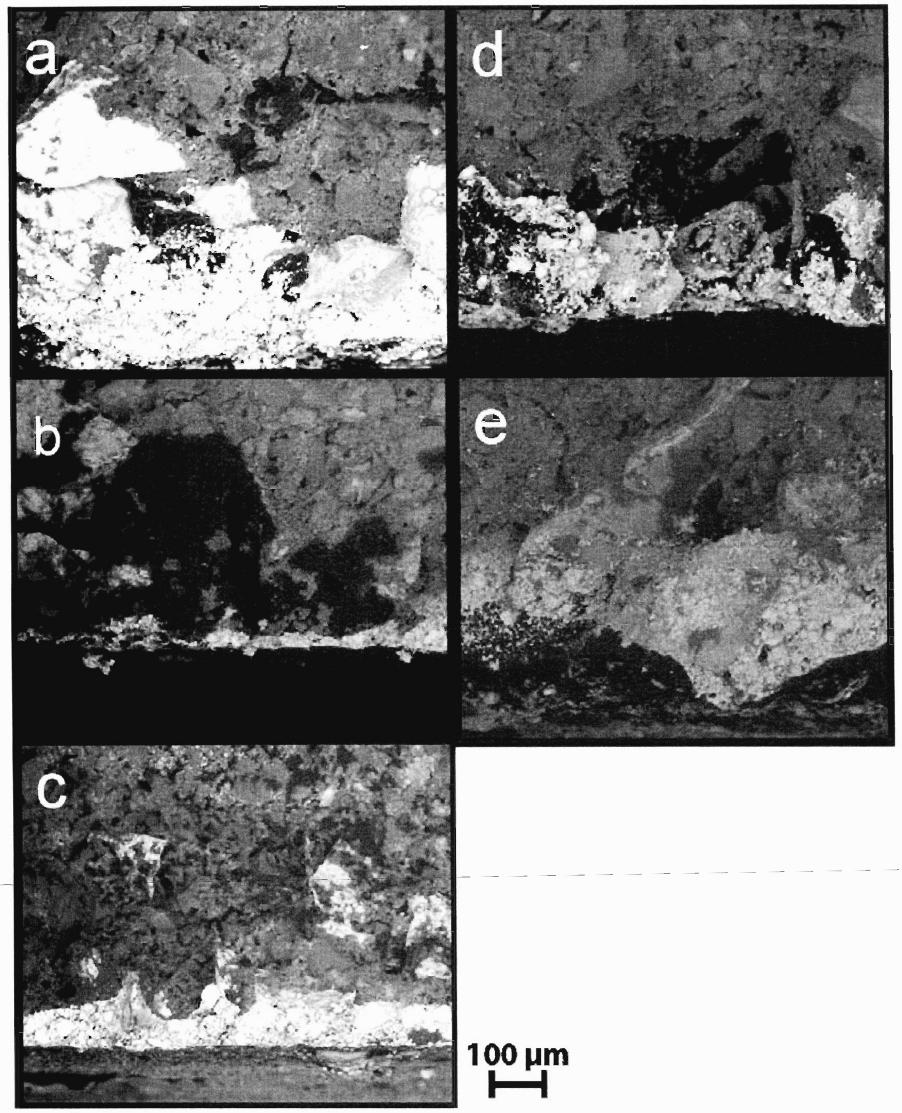

Fig. C-4a-d: Cross-sectional SEM microgrpahs of the speciemens prepared by slurries that contained (a) starch, (b) latex I (Latrix), (c) latex II (Ucar), (d) PVA, and (e and f) PVA+crosslinker, as a binder. All specimens (a-e) contained zirconia sand between the W (bottom) and Al_2O_3 (top) layers.

Appendix D. Sintering Properties of Al_2O_3 with SiO_2 Addition

Four sets of Al_2O_3-SiO_2 specimens were prepared to examine the effects of SiO_2 activation on the sintering properties of Al_2O_3. SiO_2 was chosen primarily due to its common use (in colloidal form) as a binder for Al_2O_3 slurries; such slurries are used extensively in Ch. V. To prepare compact specimens for the study, first, Al_2O_3 powder was mixed with various colloidal silica binders having different silica contents, using a binder-to-powder weight ratio of 0.35. The final composition of SiO_2 and Al_2O_3 are shown in Table D-1. The powders were allowed to dry in aluminum pans, and the dried powder cakes of different sets were then ground and compacted into rectangular bars (8.3 x 25 x 5 mm) of approximately the same green density. The specimens were subsequently fired isothermally at 1177°C in a $3H_2$-$97N_2$ atmosphere for 1 hour. Shrinkage and modulus of rupture (i.e., flexural strength) of the sintered specimens were then evaluated. The rupture test was conducted with a three-point bending measurement using a universal testing machine with a displacement rate of 500 μm/min.

Figure D-1 shows the measured linear shrinkage and modulus of rupture of the test specimens. It is observed that shrinkage of alumina increased gradually with silica content. At high silica content of 8.9% (set S4), linear shrinkage of the material is merely 0.6%. The strength of the materials, however, increased considerably with silica content. Considering the results for specimens in sets S2 and S3, as the SiO_2 content was increased from 2.7% to 5.9%, an increase of modulus of rupture by over three orders of magnitude was obtained. On the other hand, the linear shrinkage values of these materials were comparable and were very low (well below 1%). That the sintering of Al_2O_3 was significantly improved with a minimal degree of shrinkage may suggest that silica additives help enhance the surface diffusion mechanism of Al_2O_3 upon sintering at relatively low firing temperatures. In addition to its capability of providing green strength to Al_2O_3 powder as a binder, colloidal silica also helps improve sintered strength of Al_2O_3 appreciably.

Table D-1: The compositions of SiO_2 in the colloidal silica binders and the final compositions of SiO_2 and Al_2O_3 of the specimens in different sets.

Specimen Set	wt.% SiO_2 in Colloidal Silica Binder	wt.% SiO_2	wt.% Al_2O_3
S1	-	-	100
S2	8	2.7	97.3
S3	18	5.9	94.3
S4	28	8.9	91.1

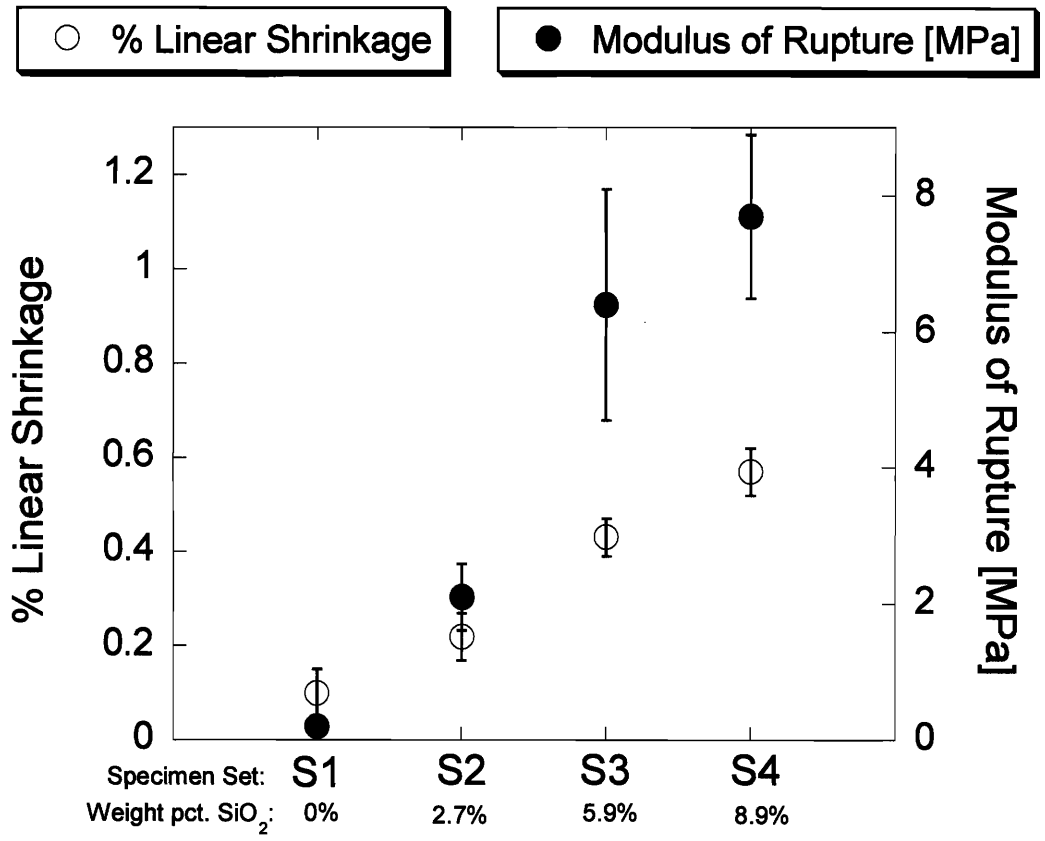

Fig. D-1: Linear shrinkage and modulus of rupture of Al_2O_3 compacts of various specimen sets. These specimens contained different contents of silica, as specified (in weight percent) on the chart.

References

[1] W. D. Coolidge, *Proc. Am. Inst. Elec. Eng*, 1910, pp. 961.

[2] C. L. Briant and B. P. Bewlay, "The Coolidge Process for Making Tungsten Ductile: The Foundation of Incandescent Lighting," *MRS Bulletin*, 1995, pp. 67-73.

[3] S. L. Kang, *Sintering: Densification, Grain Growth & Microstructure*. Burlington, MA: Elsevier Butterworth-Heinemann, 2005.

[4] S. W. H. Yih and C. T. Wang, *Tungsten*. New York: Plenum Press, 1979, pp. 168.

[5] G. S. Upadhyaya, *Sintered Metallic and Ceramic Materials: Preparation, Properties and Applications*. Chichester, England: John Wiley & Sons Ltd., 2000, pp. 439&447.

[6] H. W. Hayden and J. H. Brophy, "Low-temperature sintering of pure tungsten and tungsten-iridium," *Journal of Less-Common Metals*, vol. 6, 1964, pp. 214-8.

[7] N. C. Kothari, "Sintering kinetics in tungsten powder," *Journal of Less-Common Metals*, vol. 5, 1963, pp. 140-150.

[8] I. H. Moon, J. H. Kim, M. J. Suk, S. C. Yoo, J. Choi, and K. M. Lee, "Effect of sintering atmosphere on the sintering behavior of W-powder", *Tungsten and Tungsten Alloys*. PA: TMS, 1991, pp. 27-33.

[9] R. Haubner, "Mechanism of technical reduction of tungsten: part 2, hydrogen reduction of tungsten blue oxide to tungsten powder," *International Journal of Refractory and Hard Metals*, vol. 2, 1983, pp. 108-115.

[10] S. Farooq, P. B. Kemp, R. M. German, and A. Base, "Effect of initial oxygen content and sintering atmosphere dew point on the properties of tungsten based heavy alloys," *International Journal of Refractory Metals and Hard Materials*, vol. 8, Dec. 1989, pp. 236-43.

[11] R. M. German and V. Ham, "Effect of nickel and palladium additions on activated sintering of tungsten," *International Journal of Powder Metallurgy*, vol. 12, 1976, pp. 115-125.

[12] H. W. Hayden and J. H. Brophy, "The activated sintering of tungsten with group VIII elements," *Journal of the Electrochemical Society*, vol. 110, 1963, pp. 805-810.

[13] N. M. Hwang, Y. J. Park, D. Y. Kim, and D. Y. Yoon, "Activated sintering of Ni-doped tungsten approach by grain boundary structural transition," *Scripta Materialia*, vol. 42, 2000, pp. 421-25.

[14] V. V. Panichkina, V. V. Skorokhod, and A. F. Khrienko, "Activated sintering of tungsten and molybdenum powders," *Soviet Powder Metallurgy and Metal Ceramics*, vol. 7, July 1967, pp. 558-560.

[15] R. M. German and Z. A. Munir, "Enhanced low-temperature sintering of tungsten," *Metallurgical and Materials Transactions A*, vol. 7A, 1976, pp. 1873-7.

[16] C. J. Li and R. M. German, "Enhanced sintering of tungsten - phase equilibria effects on properties," *The International Journal of Powder Metallurgy & Powder Technology*, vol. 20, 1984, pp. 149-162.

[17] C. J. Li and R. M. German, "The properties of tungsten processed by chemically activated sintering," *Metallurgical and Materials Transactions A*, vol. 14A, 1983, pp. 2031-2041.

[18] A. A. Timofeeva, I. B. Bulat, Y. V. Voronin, G. K. Fedoseev, and V. M. Karasev, "Formation of a solid solution during interdiffusion of tungsten and molybdenum in the

course of sintering," *Soviet Powder Metallurgy and Metal Ceramics*, vol. 23, Oct. 1984, pp. 772-4.
[19] V. V. Skorokhod, S. M. Solonin, L. I. Chernyshev, L. L. Kolomiets, and L. I. Shnaiderman, "Activating effect of small additions of group VIII metals on alloy formation during the sintering of tungsten and molybdenum powders mixed with other refractory metals," *Soviet Powder Metallurgy and Metal Ceramics*, vol. 15, June 1976, pp. 435-8.
[20] A. Bose and R. M. German, "Tensile properties of tungsten-molybdenum heavy alloys," *Metallurgical and Materials Transactions A*, vol. 21A, 1990, pp. 1325-7.
[21] H. D. Park, W. H. Baik, S. J. L. Kang, and D. Y. Yoon, "The effect of Mo addition on the liquid-phase sintering of W heavy alloy," *Metallurgical and Materials Transactions A*, vol. 27A, 1996, pp. 3120-5.
[22] T. J. Godfrey, R. J. Lewis, D. A. Smith, and G. D. W. Smith, "On the nature and distribution of defects in tungsten lamp wire," *Journal of the Less-Common Metals*, vol. 44, 1976, pp. 319-26.
[23] L. E. Iorio, B. P. Bewlay, and M. Larsen, "Dopant particle characterization and bubble evolution in aluminum-potassium-silicon-doped molybdenum wire," *Metallurgical and Materials Transactions A*, vol. 33A, 2002, pp. 3349-56.
[24] Y. Bin and S. Liyeh, "Study on the low temperature activated sintering of superfine molybdenum powder with oxygen," presented at Proceeding 12th Plansee Seminar, 1989.
[25] R. M. German, *Sintering Theory and Practice*. New York, NY: John Wiley & Sons, Inc., 1996.
[26] A. Belhadjhamida and R. M. German, "Tungsten and tungsten alloys by powder metallurgy - a status review", *Tungsten and Tungsten Alloys*. PA: TMS, 1991, pp. 3-19.
[27] K. Churn and R. M. German, "Fracture behavior of W-Ni-Fe heavy alloys," *Metallurgical and Materials Transactions A*, vol. 15A, 1984, pp. 331-8.
[28] W. E. Gurwell, "Solid-state sintering of tungsten heavy alloys," *Materials and Manufacturing Processes*, vol. 9, 1994, pp. 1115-1126.
[29] H. Hofmann and G. Petzow, "Influence of sintering atmosphere on mechanical properties of tungsten based heavy alloys", *Mod. Dev. In Powder Metall.*, vol. 17. Princeton, NJ: MPIF, 1985, pp. 17-31.
[30] V. V. Skorokhod, L. A. Vermenko, O. I. Get'man, and S. P. Rakitin, "Electron-optical investigation of the sintering kinetics of tungsten powders of spherical particle shape: II. correlation between contact growth kinetics and shrinkage kinetics," *Soviet Powder Metallurgy and Metal Ceramics*, vol. 26, June 1987, pp. 447-54.
[31] T. Vasilos and J. T. Smith, "Diffusion mechanism for tungsten sintering kinetics," *Journal of Applied Physics*, vol. 35, 1964, pp. 215-7.
[32] J. S. Lee, C. Minkwitz, and C. Herzig, "Grain boundary self-diffusion in polycrystalline tungsten at low temperatures," *Phys. Stat. Sol. (b)*, vol. 202, 1997, pp. 931-940.
[33] I. J. Toth and N. A. Lockington, "The kinetics of metallic activation sintering of tungsten," *Journal of the Less-Common Metals*, vol. 12, 1967, pp. 353-65.
[34] G. H. Gessinger and H. F. Fischmeister, "A modified model for the sintering of tungsten with Ni additions," *Journal of the Less-Common Metals*, vol. 27, 1972, pp. 129-41.
[35] G. Fletcher, M. R. James, and J. R. Moon, "The nickel activated sintering of tungsten," *Scripta Meallurgica*, vol. 5, 1971, pp. 105-8.

[36] Y. E. Geguzin, Y. I. Klinchuk, and L. N. Paritskaya, "Effect of a solid-phase nickel coating on the sintering kinetics of tungsten wires," *Soviet Powder Metallurgy and Metal Ceramics*, vol. 15, 1973, pp. 379-82.
[37] R. M. German, *Powder Metallurgy Science*. Princeton, New Jersey: Metal Powder Industries Federation, 1984.
[38] R. M. German, A. Bose, and S. S. Mani, "Sintering time and atmosphere influences on the microstructure properties of tungsten heavy alloy," *Metallurgical and Materials Transactions A*, vol. 23A, 1992, pp. 211-9.
[39] S. Hofmann and H. Hofmann, "Influence of grain boundary segregation on mechanical properties of activated sintered tungsten," *Journal De Physique, Colloque C4*, vol. Supplement No. 4, 1985, pp. 633-640.
[40] A. Ioshi and D. F. Stein, *Metallurgical and Materials Transactions*, vol. 1, 1970, pp. 2543-4.
[41] B. H. Rabin and R. M. German, "Microstructure effects on tensile properties of tungsten-nickel-iron composites," *Metallurgical and Materials Transactions A*, vol. 19A, 1988, pp. 1523-32.
[42] R. G. O'Donnell and R. L. Woodward, "Influence of temperature on the fracture of a W-Ni-Fe alloy," *Journal of Materials Science*, vol. 35, 2000, pp. 4319-4324.
[43] R. G. O'Donnell, S. J. Alkemade, and R. L. Woodward, "Effect of sinter duration on the mechanical properties of a tungsten alloy," *Journal of Materials Science*, vol. 27, 1992, pp. 6490-4.
[44] D. K. Kim, S. Lee, and H. S. Song, "Effect of tungsten particle shape on dynamic deformation and fracture behavior of tungsten heavy alloys," *Metallurgical and Materials Transactions A*, vol. 29A, 1998, pp. 1057-1069.
[45] S. Jones and C. Yuan, "Advances in shell moulding for investment casting," *Journal of Materials Processing Technology*, vol. 135, 2003, pp. 258-65.
[46] S. Jones, M. R. Jolly, and K. Lewis, "Development of techniques for predicting ceramic shell properties for investment casting," *British Ceramic Society Transactions*, vol. 101, 2002, pp. 106-113.
[47] B. P. Gorman and H. U. Anderson, "Processing of composite thin film solid oxide fuel cell structures," *Journal of the American Ceramic Society*, vol. 88, 2005, pp. 1747-53.
[48] H. Li, C. Xia, X. Fang, X. He, X. Wei, and G. Meng, "Co-sintering of SDC/NiO-SDC bi-layers prepared by tape casting," *Key Engineering Materials*, vol. 280-283, 2005, pp. 779-84.
[49] M. Boaro, J. M. Vohs, and R. J. Gorte, "Synthesis of highly porous yttria-stabilized zirconia by tape-casting methods," *Journal of the American Ceramic Society*, vol. 86, 2003, pp. 395-400.
[50] H. X. Peng, Z. Fan, and J. R. G. Evans, "Novel MMC microstructures prepared by melt infiltration of reticulated ceramic preforms," *Materials Science and Technology*, vol. 16, 2000, pp. 903-7.
[51] I. H. Moon, J. Y. Kim, and Y. D. Kim, "Relationship between the addition method of the Ni-activator and the sinterability for the Ni-doped W-powder compact," *International Journal of Refractory Metals & Hard Materials*, vol. 3, 1984, pp. 176-9.
[52] V. K. Singh, "Sintering of calcium aluminate mixes," *British Ceramic Transactions*, vol. 98, 1999, pp. 187-90.

[53] L. C. Pathak, "Fabrication and sintering characteristics of doctor blade," *Ceramic International*, vol. 30, 2004, pp. 417-27.
[54] E. T. Henig, H. Hofmann, and G. Petzow, *Proceedings of The Tenth Plansee-Seminar*, vol. 2, H. M. Ortner, Ed. Reutte, Austria: Metallwerk Plansee, 1981.
[55] G. V. Raynor and V. G. Rivlin, *International Metals Reviews*, vol. 26, 1981, pp. 213-49.
[56] N. S. Stoloff, "An overview of powder processing of silicides and their composites," *Materials Science & Engineering A*, vol. 261, 1999, pp. 169-80.
[57] G. Zielger, "Relationships between processing, microstructure and properties of dense and reaction-bonded silicon nitride," *Journal of Materials Science*, vol. 22, 1987, pp. 3041-86.
[58] R. Vassen, "Processing and properties of nanophase ceramics," *Journal of Materials Processing Technology*, vol. 92-93, 1999, pp. 77-84.
[59] T. D. McGee, "Grain boundaries in ceramic materials," *Materials Science Research*, 1965, pp. 3-32.
[60] I. V. Nel'zina and I. D. Radomysel'skii, "Production and properties of dense P/M stainless steels," *Soviet Powder Metallurgy and Metal Ceramics*, vol. 20, 1981, pp. 854-62.
[61] O. Horacsek and L. Bartha, "The influence of micropores on the high temperature creep rupture of powder metallurgical tungsten wires," *Physics of Sintering*, vol. 5, 1973, pp. 85-94.
[62] P. Arato, E. Besenyei, A. Kele, and F. Weber, "Mechanical properties in the initial stage of sintering," *Journal of Materials Science*, vol. 30, 1995, pp. 1863-71.
[63] D. J. Green and D. Hardy, "Fracture toughness of partially-sintered brittle materials," *Journal of Materials Science Letters*, vol. 15, 1996, pp. 1167-8.
[64] J. Luo and R. Stevens, "Porosity-dependence of elastic moduli and hardness of 3Y-TZP ceramics," *Ceramics International*, vol. 25, 1999, pp. 281-6.
[65] D. C. C. Lam, F. F. Lange, and A. G. Evans, "Mechanical properties of partially dense alumina produced from powder compacts," *Journal of the American Ceramic Society*, vol. 77, 1994, pp. 2113-17.
[66] F. Tancret, "Comment on "Mechanical properties in the initial stage of sintering"," *Journal of Materials Science Letters*, vol. 19, 2000, pp. 1557-8.
[67] H. F. Fischmeister and E. Arzt, "Densification of powders by particle deformation," *Powder Metallurgy*, vol. 26, 1983, pp. 82-8.
[68] E. Arzt, "The influence of an increasing particle coordination on the densification of spherical powders," *Acta Metallurgica*, vol. 30, 1982, pp. 1883-90.
[69] S. K. Maiti, M. F. Ashby, and L. J. Gibson, "Fracture toughness of brittle cellular solids," *Scripta Metallurgica*, vol. 18, 1984, pp. 213-7.
[70] V. V. Skorokhod, *Rheological Basis of Theory of Sintering*. Kiev: Naukova Dumka, 1972.
[71] A. S. Helle, K. E. Easterling, and M. F. Ashby, "Hot-isostatic pressing diagrams: new developments," *Acta Metallurgica*, vol. 33, 1985, pp. 2163-74.
[72] R. M. German, *Particle Packing Characteristics*. Princeton, NJ: Industries Federation, 1989.
[73] J. C. Knight, A. S. Wagh, and W. A. Reid, "The mechanical properties of ceramics from bauxite waste," *Journal of Materials Science*, vol. 21, 1986, pp. 2179-84.
[74] S. C. Danforth and M. H. Richman, "Strength and fracture toughness of reaction-bonded Si_3N_4," *American Ceramic Society Bulletin*, vol. 62, 1983, pp. 501-4.

[75] L. L. Seigle and C. D. Dickinson, "Effect of mechanical and structural variables on the ductile to brittle transition in refractory metals", *Refractory Metals and Alloys*, vol. 17: Interscience Publishers, 1963, pp. 65-117.
[76] G. R. V. Houten, "A survey of ceramic-to-metal bonding," *American Ceramic Society Bulletin*, vol. 38, 1959, pp. 301-7.
[77] K. Otsuka, T. Usami, and M. Sekihata, "Interfacial bond strength in alumina ceramics metallized and cofired with tungsten," *American Ceramic Society Bulletin*, vol. 60, 1981, pp. 540-5.
[78] M. E. Twentyman, "High-Temperature Metallizing: Part 1. The Mechanism of Glass Migration in the Production of Metal-Ceramic Seals," *Journal of Materials Science*, vol. 10, 1975, pp. 765-76.
[79] M. E. Twentyman and P. Popper, "High-temperature metallizing: part 2. the effect of experimental variables on the structure of seals to debased aluminas," *Journal of Materials Science*, vol. 10, 1975, pp. 777-90.
[80] M. E. Twentyman and P. Hancock, "High-temperature metallizing of alumina", *Surfaces and interfaces in ceramic and ceramic-metal systems*, J. Pask and A. Evans., Eds. New York: Plenum Press, 1981, pp. 535-45.
[81] P. F. Varadi and R. Dominguez, "Tungsten metallizing of ceramics," *American Ceramic Society Bulletin*, vol. 9, 1966, pp. 789-91.
[82] B. C. Foster, F. J. Bachner, E. S. Tormey, M. A. Occhionero, and P. A. White, "Advanced Ceramic Substrates for Multichip Modules with Multilevel Thin Film Interconnects," *IEEE Transactions on Components, Hybrids, and Manufacturing Technology*, vol. 14, 1991, pp. 784-9.
[83] S. S. Cole and G. Sommer, "Glass-migration mechanism of ceramic-to-metal seal adherence," *Journal of the American Ceramic Society*, vol. 44, June 1961, pp. 265-271.
[84] D. A. Chance, "Refractory metallization of green ceramic," *Metallurgical Transactions*, vol. 1, 1970, pp. 685-94.
[85] P. S. Kislyi, B. D. Storozh, and M. L. Gorb, "Strength of alumina-tungsten cermets," *Soviet Powder Metallurgy and Metal Ceramics*, vol. 16, April 1977, pp. 299-302.
[86] L. Reed and R. A. Huggins, "Electron probe microanalysis of ceramic-to-metal seals," *Journal of the American Ceramic Society*, vol. 48, 1965, pp. 421-6.
[87] F. Belnou, J. Bernard, D. Houivet, and J. M. Haussonne, "Low temperature sintering of $MgTiO_3$ with bismuth oxide based additions," *Journal of the European Ceramic Society*, vol. 25, 2005, pp. 2785-9.
[88] T. Cheng and R. Raj, "Flaw generation during constrained sintering of metal-ceramic and metal-glass multilayer films," *Journal of the American Ceramic Society*, vol. 72, 1989, pp. 1649-55.
[89] K. Biswas and G. S. Upadhyaya, "Co-sintering of tungsten alloy slurry coated alumina composites and their properties," *Materials & Design*, vol. 19, 1998, pp. 231-40.
[90] J. R. Floyd, "Effect of composition and crystal size of alumina ceramics on metal-to-ceramic bond strength," *American Ceramic Society Bulletin*, vol. 42, 1963, pp. 65-70.
[91] S. J. Howard, R. A. Stewart, and W. J. Clegg, "The delamination of ceramic laminates due to residual thermal stresses," *Key Engineering Materials*, vol. 116-117, 1996, pp. 331-350.

[92] T. W. Clyne and S. C. Gill, "Residual stresses in thermal spray coatings and their effect on interfacial adhesion: a review of recent work," *Journal of Thermal Spray Technology*, vol. 5, 1996, pp. 401-418.

[93] X. Wang and P. Xiao, "Residual stresses and constrained sintering of YSZ/Al2O3 composite coatings," *Acta Materialia*, vol. 52, 2004, pp. 2591-2603.

[94] H. Tomaszewski, J. Strzeszewski, and W. Gebicki, "The role of residual stresses in layered composites of Y-ZrO_2 and Al_2O_3," *Journal of the European Ceramic Society*, vol. 19, 1999, pp. 255-262.

[95] P. Z. Cai, D. J. Green, and G. L. Messing, "Constrained densification of alumina/zirconia hybrid laminates, I: experimental observations of processing defects," *Journal of the American Ceramic Society*, vol. 80, 1997, pp. 1929-39.

[96] P. G. Charalambides, J. Lund, A. G. Evans, and R. M. McMeeking, "A test specimen for determining the fracture resistance of bimaterial interfaces," *Journal of Applied Mechanics*, vol. 56, 1989, pp. 77-82.

[97] P. Lucksanasombool, W. A. J. Higgs, R. J. E. D. Higgs, and M. V. Swain, "Interfacial fracture toughness between bovine cortical bone and cements," *Biomaterials*, vol. 24, 2003, pp. 1159-66.

[98] J. Malzbender, R. W. Steinbrech, and L. Singheiser, "Determination of the interfacial fracture energies of cathodes and glass ceramic sealants in a planar solid-oxide fuel cell design," *Journal of Materials Research*, vol. 18, 2003, pp. 929-34.

[99] A. Cazzato and K. T. Faber, "Fracture energy of glass-alumina interfaces via the bimaterial bend test," *Journal of the American Ceramic Society*, vol. 80, 1997, pp. 181-88.

[100] A. J. Phillipps, W. J. Clegg, and T. W. Clyne, "Fracture behavior of ceramic laminates in bending-II comparison of model predictions with experimental data," *Acta metallurgica et materialia*, vol. 41, 1993, pp. 819-827.

[101] Z. Suo and J. W. Hutchinson, "Sandwich test specimen for measuring interface crack toughness," *Materials Science & Engineering A*, vol. 107, 1989, pp. 135-43.

[102] S. H. Crandall, N. C. Dahl, and T. J. Lardner, *An introduction to the mechanics of solids*. New York: McGraw-Hill, 1999, pp. 416-510.

[103] Y. H. Kim, S. H. Cho, J. K. Lee, and I. H. Moon, "High temperature properties of Ni-activated sintered W-powder compact," *International Journal of Refractory Metals & Hard Materials*, vol. 7, 1988, pp. 206-9.

[104] W. B. Eisen, *ASM Handbook: Powder metal technologies and applications*. Materials Park, OH: ASM, 1998, pp. 907.

[105] G. T. Murray, *Handbook of materials selection for engineering applications*. New York, NY: Marcel Dekker, Inc., 1997, pp. 263.

[106] J. F. Shackelford and W. Alexander, *CRC materials science and engineering handbook 3rd ed.* Boca Raton, FL: CRC Press, 2001, pp. 462.

[107] D. N. Boccaccini and A. R. Boccaccini, "Dependence of ultrasonic velocity on porosity and pore shape in sintered materials," *Journal of Nondestructive Evaluation*, vol. 16, 1997, pp. 187-92.

[108] L. J. Gibson and M. F. Ashby, *Cellular Solids: Structure & Properties*. Elmsford, NY: Pergamon Press, 1988, pp. 207.

[109] J. R. Rice, "Elastic fracture mechanics concepts for interfacial cracks," *Journal of Applied Mechanics*, vol. 55, 1988, pp. 98-103.

[110] P. P. L. Matos, R. M. Mcmeeking, P. G. Charalambides, and M. D. Drory, "A method for calculating K^*_I, K^*_{II},K^*_{III}, in mixed mode bimaterial fracture," *International Journal of Fracture*, vol. 40, 1989, pp. 235-54.
[111] P. G. Charalambides, H. C. Cao, J. Lund, and A. G. Evans, "Development of a test method for measuring the mixed mode fracture resistance of bimaterial interfaces," *Mechanics of Materials*, vol. 8, 1990, pp. 269-283.
[112] S. Roham, K. Hardikar, and P. Woytowitz, "Crack penetration and deflection at a bimaterial interface in a four-point bend test," *Journal of Materials Research*, vol. 19, 2004, pp. 3019-27.
[113] S. T. Gonczy and N. Randall, "An ASTM standard for quantitative scratch adhesion testing of thin, hard ceramic coatings," *International Journal of Applied Ceramic Technology*, vol. 2, 2005, pp. 422-8.
[114] G. Behrens and A. H. Heuer, "Microstructural characterization of cofired tungsten-metallized high-alumina electronic substrates," *Journal of the American Ceramic Society*, vol. 75, 1992, pp. 2815-24.
[115] A. J. Blodgett, "Microelectronic Packaging," *Scientific American*, vol. 249, 1983, pp. 86-96.
[116] R. F. Bunshah, "Overview of coating technologies for large scale metallurgical, optical, and electronic applications," *Journal of Vacuum Science & Technology B*, vol. 2, 1984, pp. 789-99.
[117] D. Hotza and P. Greil, "Review: aqueous tape casting of ceramic powders," *Materials Science and Engineering A*, vol. 202, 1995, pp. 206-17.
[118] C. Pagnoux, T. Chartier, M. F. Granja, F. Doreau, J. M. Ferreira, and J. F. Baumard, "Aqueous suspensions for tape-casting based on acrylic binders," *Journal of the European Ceramic Society*, vol. 18, 1998, pp. 241-7.
[119] A. Kristoffersson, E. Roncari, and C. Galassi, "Comparison of different binders for water-based tape casting of alumina," *Journal of the European Ceramic Society*, vol. 18, 1998, pp. 2123-31.
[120] B. Bitterlich, C. Lutz, and A. Roosen, "Rheological characterization of water-based slurries for the tape casting process," *Ceramic International*, vol. 28, 2002, pp. 675-83.
[121] D. H. Yoon and B. I. Lee, "Processing of barium titanate tapes with different binders for MLCC applications," *Journal of the European Ceramic Society*, vol. 24, 2004, pp. 739-52.
[122] J. R. Reed, *Principles of Ceramics Processing*. New York, NY: John Wiley & Sons, Inc., 1995, pp. 525-539.
[123] E. Sachs and M. Cima, "Three dimensional printing: rapid tooling and prototypes directly from a CAD model," *Journal of Engineering for Industry*, vol. 114, 1992, pp. 481-8.
[124] E. Sachs, "CAD-casting: direct fabrication of ceramic shells and cores by three dimensional printing," *Manufacturing Review*, vol. 5, 1992, pp. 117-26.
[125] P. R. Taylor, "Lost wax casting - a short illustrated review," *Metal and Materials*, vol. 2, 1986, pp. 705-710.
[126] R. F. Smart, "High strength and integrity investment castings," *Materials & Design*, vol. 10, 1989, pp. 301-5.
[127] *Investment Casting*, P. R. Beeley and R. F. Smart, Eds. London, UK: The Institute of Materials, 1995, pp. 373-473.

[128] D. L. Twarog, "Causes and cures for shell-related defects," *Modern Casting*, vol. August, 1990, pp. 28-31.
[129] J. Guille, A. Bettinelli, and J. C. Bernier, "Sintering Behaviour of Tungsten Powders Co-Fired with Alumina or Conventionally Sintered," *Powder Metallurgy International*, vol. 20, 1988, pp. 26-8.
[130] J. H. Park and S. J. Lee, "Effect of Oxygen Partial Pressure on Tungsten-Alumina Bonding Behavior," *Journal of Materials Science Letters*, vol. 11, Dec. 1992, pp. 1602-1604.
[131] S. Jones and P. M. Marquis, "Role of silica binders in investment casting," *British Ceramic Transactions*, vol. 94, 1995, pp. 68-73.
[132] J. D. Jackson, N. Singh, and T. Thornton, "Include nothing: step-by-step reduction of investment casting inclusion defects," *Modern Casting*, vol. April, 2004, pp. 35-38.
[133] G. W. Scherer, "Theory of Drying," *Journal of the American Ceramic Society*, vol. 73, 1990, pp. 3-14.
[134] R. C. Chiu, T. J. Garino, and M. J. Cima, "Drying of granular ceramic films: I, Effect of processing variables on cracking behavior," *Journal of the American Ceramic Society*, vol. 76, 1993, pp. 2257-64.
[135] R. A. Horton, "Investment casting", *Metals Handbook*, vol. 15. Materials Park, OH: ASM International, 1988, pp. 253-69.
[136] P. A. Steinmann and H. E. Hintermann, "A review of the mechanical tests for assessment of thin-film adhesion," *Journal of Vacuum Science & Technology A*, vol. 7, 1989, pp. 2267-72.
[137] J. Valli, "A review of adhesion test methods for thin hard coatings," *Journal of Vacuum Science & Technology A*, vol. 6, 1986, pp. 3007-14.
[138] M. S. Hu, M. D. Thouless, and A. G. Evans, "Decohesion of thin films from brittle substrates," *Acta Metallurgica*, vol. 36, 1988, pp. 1301-7.
[139] R. C. Chiu and M. J. Cima, "Drying of granular ceramic films: II, Drying stress and saturation uniformity," *Journal of the American Ceramic Society*, vol. 76, 1993, pp. 2769-77.
[140] R. R. Tummala, "Ceramics in microelectronic packaging," *American Ceramic Society Bulletin*, vol. 67, 1988, pp. 752-58.
[141] W. H. Kohl, "Ceramics and ceramic-to-metal sealing," *Vacuum*, vol. 14, 1964, pp. 333-354.
[142] D. M. Mattox and H. D. Smith, "Role of manganese in the metallization of high alumina ceramics," *American Ceramic Society Bulletin*, vol. 64, 1985, pp. 1363-67.
[143] Nolte, "2,667,432 U.S. Patent," 1954.
[144] H. J. Nolte and R. F. Spurek, "Metal-ceramic sealing with manganese," *Television Engr.*, vol. 1, 1954, pp. 14-18.
[145] K. White and D. P. Kramer, "Microstructure and seal strength relation in the molybdenum-manganese glass metallization of alumina ceramics," *Materials Science and Engineering*, vol. 75, 1985, pp. 207-213.
[146] M. E. Arthur and L. E. Fussell, "Effect of sintering conditions on Al_2O_3-MoMn bond strengths," *American Ceramic Society Bulletin*, vol. 50, 1971, pp. 9982-4.
[147] S. H. Yang and S. Kang, "Fracture behavior and reliability of brazed alumina joints via Mo-Mn process and active metal brazing," *Journal of Materials Research*, vol. 15, 2000, pp. 2238-43.

[148] M. M. Schwartz, *Ceramic Joining*. Ohio: ASM International, 1990.
[149] E. A. Hayduk, "Effect of atmosphere composition on metallizing Al_2O_3 substrates with Mo-Mn paste," *Solid State Technology*, vol. April, 1985, pp. 321-324.
[150] E. A. Hayduk, K. Berger, and B. A. Hassler, "Furnace atmosphere's effect on cofiring tungsten-alumina multilayer substrates," *Solid State Technology*, 1986, pp. 135-8.
[151] E. M. Levin, C. R. Robbins, and H. F. McMurdie, "Phase Diagrams for Ceramists", vol. 1: The American Ceramic Society, INC, 1964.
[152] M. L. Williams, "The stress around a fault or crack in dissimilar media," *Bulletin of the Seismology Society of America*, vol. 49, 1959, pp. 199-204.
[153] J. Dundurs, "Edge-bonded dissimilar orthogonal elastic wedges," *Journal of Applied Mechanics*, vol. 36, 1969, pp. 650-2.
[154] B. M. Malyshev and R. L. Salganik, "The strength of adhesive joints using the theory of cracks," *International Journal of Fracture*, vol. 1965, 1965, pp. 114-128.
[155] N. Sukumar, Z. Y. Huang, J. H. Prevost, and Z. Suo, "Partition of unity enrichment for bimaterial interface cracks," *International Journal for Numerical Methods in Engineering*, vol. 59, 2004, pp. 1075-1102.
[156] A. G. Evans, M. Ruhle, B. J. Dalgleish, and P. G. Charalambides, "The fracture energy of bimaterial interfaces," *Metallurgical Transactions A*, vol. 21A, 1990, pp. 2419-29.
[157] J. R. Rice, "A path independent integral and the approximate analysis of strain concentration by notches and cracks," *ASME Journal of Applied Mechanics*, vol. 35, 1968, pp. 379-86.
[158] D. M. Parks, "The virtual crack extension method for nonlinear materials behavior", *Numerical Methods in Fracture Mechanics*, D. R. Owen, Ed., 1978, pp. 464-478.
[159] D. M. Parks, "A stiffness derivative finite element technique for determination of elastic crack tip stress intensity factors," *International Journal of Fracture*, vol. 10, 1974, pp. 487-502.
[160] P. P. L. Matos, R. M. McMeeking, P. G. Charalambides, and M. D. Drory, "A method for calculating stress intensities in bimaterial fracture," *International Journal of Fracture*, vol. 40, 1989, pp. 235-54.